INFORMATION TO USERS

This reproduction was made from a copy of a document sent to us for microfilming. While the most advanced technology has been used to photograph and reproduce this document, the quality of the reproduction is heavily dependent upon the quality of the material submitted.

The following explanation of techniques is provided to help clarify markings or notations which may appear on this reproduction.

1. The sign or "target" for pages apparently lacking from the document photographed is "Missing Page(s)". If it was possible to obtain the missing page(s) or section, they are spliced into the film along with adjacent pages. This may have necessitated cutting through an image and duplicating adjacent pages to assure complete continuity.

2. When an image on the film is obliterated with a round black mark, it is an indication of either blurred copy because of movement during exposure, duplicate copy, or copyrighted materials that should not have been filmed. For blurred pages, a good image of the page can be found in the adjacent frame. If copyrighted materials were deleted, a target note will appear listing the pages in the adjacent frame.

3. When a map, drawing or chart, etc., is part of the material being photographed, a definite method of "sectioning" the material has been followed. It is customary to begin filming at the upper left hand corner of a large sheet and to continue from left to right in equal sections with small overlaps. If necessary, sectioning is continued again—beginning below the first row and continuing on until complete.

4. For illustrations that cannot be satisfactorily reproduced by xerographic means, photographic prints can be purchased at additional cost and inserted into your xerographic copy. These prints are available upon request from the Dissertations Customer Services Department.

5. Some pages in any document may have indistinct print. In all cases the best available copy has been filmed.

University Microfilms International
300 N. Zeeb Road
Ann Arbor, MI 48106

8501163

Parayanthal, Padmanabhan

SPECTROSCOPIC STUDY OF ALLOY SEMICONDUCTORS GALLIUM(1-X)ALUMINUM(X) ARSENIDE/GALLIUM-ARSENIDE AND (GALLIUM(1-X)ALUMINUM(X))0.47 INDIUM 0.53 ARSENIDE/INDIUM-PHOSPHIDE

City University of New York PH.D. 1984

University
Microfilms
International 300 N. Zeeb Road, Ann Arbor, MI 48106

PLEASE NOTE:

In all cases this material has been filmed in the best possible way from the available copy. Problems encountered with this document have been identified here with a check mark __√__.

1. Glossy photographs or pages ______
2. Colored illustrations, paper or print ______
3. Photographs with dark background ______
4. Illustrations are poor copy ______
5. Pages with black marks, not original copy ______
6. Print shows through as there is text on both sides of page ______
7. Indistinct, broken or small print on several pages __√__
8. Print exceeds margin requirements ______
9. Tightly bound copy with print lost in spine ______
10. Computer printout pages with indistinct print ______
11. Page(s) ____________ lacking when material received, and not available from school or author.
12. Page(s) ____________ seem to be missing in numbering only as text follows.
13. Two pages numbered ____________. Text follows.
14. Curling and wrinkled pages ______
15. Other Dissertation contains pages with print at a slant, filmed as received.

University
Microfilms
International

Spectroscopic Study of Alloy Semiconductors $Ga_{1-x}Al_xAs/GaAs$

and $(Ga_{1-x}Al_x)_{0.47}In_{53}As/InP$

by

Padmanabhan Parayanthal

A thesis
presented to the Graduate Faculty in Physics
in partial fulfillment of the requirements
for the degree of Doctor of Philosophy,
City University of New York

1984

This manuscript has been read and accepted for the Graduate Faculty in Physics in satisfaction of the dissertation requirement for the degree of Doctor of Philosophy.

8/23/84
date

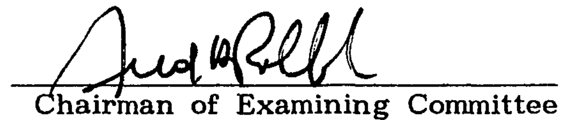
Chairman of Examining Committee

8/27/84
date

Executive Officer

Fred H. Pollak
Albert Bond
Joseph B. Krieger
Sook Lee
Jerry M. Woodall

Supervisory Committee

The City University of New York

Abstract

Spectroscopic study of alloy Semiconductors $Ga_{1-x}Al_xAs/GaAs$ and $(Ga_{1-x}Al_x)_{0.47}In_{53}As/InP$

by

Padmanabhan Parayanthal

Advisor: Professor Fred H. Pollak

The semiconductor alloy systems $Ga_{1-x}Al_xAs/GaAs$ ($0 \leq x \leq 0.9$) and $(Ga_{1-x}Al_x)_{0.47}In_{0.53}As/InP$ ($0 \leq x \leq 1$) and their interfaces with the substrates are investigated using three spectroscopic techniques, i.e., Raman scattering (RS), electroreflectance (ER) and nuclear profiling.

Using a "spatial correlation" model with a Guassian correlation function we have for the first time quantitatively explained the broadening and asymmetry of the first-order longitudinal-optic phonon Raman spectrum induced by alloy potential fluctuations. The systems studied were the representative alloy systems $Ga_{1-x}Al_xAs/GaAs$ and $Ga_{0.47}In_{0.53}As/InP$. This analysis provides important insights into the microscopic nature of the alloy potential fluctuations.

We have performed the first ER study on the quaternary alloy system $(Ga_{1-x}Al_x)_{0.47}In_{0.53}As$ grown lattice matched to InP. The various interband transition energies E_0 (fundamental gap), $E_0+\Delta_0$ (spin

orbit split component), E_1, $E_1+\Delta_1$, E_0' and $E_0'+\Delta_0'$ as well as the spin orbit splittings of the valence bands Δ_0 and Δ_1 were accurately determined. The spin orbit splittings Δ_0 and Δ_1 exhibit a negative bowing similar to that found in the other quaternary alloy system GaInAsP. We have generalized the VV-B-W model including both intra and interband effects to account for the composition dependence of the valence band spin orbit splittings Δ_0 and Δ_1 in the quaternary alloys InGaAsP and GaAlInAs grown lattice matched to InP.

The effects of substrate preparation on the properties of the epitaxial layer are investigated in GaAlAs/GaAs heterojunctions prepared by different modifications of liquid phase epitaxy using RS as well as ER. Signals were observed from both the GaAlAs epilayer and the GaAs substrate at the interface. The results are correlated with the properties of the substrate and growth condition.

The major limitation to the depth resolution in depth profiling using ion beams is the energy straggling of the projectiles resulting from the statistical nature of the energy loss mechanism. We have done the first energy straggling measurements in GaAlAs using nuclear reaction technique. The samples were prepared by MBE. We have also observed the importance of growing buffer layers to obtain sharp interfaces in GaAlAs/GaAs heterostructures.

ACKNOWLEDGEMENTS

To Professor Fred H. Pollak, my thesis advisor, I wish to express my deepest gratitude for his valuable guidance and constant encouragement throughout this thesis work. His enthusiasm and creativity in exploring and understanding physics were an inspiration.

I would also like to express my special gratitude to Professor Albert Bond of Brooklyn College of CUNY and Dr. Jerry M. Woodall of IBM for the various help given to me during the course of this work. I like to acknowledge with deep appreciation the careful reading of this manuscript and the advice given to me by other committee members, Professors Joseph B. Krieger of Brooklyn College of CUNY and Sook Lee of Hunter College of CUNY.

There are many whom I would like to express my sincere thanks, Dr. Paul M. Amirtharaj for the constant encouragement and for several helpful suggestions, Dr. Orest J. Glembocki for the various useful discussions, and the graduate students of the solid state laboratory for their co-operation and help.

I would like to express my gratitude to Dr. Nick Bottka of U.S. Naval Research Laboratories, Dr. Tom Pearsall of Bell Laboratories, Dr. Gary Wicks of Cornell University, and Dr. Jerry Woodall of IBM for providing the samples used in this study.

I wish to acknowledge with gratitude the department of Physics of Brooklyn College for providing me this opportunity, the Research foundation of CUNY for the financial support during the course of this work, and the Brooklyn College computer center for allowing me to use their facilities.

Contents

Abstract iii

ACKNOWLEDGEMENTS v

List of Tables ix

List of Figures xi

Chapter I: INTRODUCTION 1

Chapter II: RAMAN SPECTROSCOPY 12

General Description of Raman Scattering 13
First-order Raman Scattering (microscopic description). 15
Selection Rules 21
First-order scattering 21
Second-order scattering. 27
LO - TO splitting. 28
Coupled LO phonon plasmon modes. 29
Alloy mixed mode behavior. 32
Experimental details 33
Optics and electronics. 33
Sample details. 36
Experimental Results. 38
Characterization of epilayer, interface and substrate. 38
Band bending and carrier depletion 45
Alloy composition 47
Crystalline quality 48
Symmetry forbidden TO modes. 49
Raman lineshape and microscopic alloy disorder 50
Spatial Correlation model 56

Chapter III: MODULATION SPECTROSCOPY 68

Electric Field Modulation 74
Third derivative spectra. 74
Experimental Details 80
Optics and Electronics 82
visible and near uv 82
Infrared Range 85
Sample details. 87
Experimental Results 88
Electroreflectance: GaAlInAs/InP 91
E_0 and $E_0+\Delta_0$ transitions. 91
E_1 and $E_1+\Delta_1$ transitions 100
E_0' and $E_0'+\Delta_0'$ transitions. 103
Composition dependence of transition energies 103
Electroreflectance: GaAlAs/GaAs 109
Composition dependence of the spin orbit splittings. 114

Chapter IV: ION BEAM SPECTROSCOPY 125

Nuclear profiling technique 126
Energy straggling 127
Instrumental width 135
Experimental details 135
Sample details. 140
Data analysis and results 142
Evaluation of the straggling parameter. 146
Effect of substrate preparation. 148

Chapter V: Summary and conclusions. 151

Bibliography 159

TABLES

Ia. The "allowed" Raman tensor $\chi^{1}_{\alpha\beta}$, the q-dependent Raman tensor $\chi^{1}_{\alpha\beta q}$ and the electric field induced Raman tensor $\chi^{1}_{\alpha\beta E}$. 26

b. The strain induced Raman tensor $\chi^{1}_{\alpha\beta\eta}$. 27

II. Characterstics of the $Ga_{1-x}Al_xAs/GaAs$ and $Ga_{0.47}In_{0.53}As/InP$ samples in Fig. 13. 52

III. The transition energies and broadening parameters for the various $(Ga_{1-x}Al_x)_{0.47}In_{0.53}As/InP$ samples measured at room temperature. 100

IV. Values of the quadratic fitting parameters $\underline{a}$, $\underline{b}$ and $\underline{c}$ obtained by fitting the various E versus x curves to the equation $E = \underline{a} + \underline{b}x + \underline{c}x^2$ 107

V. Values of the quadratic fitting parameters $\underline{a}$, $\underline{b}$ and $\underline{c}$ for the spin orbit splitting parameters Δ_0 and Δ_1 for $In_{1-y}Ga_yAs_xP_{1-x}$ and $(Ga_{1-x}Al_x)_{0.47}In_{0.53}As$ lattice matched to InP. All measurements were made at room temperature. 117

VI. Characterstics of the $Ga_{1-x}Al_xAs/GaAs$ samples used for nuclear profiling measurements. 141

VII. The measured straggling coefficient (K_M) and thickness for the two samples MBE 31-3 and MBE 32-X. The ratio K_M/K_B, where K_B is the Bohr straggling coefficient, is also listed. 141

FIGURES

1a. Two band Raman scattering processes.

b. Three band Raman scattering processes. 17

2. Kinematics of the Stokes inelastic light scattering. 22

3. Phonon dispersion curves for (a) silicon and (b) GaAs. . . . 29

4. The frequency dependence of the q=0 coupled LO phonon-plasmon modes on the electron density in GaAs. 32

5. Schematic functional block diagram of Raman scattering apparatus. 35

6. Schematic representation of the phase diagram for the liquid phase epitaxial growth of $Ga_{1-x}Al_xAs$. 38

7a. Raman spectrum of GaAs E-820, the substrate used for SCL-392. The upper right-hand corner shows the coupled mode L_+. The sharper structures are due to second-order two-phonon Raman scattering.

b. Raman spectrum of $Ga_{1-x}Al_xAs$/GaAs sample SCL-392. The upper right-hand corner shows the Raman spectrum in the range 500-800 cm^{-1}. These Raman structures are from the $Ga_{1-x}Al_xAs$ epilayer. 40

8a. Raman spectrum of GaAs E-1068, the substrate used for SCL-400. The upper right-hand corner shows the coupled

mode L_+. The sharper structures are due to second-order two-phonon Raman scattering.

b. Raman spectrum of $Ga_{1-x}Al_xAs/GaAs$ sample SCL-400. The upper right-hand corner shows the Raman spectrum in the range 500~800 cm^{-1}. Features to the left of the vertical dashed line are from GaAs substrate and those to the right are from the $Ga_{1-x}Al_xAs$ epilayer. 41

9a. Raman spectrum of GaAs A-1319, the substrate used for SCL-379.

b. Raman spectrum of $Ga_{1-x}Al_xAs/GaAs$ sample SCL-379. 42

10. Variation of the mode frequencies of $Ga_{1-x}Al_xAs$ with composition x. 48

11. Raman spectra from (100) $Ga_{1-x}Al_xAs/GaAs$ at 300 K for x=0.0, 0.3, 0.5, and 0.9. A small background due to the disorder activated TO phonons has been substracted from the low-energy side of the alloy spectra. The dashed line show the fit obtained from the theoritical model. 53

12. Raman spectra from (100) $Ga_{0.47}In_{0.53}As/InP$ samples #13, #15 and #11 at 300 K.. 55

13. The relationship between broadening Γ and asymmetry Γ_a/Γ_b as a function of correlation length L. The dashed line and solid line are calculated for AlAs dispersion (L_1)

and GaAs dispersion (L_2), respectively, with $\exp(-r^2/L^2)$ as the correlation function. The dotted line shows the relationship for GaAs dispersion (L_2') using $\exp(-r/L)$ spatial correlation. The experimental points for the various samples are also shown. 62

14. The singular portion of ε_1 and ε_2 at the four types of critical points. 73

15. Schematic functional block diagram of the electroreflectance setup for the energy range 1.3 eV to 7 eV 83

16. Schematic functional block diagram of the electroreflectance setup for the infrared region. 86

17. Bandstructure of GaAs along (100) and (111) directions. . . . 89

18. Electroreflectance spectrum of n-GaAs at 300 K. 90

19. Electroreflectance spectrum of $(Ga_{1-x}Al_x)_{0.47}In_{0.53}As/InP$ at 300 K for x=0.04. 92

20. Electroreflectance spectrum of $(Ga_{1-x}Al_x)_{0.47}In_{0.53}As/InP$ at 300 K for x=0.2. 93

21. Electroreflectance spectrum of $(Ga_{1-x}Al_x)_{0.47}In_{0.53}As/InP$ at 300 K for x=0.4. 94

22. Electroreflectance spectrum of $(Ga_{1-x}Al_x)_{0.47}In_{0.53}As/InP$ at 300 K for x=0.6. 95

23. Electroreflectance spectrum of $(Ga_{1-x}Al_x)_{0.47}In_{0.53}As/InP$ at 300 K for x=0.8. 96

24. Electroreflectance spectrum of $(Ga_{1-x}Al_x)_{0.47}In_{0.53}As/InP$ at 300 K for x=1.0. 97

25. A typical lineshape fit for E_0 feature. 99

26. A typical lineshape fit for E_1 and $E_1+\Delta_1$ features. 102

27. Variation of the E_0 and $E_0+\Delta_0$ and Δ_0 energies as a function of composition x. The dashed line is theory of Aymerich (Ref. 12). 105

28. Variation of the E_1, $E_1+\Delta_1$ E_0', $E_0'+\Delta_0'$ and Δ_1 transition energies as a function of composition x.. 106

29. Electroreflectance spectrum of $(Ga_{1-x}Al_x)_{0.47}In_{0.53}As/InP$ at 300 K for x=0.0. 108

30. Electroreflectance spectrum of $Ga_{1-x}Al_xAs/GaAs$ sample SCL-392. 110

31. Electroreflectance spectrum of $Ga_{1-x}Al_xAs/GaAs$ sample SCL-400. 111

32. Electroreflectance spectrum of $Ga_{1-x}Al_xAs/GaAs$ sample SCL-379. 112

33. Variation of the spin orbit spilttings with alloy composition x for $In_{1-y}Ga_yAs_xP_{1-x}$. lattice matched to InP (x=2.2y). . . .122

34. Variation of the spin orbit spilttings with alloy composition x for $(Ga_{1-x}Al_x)_{0.47}In_{0.53}As/InP$ lattice matched to InP. . . 124

35. Gamma ray yield from a pure GaAs sample and a $Ga_{1-x}Al_xAs$ sample. 129

36. Integrated reaction cross section for $^{27}Al(p,\gamma)^{28}Si$ reaction, measured with a thick target. (Ref. 19) 130

37. Energy straggling calculated for protons (right scale) and for ^4He ions (left scale) for all elements at various energies. The dashed curve represent the calculations using Thomas-Fermi model while the solid curve represent the calculations of Chu (Ref. 91) 133

38. Schematic representation of the experimental arrangement for nuclear profiling. 137

39. Schematic representation of the detection system for the nuclear profiling measurements. 139

40. Gamma ray yield (in arbitrary units) as a function incident energy for MBE samples (a) 31-3 and (b) 32-x. The dashed line represent best fit curves to the data (shown by dots). 143

41. Beam profile due to straggling at various depths, according to Bohr theory. The energies labeling the curves are proton bombarding energies. Each curve represents the

depth distribution of protons reaching 992 keV, assuming an initial beam energy spread of 2.8 (FWHM), about the bombarding energy.......................146

42. Gamma ray yield (in arbitrary units) as a function incident energy for MBE sample 49-4. The data are shown by dots. a representative error bar is shown. The dashed line represent best fit curves to the data. The scale at the top of the figure represents the depth corresponding to a given proton energy.......................149

Chapter I

INTRODUCTION

Studies of the fundamental electronic, vibrational, and structural properties of semiconductor alloys have become an important part of semiconductor physics. The availability of a large number of semiconductors with a wide variety of different and often unique properties, made it possible not only to discover new phenomena but also to select optimum materials for specific experimental and theoretical work.

In this thesis we examine the vibrational, electronic, and structural properties of epitaxially grown semiconductor alloys and their interface with the substrate using various spectroscopic techniques. Raman spectroscopy, modulation spectroscopy, and Ion beam spectroscopy (nuclear profiling) are employed to investigate $Ga_{1-x}Al_xAs/GaAs$ ($0 \le x \le 0.9$) and $(Ga_{1-x}Al_x)_{0.47}In_{0.53}As/InP$ ($0 \le x \le 1$) systems. In Raman spectroscopy, which probes the vibrational states of the solid, the characterstic energies range typically from ~10 to 100 meV whereas in modulation spectroscopy, which probes the electronic states, the optical excitations range from ~0.5 eV to 6 eV. Ion beam spectroscopy

(nuclear profiling), involves nuclear energy levels and hence the emission energies involved are several MeV. Thus these spectroscopic techniques are based on a broad range of excitations ranging from a few meV to several MeV.

Raman spectroscopy is an effective and versatile tool for investigating lattice vibrations in semiconductors[1,2]. Lattice vibrations are sensitive to the nearest neighbour interaction and therfore probe the crystal structure and quality on a small scale, i.e., on the order of several lattice spacings. Raman spectroscopy is especially useful for the study of epitaxial layers and heterojunctions since the lattice vibrational spectra are observed as a superposition of contributions from each layer. Depth profiling can be accomplished by using different excitation energies with different penetration depths. In addition, since it is a second-order process, Raman scattering can provide symmetry information which is not available from first-order processes.

In the past two decades modulated optical spectroscopy has evolved into a powerful technique for studying interband electronic transitions, achieving far greater sensitivity and resolution than absolute reflectivity measurements[3,4]. In all modulated optical techniques some parameter of the sample or the measuring system is varied periodically so as to produce a change in the optical reflectance or transmittance of the solid. These periodic variations give rise to sharp differential-like

spectra in the region of photon energies where optical excitation processes occur. Thus in all modulated optical techniques the uninteresting background effects are suppressed and relevent optical features are enhanced. In addition, weak structures that may not be clear in unmodulated spectra are better resolved. At present electric-field modulated reflectivity provides one of the best optical techniques available, in terms of sensitivity and resolution, for the study of the fundamental gap and higher energy electronic transitions in semiconductors.

In a semiconductor heterojunction the energy gap difference in the semiconductor introduces barriers in the energy band diagrams giving a new degree of freedom for the study of fundamental phenomena as well as the design of devices. Recently, attempts to utilize the properties associated with the band gap discontinuities at heterojunctions have required very stringent growth conditions during the formation of the interface. If the interface is abrupt the bandgap changes in an abrupt manner while if the interface is compositionally graded the bandgap will change in a more gradual fashion.

Among the many ion beam techniques nuclear profiling utilizes the presence of narrow resonances in many light nuclei and hence provides a method of accurate depth profiling. In alloy semiconductors with Al as a constituent, nondestructive profiling of Al can be accomplished using

the Al(p,γ)Si nuclear reaction, which has an extremely sharp resonance at 992 keV (lab frame). The 10.7 MeV γ ray emitted during the reaction reveals the presence of Al. The depth profile of Al can be translated into a bandgap profile from the known bandgap variation with Al composition.

Semiconductor alloys are of great interest from both fundamental as well as technological considerations. From the basic physics point of view, compound semiconductor alloys help to examine our theoretical knowledge of how the fundamental electronic as well as lattice vibrational properties vary with chemical composition of the alloy. In addition, when the alloy system is grown lattice matched to the substrate material, they provide a unique testing ground for examining the theories of random disorder.

In the various electronic, vibrational, as well as electrical properties of alloy semiconductors, disorder plays an important role. In many III-V semiconducting compounds either the cation or the anion may be alloyed in arbitrary concentrations. These alloy semiconductors usually have continually varying properties intermediate between the two end point materials. The crystal structure (e.g. zinc-blende) is also preserved. The random substitution of one element (cation or anion) in an otherwise compositionally ordered alloy, introduces potential fluctuations. In addition, recent extended X-ray absorption fine

structure (EXAFS) measurements in alloys such as GaInAs have shown that the Ga-As and In-As bond lengths remain nearly constant in the entire composition range even though the average cation-anion distance closely follows Vegards law[5]. The resulting bondlength alternations cause structural distortion in these alloys. The variation of the fundamental bandgap energy, higher lying interband transitions, as well as spin orbit splittings, with composition, instead of being linear, is found to follow a quadratic relationship in these alloy systems. In general, these nonlinear variations, called "bowing", is a result of alloy potential fluctuations, structural distortion due to bondlength alternations, as well as the breakdown of the virtual crystal approximation.

In lattice matched systems the bowing of the spin orbit splittings has been attributed to the alloy disorder but may also be a consequence of the structural distortion. Thus a detailed study of the compositional variation the spin-orbit splittings in these systems can provide important information regarding these two factors affecting the material properties. Van Vechten-Berolo and Wooley (VV-B-W)[6,7] and Chadi[8] have proposed models to explain the bowing of the spin orbit splittings in semiconductor alloy systems.

Several investigators have observed that the allowed first order Raman lines for the alloy systems has an asymmetric lineshape[9,10] in

contrast to that of the end point materials. This has been attributed to q vector relaxation related to alloy disorder and qualitatively explained. A quantitative explanation of the alloy Raman lineshapes has been lacking. A detailed analysis of the Raman lineshapes can provide important insights into nature of microscopic alloy disorder.

Quaternary alloys are important from a device point of view due to the flexibility offered by these systems to select both energy bandgap, E_g, and lattice constant independently. This is significant because the high quality material required for most devices can be produced only when the epitaxial layer is lattice matched to the substrate, thus avoiding the high density of dislocations as well as interface states generated by the lattice mismatch. For obtaining high quality interfaces required for heterostructure devices it is necessary to change the bandgap without changing the lattice parameter.

Recently, there has been a growing interest in the quaternary alloy system $(Ga_{1-x}Al_x)_{1-y}In_yAs$ based in the arsinides of gallium, aluminum and indium, because of its applications for optical communication devices such as optical emitters, waveguides, and detectors. It can be grown lattice matched to InP for $0 \leq x \leq 1$, $y=0.47$. As the Al atoms are substituted for the Ga, the fundamental bandgap energy is expected to vary continually from 0.75 ev to 1.5 ev at 300 K. This spectral range covers the range of lowest loss as well as dispersion for optical fibers.

Very little work, both theoretical and experimental, has been performed on this quaternary system, in relation to the quaternary GaInAsP/InP alloy system, even though GaAlInAs system has a larger range of the fundamental gap energies. The lack of experimental studies has been mainly related to difficulty in growing good quality single crystal layers by liquid phase epitaxy (LPE). Recently molecular beam epitaxy (MBE) growth process has made it possible to fabricate epitaxial films of this quaternary alloy with good control over alloy composition. Olego et al[11] have investigated the compositional dependance of the band gap energy by room temperature photoluminescence and also the conduction band effective mass, m^*, from Raman scattering experiments. Recently, Aymerich[12,13] has performed a bandstructure calculation based on a model version of the coherent potential approximation.

$Ga_{1-x}Al_xAs$/GaAs is probably among the most important of the various semiconductor heterojunctions fabricated in recent years. In addition to being useful in studying fundamental aspects such as quantum well and superlattice effects this heterojunction has numerous device applications[14,15]. High efficiency solar cells have been fabricated using GaAs p-n junctions with a thin $Ga_{1-x}Al_xAs$ alloy layer on top of the GaAs[16]. The close lattice match of the two materials GaAs and GaAlAs results in a low recombination velocity at the interface which results in negligible surface recombination. The alloy layer can be

highly doped, resulting in low series resistance. This allows the GaAs layer to be doped less than usual in order to obtain larger minority carrier diffusion lengths. Proper use of composition graded GaAlAs/GaAs interfaces in the fabrication of solar cells can improve the solar cell conversion efficiency. The grading of composition results in a built-in electric field for the minority carriers in the GaAlAs layer which directs photoelectrons away from the surface and can therefore significantly enhance the photocurrent collection from the surface region. Theoretical efficiencies as high as 35% under direct sunlight has been predicted for these graded composition heterojunctions. Quantitative evaluation of the composition profile of these graded layers is needed to develop the proper growth technique and to understand the resulting solar cell characterstics.

Heterojunctions have played an important role in the area of injection lasers in recent years[17]. The essential idea is that the potential barriers provided by the heterojunction results in the confinement of the injected carriers in the active volume so that population inversion is more readily achieved and laser gain is higher. GaAlAs/GaAs heterojunction layers have the added advantage that since GaAlAs has a lower refractive index than GaAs; hence, waveguide confinement is also obtained thus reducing laser losses. The development of these heterojunctions has resulted in continous wave (cw) operation of GaAs laser diodes at and above room temperature.

Other applications of $Ga_{1-x}Al_xAs/GaAs$ heterojunctions include high mobility field effect transistors (HMFET) as well as fabrication of superlattices. More recently, interesting applications for GaAlAs/GaAs has been proposed for uses such as Schottky barrier formation and passivation of the GaAs surface for metal-insulator-semiconductor (MIS) technology[18].

In order to understand the performance of these devices it is essential to know the various material parameters related to the epitaxial layer, interfaces as well as substrates.

In ion beam spectroscopy, the nuclear profiling technique has been known for a long time. Only recently has this technique been applied to obtain the Al profiles in semiconductor structures[19,20]. The major limitation to the depth resolution of this technique is the energy straggling of the projectile. It is necessary to obtain accurate values for energy straggling to extract accurate depth profiles.

This thesis is divided into 5 chapters. Chapter II deals with Raman spectroscopy. The basic principles in Raman scattering are discussed in Section 1 and experimental techniques in Section 2. In Section 3 we describe the results of the investigation regarding the effects of the growth parameters on the heterostructure of GaAlAs/GaAs. The samples were prepared under different modifications of LPE. Information is obtained about the various aspects of the epilayer, interface as well as

the substrate including (1) crystal quality (2) alloy composition of the epilayer (3) band bending at the interface as well as the GaAs substrate without the epilayer and (4) carrier depletion. In the last section of Chapter II we conduct a systematic study of the Raman lineshapes $Ga_{1-x}Al_xAs/GaAs$ ($0\leq x\leq 0.9$) and $Ga_{0.47}In_{0.53}As/InP$ grown lattice matched to their substrates by various growth techniques. A "Spatial Correlation" model is presented to explain, for the first time quantitatively, the asymmetry and broadening of the first order Raman lines in these representative alloy systems. This "Spatial Correlation" model is based on q-vector relaxation induced by the alloy potential fluctuations (APF). This model, which is quite general, provides important information about the nature of APF.

Chapter III deals with modulation spectroscopy. The necessary theoretical background for understanding the experimental results are given in section 1 and the experimental procedures in section 2. Section 3 contains the results obtained using this technique for the quaternary alloy system GaAlInAs grown lattice matched to InP. The main focus was on the accurate determination of the various transition energies and their associated broadening. GaAlAs/GaAs prepared under different conditions are examined and the results are presented in Section 4. The effects of microscopic alloy disorder on the bowing of the spin orbit splitting is examined in Section 5. The VV-B-W model is

generalized to explain the bowing in quaternary systems GaAlInAs/InP and GaInAsP/InP.

In Chapter IV we discuss an ion beam spectroscopic technique (nuclear profiling). The basic principles of nuclear profiling are outlined in Section 1. The various theoretical models and current experimental status for the energy straggling are reviewed in section 2. Section 3 contains the experimental details for the nuclear profiling measurements. Experimental results for the measurement of the energy straggling are discussed in section 4. The last section presents the effects of substrate preparation on the composition profile of molecular beam epitaxially grown GaAlAs/GaAs heterostructure.

In the last chapter we summarize the results and conclusions of this study.

Chapter II

RAMAN SPECTROSCOPY

In recent years, with the advent of lasers, light scattering has become one of the most powerful optical techniques for investigating elementary excitations in solids. In semiconductors, Raman scattering has been used to study phonons, single particle and collective charge carrier excitations, electron-phonon interaction, and the properties of defects or disorder in semiconductor alloys and amorphous materials[1,2,21-24]. In resonant Raman scattering experiments where the incident light beam energy is in coincidence with that of an electronic transition, information is obtained about the electronic excitations, as well as electron-phonon interaction. Depth profiling can be accomplished by using different excitation energies with different penetration depths. In addition, since it is a second-order process Raman scattering can provide symmetry information not available from first-order processes. Raman spectroscopy is complimentary to infrared absorption techniques in the sense that the symmetry of the modes coupled to the radiation field can be different, for example in the diamond structure the infrared inactive modes are Raman active.

2.1 General Description of Raman Scattering

In Raman scattering, photons of energy $\hbar\omega$ incident on the material are scattered giving rise to photons up or down shifted in frequency, typically in the range 50 - 1000 cm^{-1}. These freqency shifts are caused by the spatial and temporal variations in the electric susceptibility of the medium. The electric susceptibility $\hat{\chi}$ is given by

$$\vec{P}(\omega)=\hat{\chi}(\omega)\vec{E}(\omega) \tag{1}$$

where $\vec{P}$ and $\vec{E}$ are the polarization and field vector associated with the electric field.

Consider an incident electric field

$$\vec{E}_i=\vec{E}_i^0\cos(\vec{k}_i.\vec{r}-\omega_i t) \tag{2}$$

If $\hat{\chi}$ is spatially and temporaly constant (homogeneous medium) the induced dipole moments oscillate with the frequency ω_i giving rise to scattered light at the same frequency. However, in practice there are spatial and temporal fluctuations in the medium which manifest themselves as fluctuations in $\hat{\chi}$.

We focus mainly on the inelastic scattering of light by collective excitations in solids. For example, consider a phonon described by

$$Q_j=Q_j^0\cos(\vec{q}_j.\vec{r}-\omega_j t) \tag{3}$$

where Q_j^0 is the amplitude of the phonon normal co-ordinate. In the presence of lattice vibrations the linear susceptibility can be expressed as a Taylor expansion in powers of the normal co-ordinate of the phonon. Expanding the susceptibility components $\chi_{\alpha\beta}$ in Q_j we get

$$\chi_{\alpha\beta}(Q_j) = \chi^{(0)}{}_{\alpha\beta}(\omega_i,\omega_s) + \chi^{(1)}{}_{\alpha\beta}(\omega_i,\omega_s) + \chi^{(2)}{}_{\alpha\beta}(\omega_i,\omega_s) + \ldots \quad (4)$$

where

$$\chi^{(0)}{}_{\alpha\beta}(\omega_i,\omega_s) = \chi^{(0)}{}_{\alpha\beta}(\omega_i,\omega_i) = \chi^{(0)}{}_{\alpha\beta}(\omega_i) \quad (5)$$

$$\chi^{(1)}{}_{\alpha\beta}(\omega_i,\omega_s) = [\partial\chi_{\alpha\beta}/\partial Q_j]Q_j \quad (6)$$

$$\chi^{(2)}{}_{\alpha\beta}(\omega_i,\omega_s) = [\partial^2\chi_{\alpha\beta}/\partial Q_j\partial Q_{j'}]Q_jQ_{j'} \quad (7)$$

$\chi^{(0)}{}_{\alpha\beta}$ corresponds to the linear susceptibility and gives rise to scattered light at the frequency of the incident light called Rayleigh scattering. $\chi^{(1)}{}_{\alpha\beta}$ involves one phonon and is the first-order transition susceptibility. Considering the time dependence of the normal co-ordinate Q_j [see Eqn. (3)] and the incident electromagnetic

wave [see Eqn. (2)] we can see that $\chi^{(1)}_{\alpha\beta}$ generates dipoles oscillating at frequencies $\omega_i \pm \omega_j$ and hence produces these frequencies in the scattered light. The frequencies $\omega_i - \omega_j$ are called Stokes lines and $\omega_i + \omega_j$ are termed anti-Stokes lines. Similarly $\chi^{(2)}_{\alpha\beta}$ is the second-order susceptibility and describes the second-order Raman scattering involving two phonons.

2.2 First-order Raman Scattering (microscopic description).

In a microscopic description Raman scattering is viewed as a three step process[2,21,25]. (see Fig. 1)

1. a photon with energy ω_i is absorbed creating an electron-hole pair in the state $|l\rangle$
2. a phonon with energy ω_j is created (or destroyed) and the electron-hole pair is scattered to the state $|m\rangle$
3. the electron-hole pair recombines and a photon with energy ω_s is emitted.

Wavevector is conserved in each step where as energy is conserved only in the total process, i.e., each of the above transitions can be real or virtual. These processes can occur in any time order giving rise to six types of processes. Using third order time dependent perturbation theory one obtains the following expression for the first order susceptibility[25].

$$\chi^{(1)}_{\alpha\beta}(j) = (e^2/m_0^2\omega_s^2 V) \sum_{\ell m} \frac{<0|p_\alpha|m><m|H_{EL}|l><l|p_\beta|0>}{(E_m-\hbar\omega_s)(E_l-\hbar\omega_i)}$$

$$+ \text{ five permuted terms.} \tag{8}$$

where H_{EL} is the electron-phonon Hamiltonian, p_α and p_β are electron momentum operators and $|0>$ is the "one electron" wave function for the ground state. Under resonance conditions $\hbar\omega_i$ and/or $\hbar\omega_s$ are close to the energies of the intermediate states E_m or E_l giving rise to large enhancements in $\chi^{(1)}_{\alpha\beta}(j)$. Figures 1a and 1b distinguish two and three band processes. The two band processes involve intraband matrix elements of H_{EL} whereas three band processes involve interband matrix elements.

Electrons interact with optical-phonon type lattice excitations via atomic deformation potential and through their associated macroscopic electric fields.i.e.,

$$H_{EL} = H^D_{EL} + H^F_{EL} + H^{TEM}_{EL} \tag{9}$$

H^D_{EL} represents the deformation potential interaction, which is due to the modulation of the crystal periodic potential by the relative atomic displacement of the phonons. H^F_{EL} represents the electron-macroscopic longitudinal electric field interaction, namely, the Frolich interaction and H^{TEM}_{EL} corresponds to the electron-macroscopic transverse electromagnetic field interaction. The contribution due to the

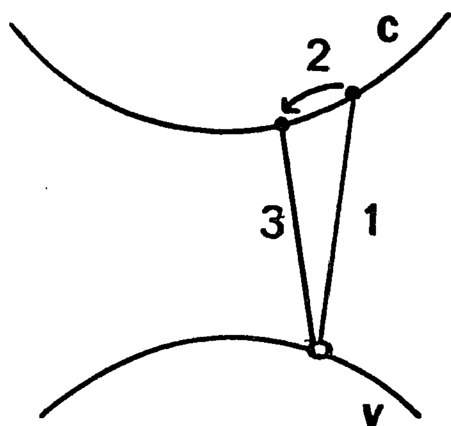

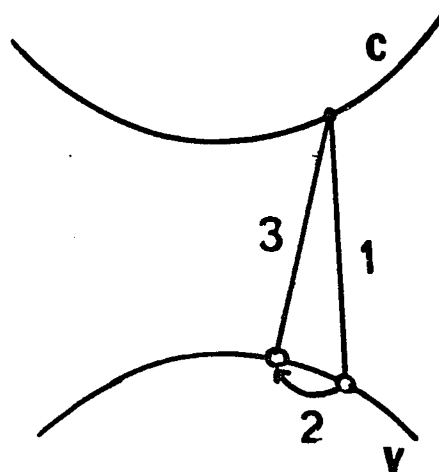

i) electron-phonon scattering ii) hole-phonon scattering

FIG. 1a. Two band Raman scattering.

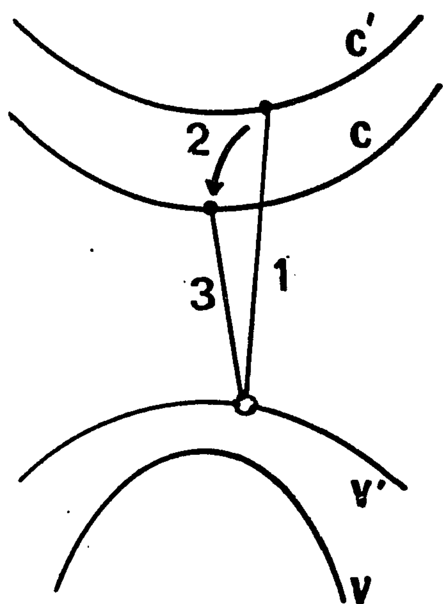

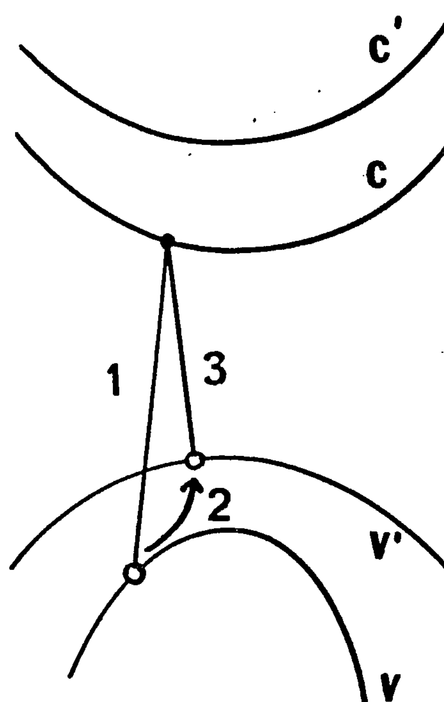

i)electron-phonon scattering ii) hole-phonon scattering.

FIG. 1b. Three band Raman scattering.

deformation potential interaction to the susceptibility tensor can be written as:

$$\chi^{D}_{\alpha\beta} = [(\partial\chi/\partial Q_j)]\ Q_j \tag{10}$$

Due to the short range nature of the deformation potential interaction, the wave vector dependence from this contribution to the susceptibility tensor is negligible. Both two band and three-band contributions are important in this case.

The macroscopic electric field associated with the optical phonons and polaritons can be written as[25]:

$$E_j = (4\pi N e^*/\varepsilon_\infty)[(\omega_T^2-\omega^2)/(\omega_L^2-\omega_T^2)]Q_j \tag{11}$$

where ω_T and ω_L are the TO and LO (q=0) phonon frequencies, N is the density of unit cells, e^* is the Born or transverse effective charge and ε_∞ is the high frequency dielectric constant.

The contribution from the macroscopic electric fields of the optical modes can be separated to q independent three-band terms and q-dependent two-band terms[25]. The q independent three-band contribution can be written as:

$$\chi'''_{\alpha\beta}(j) = [(\partial\chi/\partial E_j)(\partial E_j/\partial Q_j)]\ Q_j \tag{12}$$

The q independent contributions to the first-order susceptibility which is the "allowed" scattering is the sum of $\chi^{D}_{\alpha\beta}$ and $\chi'''_{\alpha\beta}$, i.e.,

$$\chi^{(1)}_{\alpha\beta}(j) = [(\partial\chi_{\alpha\beta}/\partial Q_j)+(\partial\chi_{\alpha\beta}/\partial E_j)(\partial E_j/\partial Q_j)]\ Q_j \tag{13}$$

To see the wavevector dependence in the case of LO phonon-Frolich interaction, we look at the matrix element

$$<\beta|H^{F}_{EL}|\alpha> = \pm ie<\beta|e^{-iq_j\bullet r}|\alpha>E_j/q_j \tag{14}$$

(+) and (-) signs correspond to the hole and electron contributions. In the two band process involving q_j=0 phonon modes $|\alpha>$ and $|\beta>$ belong to the same band. Hence $<\alpha|e^{-iq_j.r}|\beta>$ --> 1 and the contribution from scattering from the conduction electron and that from the scattering valence hole exactly cancel with each other. Thus the first nonvanishing term is linear in q_j.

In addition to the allowed scattering mechanisms other perturbations (applied or built-in electric field, stress etc.) may also affect the phonon induced change in the susceptibility thus contributing to the

first order Raman scattering. Including these contributions we obtain[21,26]:

$$\chi^{(1)}_{\alpha\beta}(\omega_i,\omega_s) = (\partial\chi_{\alpha\beta}/\partial Q_j)Q_j + (\partial\chi_{\alpha\beta}/\partial\nabla Q_j)iQ_jq_j + (\partial\chi_{\alpha\beta}/\partial Q_j\partial E_a)Q_jE_a + (\partial\chi_{\alpha\beta}/\partial Q_j\partial\eta)Q_j\eta + \quad (15)$$

$$\chi^{(1)}_{\alpha\beta}(\omega_i,\omega_s) = \chi^{(1)}_{\alpha\beta}(j) + i\chi^{(1)}_{\alpha\beta q}(j) + \chi^{(1)}_{\alpha\beta E}(j) + \ldots \quad (16)$$

where we have expanded $\chi^{(1)}_{\alpha\beta}$ in Q_j, ∇Q_j, E_a (the applied electric field) and η the strain. $\chi^{(1)}_{\alpha\beta}(j)$ which depends only on Q_j describes the "allowed" one phonon scattering. $\chi^{(1)}_{\alpha\beta E}(j)$ describes the contribution to the first order Raman scattering due to the field induced atomic displacements. $\chi_{\alpha\beta q}$ represents the linear q-dependent contribution in the case of longitudinal optic (LO) phonon-Frolich interaction and $\chi_{\alpha\beta\eta}$ represents the contribution to $\chi^{(1)}_{\alpha\beta}$ due to stress. The selection rules for scattering due to $\chi_{\alpha\beta E}$, $\chi_{\alpha\beta q}$ and $\chi_{\alpha\beta\eta}$ are usually different from $\chi^{(1)}_{\alpha\beta}$ and hence are called "forbidden" scattering.

The scattering efficiency (Raman cross section), S, defined as the ratio of the scattered intensity into unit solid angle per unit time per unit frequency interval, to the incident intensity is given by[21]:

$$S^{(1)}(j) = |\vec{e}_s \cdot \hat{\chi} \cdot \vec{e}_i|^2 \, V\omega_s^4 / c^4 \tag{17}$$

where $\vec{e}_i$ and $\vec{e}_s$ are the unit polarization vectors of the incident and scattered light, respectively, V is the scattering volume and c is the velocity of light.

2.2.1 Selection Rules

2.2.1.1 First-order scattering

For the first-order Raman scattering conservation of energy and wavevector, for a material with translational symmetry, gives (refer Fig. 2)

$$\hbar\omega_s = \hbar\omega_i \pm \hbar\omega_j \tag{18}$$

$$\hbar\vec{k}_s = \hbar\vec{k}_i \pm \hbar\vec{q}_j \tag{19}$$

i,s,j designating the incident light, scattered light and phonon, respectively.

The magnitude of the scattering wavevector depends on the scattering geometry. The largest value for $|\vec{q}_j|$ is obtained for backscattering in which case

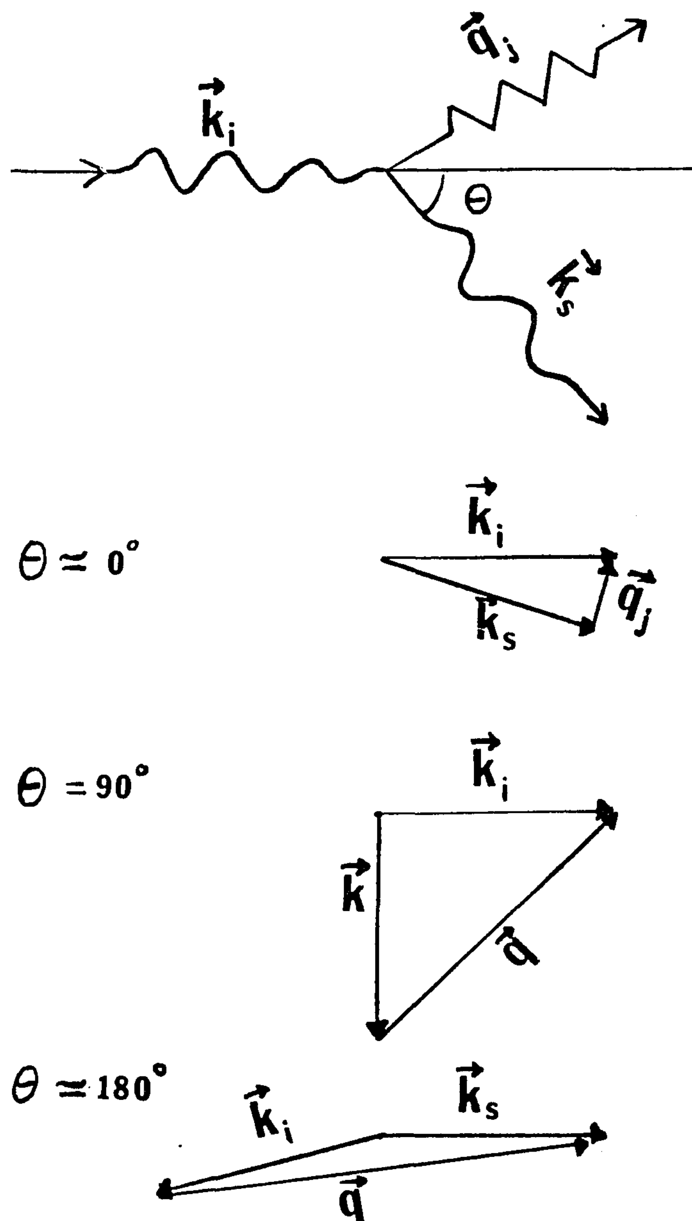

Fig. 2. Kinematics of the Stokes inelastic light scattering.

$$|\vec{q}_j| = |\vec{k}_i| + |\vec{k}_s| = \{n(\omega_i)\omega_i + n(\omega_s)\omega_s\}/c \tag{20}$$

where n is the refractive index of the medium and c is the velocity of light. In typical Raman scattering experiments (in or near visible) $\hbar\omega_i \simeq \hbar\omega_s \simeq 2.5$ ev and $n \sim 4$ and hence the maximum wavevector transfer $|\vec{q}_j| \leq 10^6\ cm^{-1}$. This is only a small fraction of the typical wavevector of the Brillouin zone (BZ) edge phonons ($\sim 2\pi/a_1 \simeq 10^8\ cm^{-1}$). Thus under conditions of wavevector conservation only phonons near the zone center i.e.,

$$q_j \simeq 0 \tag{21}$$

participate in first order Raman scattering.

In addition to the above restrictions on scattered light imposed by the kinematics of the scattering process selection rules arise for the tensor components $\chi_{\alpha\beta}$ from the crystal symmetry. From group theory, one obtains the condition for the existence of the nonzero components $\chi^{(1)}_{\alpha\beta}(j)$ as

$$\Gamma(Q_j) \otimes \Gamma_{\alpha\beta} \supset \Gamma_1 \tag{22}$$

where Γ's are the irreducible representations of the crystal point group under consideration. $\Gamma(Q_j)$ corresponds to the normal co-ordinate Q_j,

$\Gamma_{\alpha\beta}$ transforms like the components of a second-rank tensor and Γ_1 is the totally symmetric representation. Similarly the selection rule for other terms of $\chi_{\alpha\beta}$ can be written as[21,25]

$$\Gamma_{\alpha\beta q}: \quad \Gamma(Q_j) \otimes \Gamma(q) \otimes \Gamma_{\alpha\beta} \supset \Gamma_1 \tag{23}$$

$$\Gamma_{\alpha\beta E}: \quad \Gamma(Q_j) \otimes \Gamma(E) \otimes \Gamma_{\alpha\beta} \supset \Gamma_1 \tag{24}$$

$$\Gamma_{\alpha\beta\eta}: \quad \Gamma(Q_j) \otimes \Gamma(\eta) \otimes \Gamma_{\alpha\beta} \supset \Gamma_1 \tag{25}$$

$\Gamma(E)$ and $\Gamma(q)$ are irreducible representations transforming like the vectors q and E, respectively. $\Gamma(\eta)$ transforms like a second-rank tensor.

The materials under study have a zincblende structure and hence belong to the T_d point group. The optic vibrations belong to Γ_{15} representation of the T_d group which has a three fold degenerate irreducible representation at q=0.

Choosing our co-ordinate system coinciding with the crystal axes x = (100), y = (010) and z = (001) the "allowed" Raman tensor $\chi^{(1)}_{\alpha\beta}$ for the three optic modes are listed in Table I. Since the scattered intensity is proportional to $|\vec{e}_i . \hat{\chi} . \vec{e}_s|^2$ the polarization of the incident and scattered light furthur imposes restrictions on the first order scattering. For example, in backscattering from (100) surface only LO phonon is allowed.

The q-dependent and electric field induced and strain induced Raman tensors $\chi^{(1)}_{\alpha\beta q}$ and $\chi^{(1)}_{\alpha\beta E}$ and $\chi^{(1)}_{\alpha\beta\eta}$ and are also listed in Table I.[26]

The wavevector conservation given by Eqn. 21 is often relaxed due to several reasons.

1. breakdown of translational symmetry: If the scattering medium suffers complete or partial loss of translational symmetry a relaxation of the $q_j \simeq 0$ selection rule occurs. This occurs in amorphous or microcrystalline semiconductors, crystals with defects or structural disorder or in semiconductor alloys.
2. if the scattering volume is small: If d is the characterstic length of the scattering medium, phonons with wavevectors in the range $0 \le q_j \le 2\pi/d$ can participate in first order Raman scattering. Similar relaxation occurs if the penetration length of the incident light is small.

2.2.1.2 Second-order scattering.

In second-order Raman scattering two phonons participate. They may both be created or destroyed or one may be created and the other destroyed. The selection rules arising from energy momentum conservation can be written as follows:

$$\hbar\omega_s - \hbar\omega_i = \hbar\omega_j \pm \hbar\omega_l \tag{26}$$

$$\hbar\vec{k}_s - \hbar\vec{k}_i = \hbar\vec{q}_j \pm \hbar\vec{q}_l \tag{27}$$

$$\chi^{1}_{\alpha\beta} = \underset{x}{\begin{bmatrix} & & \\ & & d \\ & d & \end{bmatrix}} \quad \underset{y}{\begin{bmatrix} & & d \\ & & \\ d & & \end{bmatrix}} \quad \underset{z}{\begin{bmatrix} & d & \\ d & & \\ & & \end{bmatrix}}$$

$$\chi^{1}_{\alpha\beta q} = \underset{x}{\begin{bmatrix} cq_x & bq_y & bq_z \\ bq_y & aq_x & 0 \\ bq_z & 0 & aq_x \end{bmatrix}} \quad \underset{y}{\begin{bmatrix} aq_y & bq_x & 0 \\ bq_x & cq_y & bq_z \\ 0 & bq_z & aq_y \end{bmatrix}} \quad \underset{z}{\begin{bmatrix} aq_x & 0 & bq_x \\ 0 & aq_z & bq_y \\ bq_x & bq_y & cq_z \end{bmatrix}}$$

$$\chi^{1}_{\alpha\beta E} = \begin{bmatrix} cE_x & bE_y & bE_z \\ bE_y & aE_x & 0 \\ bE_z & 0 & aE_x \end{bmatrix} \quad \begin{bmatrix} aE_y & bE_x & 0 \\ bE_x & cE_y & bE_z \\ 0 & bE_x & aE_y \end{bmatrix} \quad \begin{bmatrix} aE_x & 0 & bE_x \\ 0 & aE_z & bE_y \\ bE_x & bE_y & cE_z \end{bmatrix}$$

Table 1a. The "allowed" Raman tensor $\chi^{1}_{\alpha\beta}$, the q-dependent Raman tensor $\chi^{1}_{\alpha\beta q}$ and the electric field induced Raman tensor $\chi^{1}_{\alpha\beta E}$.

Table Ib. strain induced Raman tensors $\chi^{1}_{\alpha\beta\eta}$

$$\chi^{1}_{\alpha\beta\eta} = \begin{bmatrix} c\eta_{yz} & f\eta_{zx} & f\eta_{xy} \\ f\eta_{zx} & e\eta_{yz} & b\eta_{xx}+g(\eta_{yy}+\eta_{zz}) \\ f\eta_{xy} & b\eta_{xx}+g(\eta_{yy}+\eta_{zz}) & e\eta_{yz} \end{bmatrix}$$

$$\begin{bmatrix} e\eta_{zx} & f\eta_{yz} & b\eta_{yy}+g(\eta_{zz}+\eta_{xx}) \\ f\eta_{yz} & c\eta_{zx} & f\eta_{xy} \\ b\eta_{yy}+g(\eta_{zz}+\eta_{xx}) & f\eta_{xy} & e\eta_{zx} \end{bmatrix}$$

$$\begin{bmatrix} e\eta_{xy} & b\eta_{zz}+g(\eta_{xx}+\eta_{yy}) & f\eta_{yz} \\ b\eta_{zz}+g(\eta_{xx}+\eta_{yy}) & e\eta_{xy} & f\eta_{zx} \\ f\eta_{yz} & f\eta_{zx} & c\eta_{xy} \end{bmatrix}$$

where j and l represent the two phonons participating in the scattering. Thus in second-order scattering wavevector transfer is not confined to that of the zone center but can take on values throughout the BZ. Structures in the second-order spectrum arise from points in the BZ where there are singularities in the combined density of states called Van Hove singularities.

2.2.2 LO - TO splitting.

In a crystal with inversion symmetry the optical branch of the phonon dispersion curve is three fold degenerate at the zone center. In any polar semiconductor the degeneracy of the longitudinal optic (LO) and the transverse optic (TO) is lifted by the long range electrostatic forces associated with the long wavelength (LO) phonons, which cause the LO phonon to oscillate at a higher frequency than the TO phonon. This may be viewed as the polar contribution (first order) to the increased spring constant for the LO phonon. The dispersion curve for Si as well as GaAs along (100) and (111) directions are shown in Fig. 3

2.2.3 Coupled LO phonon plasmon modes.

The presence of charge carriers in heavily doped semiconductors give rise to plasma oscillations with a frequency

$$\omega_p = (4\pi Ne^2/\varepsilon_\infty m^*)^{\frac{1}{2}} \qquad (28)$$

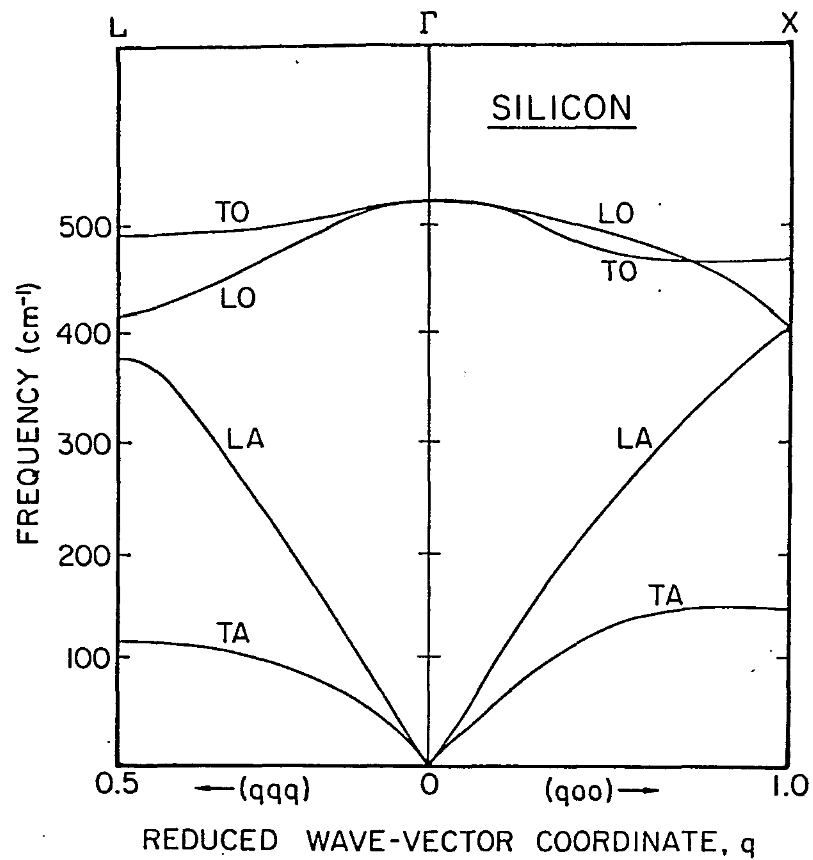

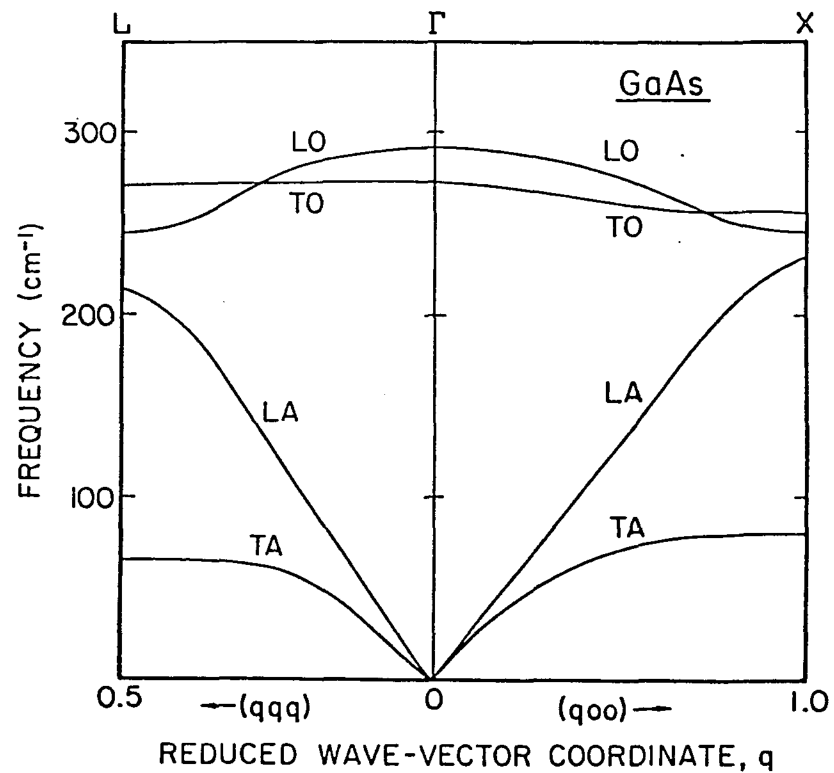

FIG. 3. Phonon dispersion curves for (a) silicon and (b) GaAs.

where ω_p is the plasma frequency, N is the number density and m^* is the effective mass of the charge carriers. ε_∞ is the high frequency dielectric constant and e is the electronic charge. If the plasma frequency is close to that of the LO phonon frequency the two modes of collective oscillations (electronic and atomic) will be strongly coupled with each other through the depolarizing field they produce.

The frequencies of the coupled LO phonon-plasmon modes are the roots of the total dielectric response, i.e.,

$$\varepsilon(q,\omega) = \varepsilon_\infty + \varepsilon_{lattice}(q,\omega) + \varepsilon_{plasma}(q,\omega) \tag{29}$$

$$= \varepsilon_\infty[(\omega_{LO}^2(q)-\omega^2)/(\omega_{TO}^2-\omega^2)] + \varepsilon_{plasma}(q,\omega) = 0 \tag{30}$$

at q=0, $\varepsilon_{plasma}(0,\omega) = \varepsilon_\infty \omega_p^2/\omega^2$ where ω_{LO} and ω_{TO} are the frequencies of the LO and TO phonons. From Eqn. 30 one obtains the frequencies of the q = 0 coupled modes as:

$$\omega_\pm(q=0)=\tfrac{1}{2}[\omega_p^2+\omega_{LO}^2\pm\{(\omega_p^2+\omega_{LO}^2)^2- 4\omega_p^2\omega_{TO}^2)^{\frac{1}{2}}\}] \tag{31}$$

where ω_{LO} and ω_{TO} are the frequencies of the LO and TO phonons at Γ point on BZ.

If $q \neq 0$ one cannot solve $\omega_{\pm}$ analytically. With increasing q the screening of the phonon field is less effective and hence ω_{-} increases from $\omega_{-}(q=0)$ which is below ω_{TO} to the asymptotic value ω_{LO}. The wavevector dependence of the ω_{+} can be obtained by replacing

$$\omega_p^2(q) = \omega_p^2 + 3/5(qv_F)^2 \tag{32}$$

in Eqn. 30 instead of ω_p^2. The quantity $v_F = hk_F/m^*$ is the Fermi velocity and ω_{LO} and ω_{TO} are the frequencies of the LO and TO phonons at the Γ point[27]. Figure 4 shows the frequencies of the coupled modes as a function of the electron concentration in GaAs, calculated for 5145 Å laser line.

2.2.4 Alloy mixed mode behavior.

Based on the behavior of the long wavelength optical phonons, alloy semiconductors can be classified into two categories, the "one mode" type and the "two mode" behavior type. In systems exhibiting "one mode" behavior each of the $q \simeq 0$ optic mode frequencies varies continously with concentration from the frequency characterstic of the one end member to the other end member. Furthermore the strength of the mode remains approximately a constant.

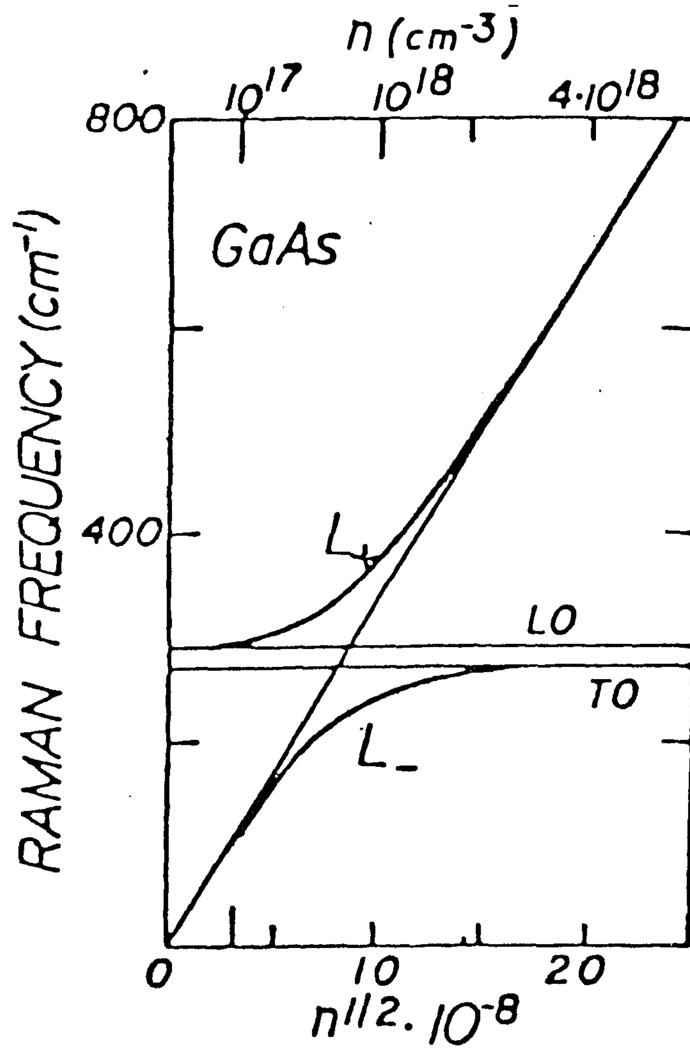

FIG. 4. The frequency dependence of the q = 0 coupled LO phonon-plasmon modes on the electron density in GaAs. (Ref. 36).

In the other class of mixed crystal systems, the "two mode" behavior type, two phonon frequencies for each of the two allowed optic modes are observed. In addition the strength of each phonon mode of the mixed crystal is approximately proportional to the mode fraction of the compound it represents. Models have been proposed to predict, depending of the mass ratios, whether a mixed crystal will exhibit "one mode" or "two mode" behavior[27-30]. Recently Gupta et al[31] have presented a model to calculate the phonon dispersion curves in mixed crystal systems. GaAlAs exhibits a "two mode" behavior in the entire composition range[32]. In the case of GaInAs although, in general, it has a "two mode" behavior, the particular $Ga_{0.47}In_{0.53}As$ exhibits an anomaly. It has been observed that $Ga_{0.47}In_{0.53}As$ has a one mode behavior[33]

2.3 Experimental details

2.3.1 Optics and electronics.

The functional block diagram of the experimental setup for Raman scattering is shown in Fig. 5. The collimated, monochromatic beam from a 6 watt Coherent Ar^+ laser was used as the incident radiation. The 5145 Å line was used in these measurements. The laser beam is reflected from two mirrors, passes through an interference filter (I.F.) having a band pass of ~ 5 Å which eliminates any spurious emissions,

(such as the plasma oscillations from the laser medium), a pin hole collimator, and is then focused onto the sample by a cylindrical lens (focal length=6 cm). The purpose of this lens was to focus the beam to a line rather than a point, thus reducing the incident power density and hence minimizing the sample heating. Typically the laser power used was ~ 250 mw. The backscattered light was collected at the entrance slit of the spectrometer by a camera lens composed of a series of lenses (focal length = 13.5 cm and f number = 1.8). The large index of refraction (~ 4) of the semiconductor ensures that both the incident and scattered angles inside the semiconductor are small (typically ~10°).

The Raman spectrometer is a Spex 1401 double monochromator which consists of two identical units. Each unit has two identical spherical mirrors and one vertically mounted grating. The gratings were holographic and were blazed at 5000 Å. A synchronous rotation of the two gratings provides a scanning in photon energy. The photons which emerge from the exit slit of the spectrometer are focussed onto the GaAs cathode of the cooled photomultiplier (RCA N-40436). The thermoelectrical cooling of the photomultiplier cathode significantly reduces the "dark current" which is due to thermionic emmisions of electrons from the cathode and dynodes even in the absence of any incident light. The anode current pulses are converted to voltage

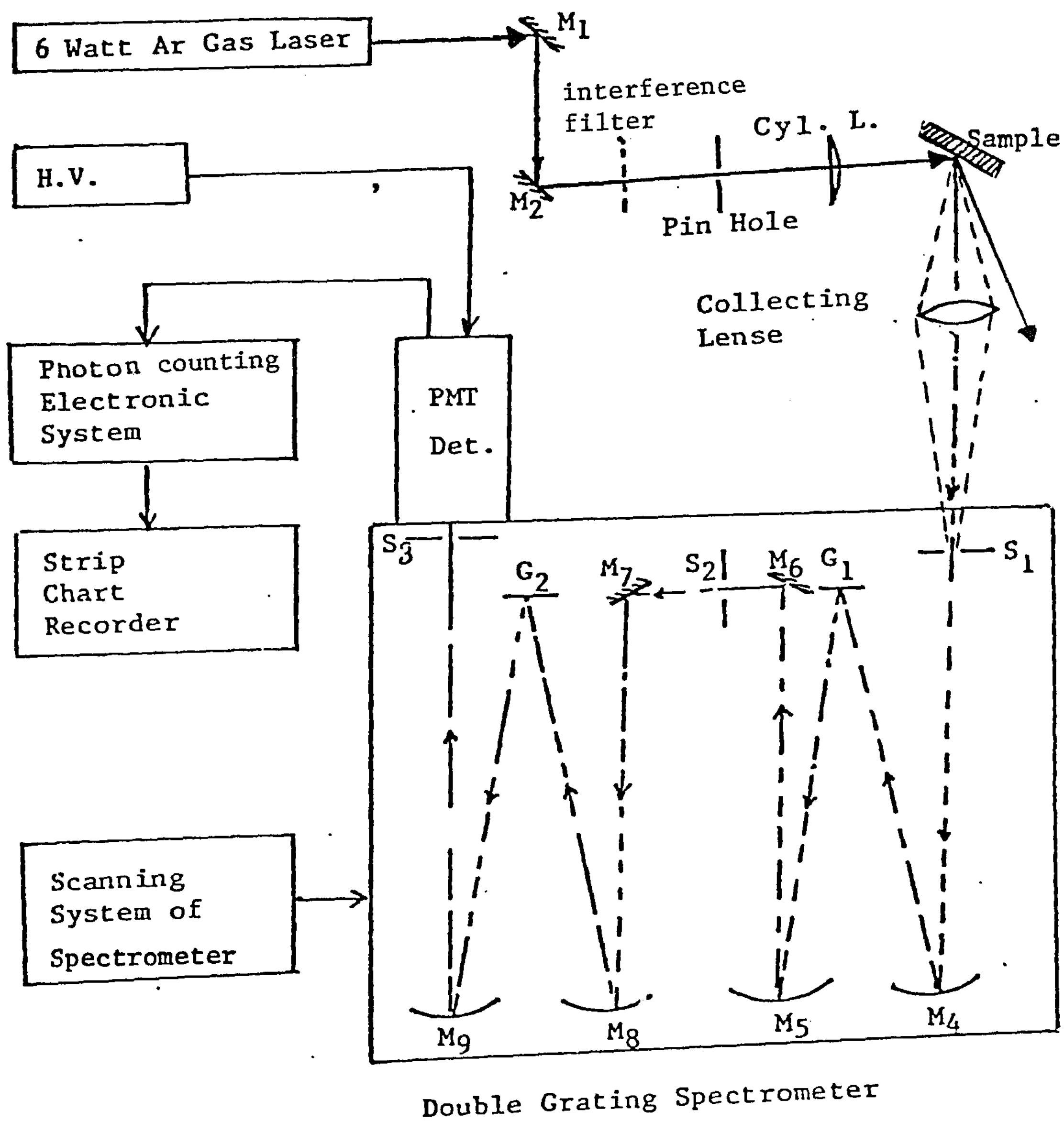

Fig. (5) Schematic functional block diagram of Raman scattering apparatus.

pulses which are fed through a discriminator which filters voltage pulses which are below a preset level thus reducing the effects of dark current. These voltage pulses are collected by a photon counting system and the time averaged results are recorded on a chart recorder.

2.3.2 Sample details.

The first part of the study was focussed on $Ga_{1-x}Al_xAs/GaAs$ hetero-structures to understand the effects of substrate preparation and growth conditions on the epitaxial layer and interface. The samples used in this study were n-n GaAlAs/GaAs heterostructures grown by different modifications of the liquid phase epitaxy (LPE) method including saturated melt mode and rapid cool modification. The thickness of epilayers (including the interface) were typically ~ 4000 Å. To form these heterostructures GaAs (100) oriented substrates doped doped with Si ($n \simeq 10^{18}$) are placed in melts of GaAlAs doped with Te to produce a carrier concentration of ~ 4×10^{16} cm^{-3}. The phase diagram in Fig. 6 illustrates the conditions for the saturated, normal and etchback melt mode of growth. In the saturated melt mode the melt is initially at two phase equilibrium. When GaAs substrate contacts with this type of melt GaAs begins to dissolve at a slow rate forming a broad interface region. Two of the samples SCL-392 and SCL-379 are grown by this procedure. For SCL-379 the GaAlAs epilayer was intentionally grown on a poor quality GaAs substrate. The third sample

SCL-400 was grown by rapid cool modification of the LPE. In this growth procedure the melt in contact with the substrate is allowed to cool more rapidly thus forming a sharper interface.

The second part of the study deals with microscopic alloy disorder in ternary alloy semiconductors. The samples investigated include several samples of $Ga_{1-x}Al_xAs/GaAs$ ($0 \le x \le 0.9$) and $Ga_{0.47}In_{0.53}As/InP$. The samples prepared by a variety of growth techniques including molecular beam epitaxy (MBE), vapor phase epitaxy (VPE), metallo-organic vapor phase epitaxy (MOCVD) and liquid phase epitaxy (LPE). All the samples were grown lattice matched to the substrate material. The various samples used in this study were kindly provided by Dr. Jerry Woodall of IBM, Dr. Gary Wicks of Cornell university, Dr. Tom Pearsall of Bell Labs and Dr. Nick Bottka of NRL. All the measurements were performed at room temperature on "as grown" sample surfaces.

2.4 Experimental Results.

2.4.1 Characterization of epilayer, interface and substrate.

In this section we discus the results of the Raman scattering investigation of both the epitaxial layer, interface and substrate of GaAlAs/GaAs heterostructures prepared under different growth parameters. Raman signals were obtained from both the epilayer and

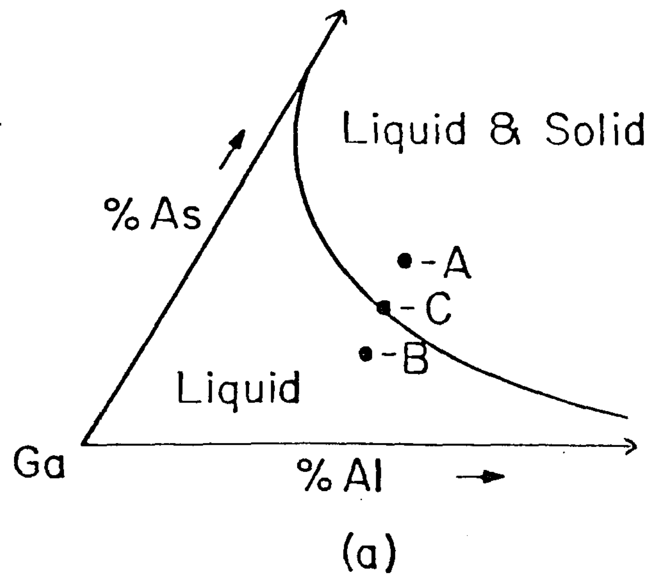

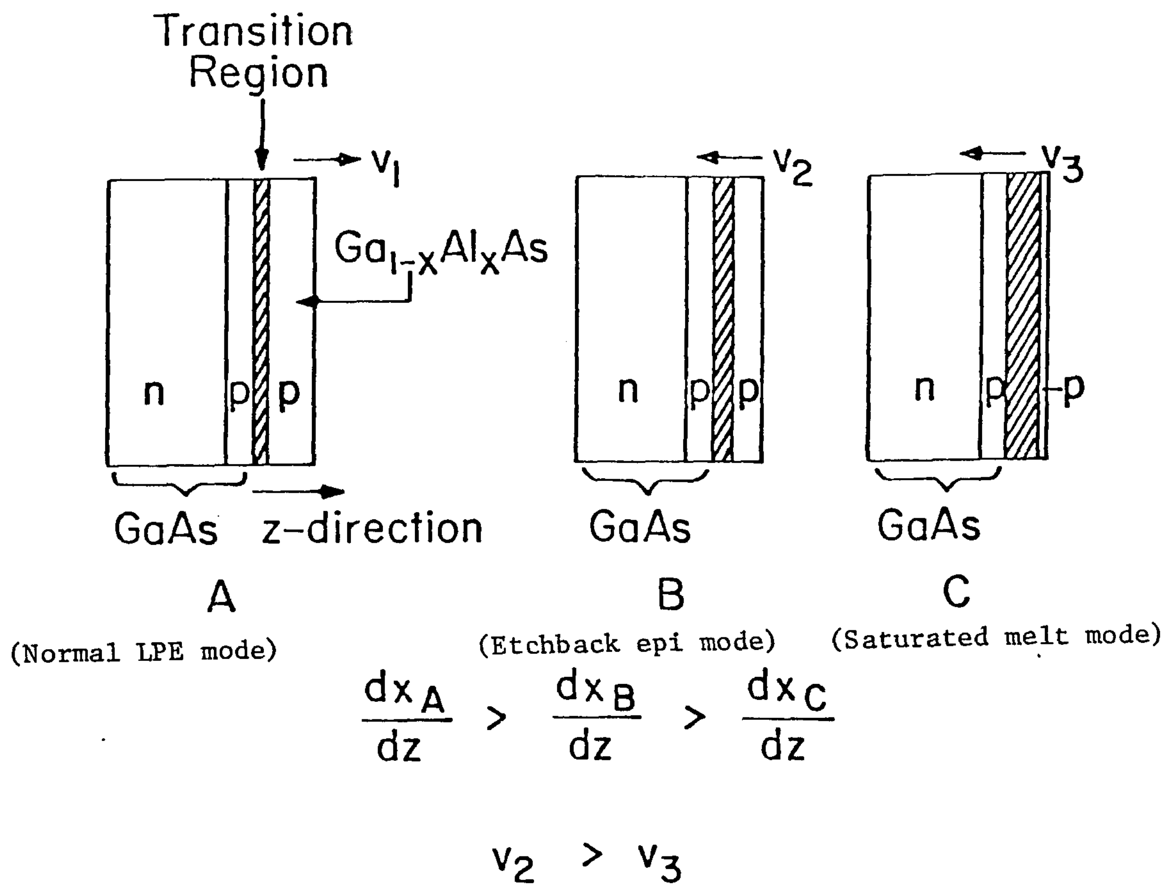

FIG. 6. Schematic representation of the phase diagram for the liquid phase epitaxial growth of $Ga_{1-x}Al_xAs$.

the substrate at the interface. Information was obtained about (a) composition x of the $Ga_{1-x}Al_xAs$ epilayer, (b) crystalline quality, (c) band bending at the interface, (d) carrier depletion from the GaAs substrate, and (e) carrier concentration of the GaAs substrate material[34].

Figures 7a, 8a, and 9a display the Raman spectra of GaAs substrate samples E-820, E-1068 and A-1319, respectively, which were used in growing the $Ga_{1-x}Al_xAs$ epilayers of samples SCL-392, SCL-400 and SCL-379, respectively. Sharp structures at 269 cm^{-1} (denoted by L_-) and 292 cm^{-1} (denoted LO) are to be seen in Figs. 7a and 8a. The upper right hand corner of both these figures exhibits a broad peak (denoted L_+) which occurs at about 560 cm^{-1} for sample E-820 and 620 cm^{-1} for sample E-1068. Both peaks have some sharper structure, designated 2TO(X) and 2TO(L), superimposed on them. These features are due to second-order two phonon Raman scattering, i.e., 2TO phonon at X, etc[35]. Features around 165 cm^{-1} are observed in both these figures and are due to other second-order scattering {2TA(K), etc}. The L_- and L_+ features of Figs. 7a and 8a are the coupled plasmon-LO phonon modes[36,37] which are observed for (100) GaAs samples with $n \geq 5 \times 10^{17}$ cm^{-3}. The fact that we observe a peak at the position of the uncoupled or "bare" LO mode (i.e., 292 cm^{-1}) in E-820 and E-1068 samples is evidence for the presence of a fully depleted

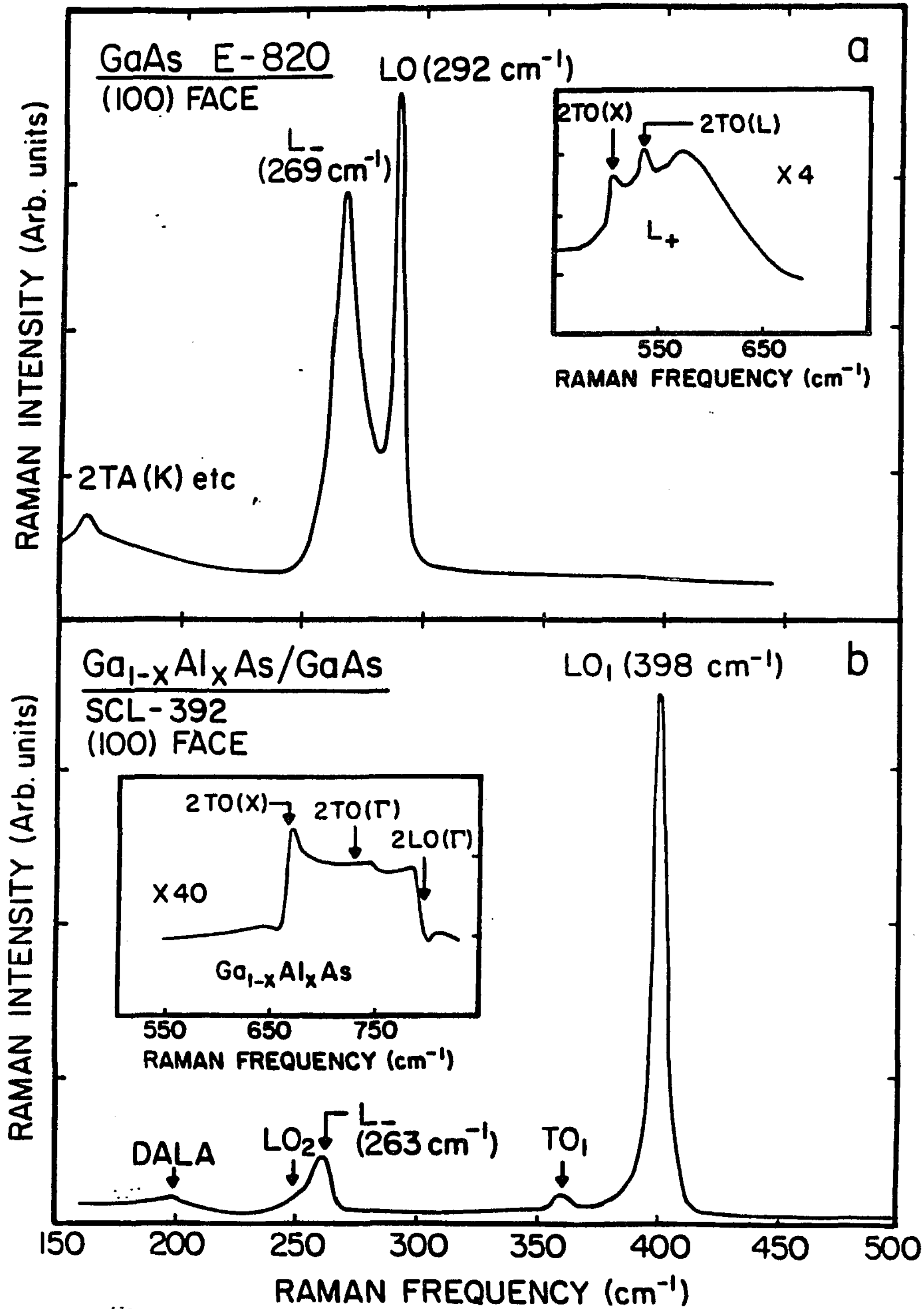

FIG. 7a. Raman spectrum of GaAs E-820, the substrate used for growing SCL-392
7b. Raman spectrum of $Ga_{1-x}Al_xAs/GaAs$ sample SCL-392.

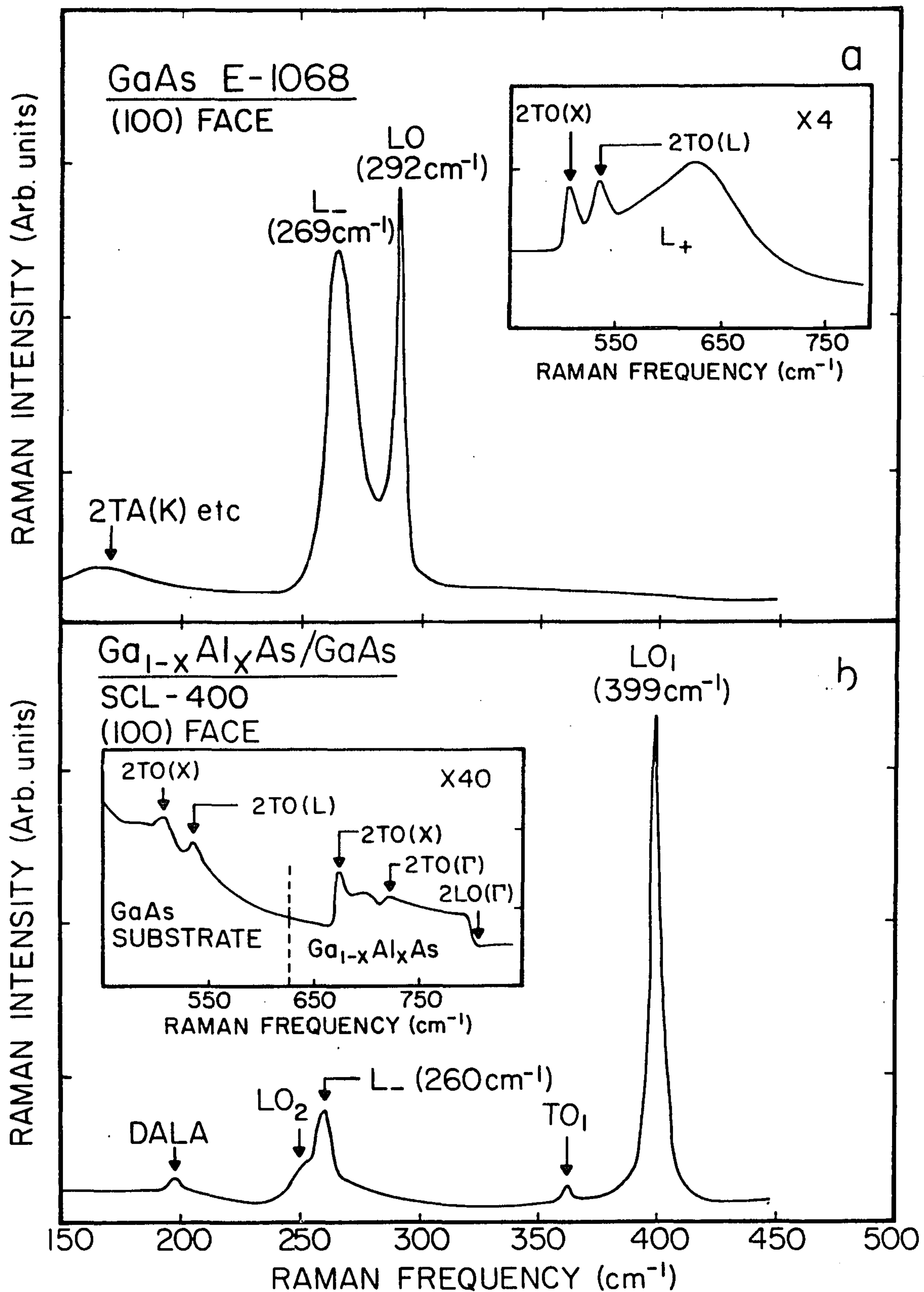

FIG. 8a. Raman spectrum of GaAs E-1068, the substrate used for SCL-400.

8b. Raman spectrum of $Ga_{1-x}Al_xAs$/GaAs sample SCL-400.

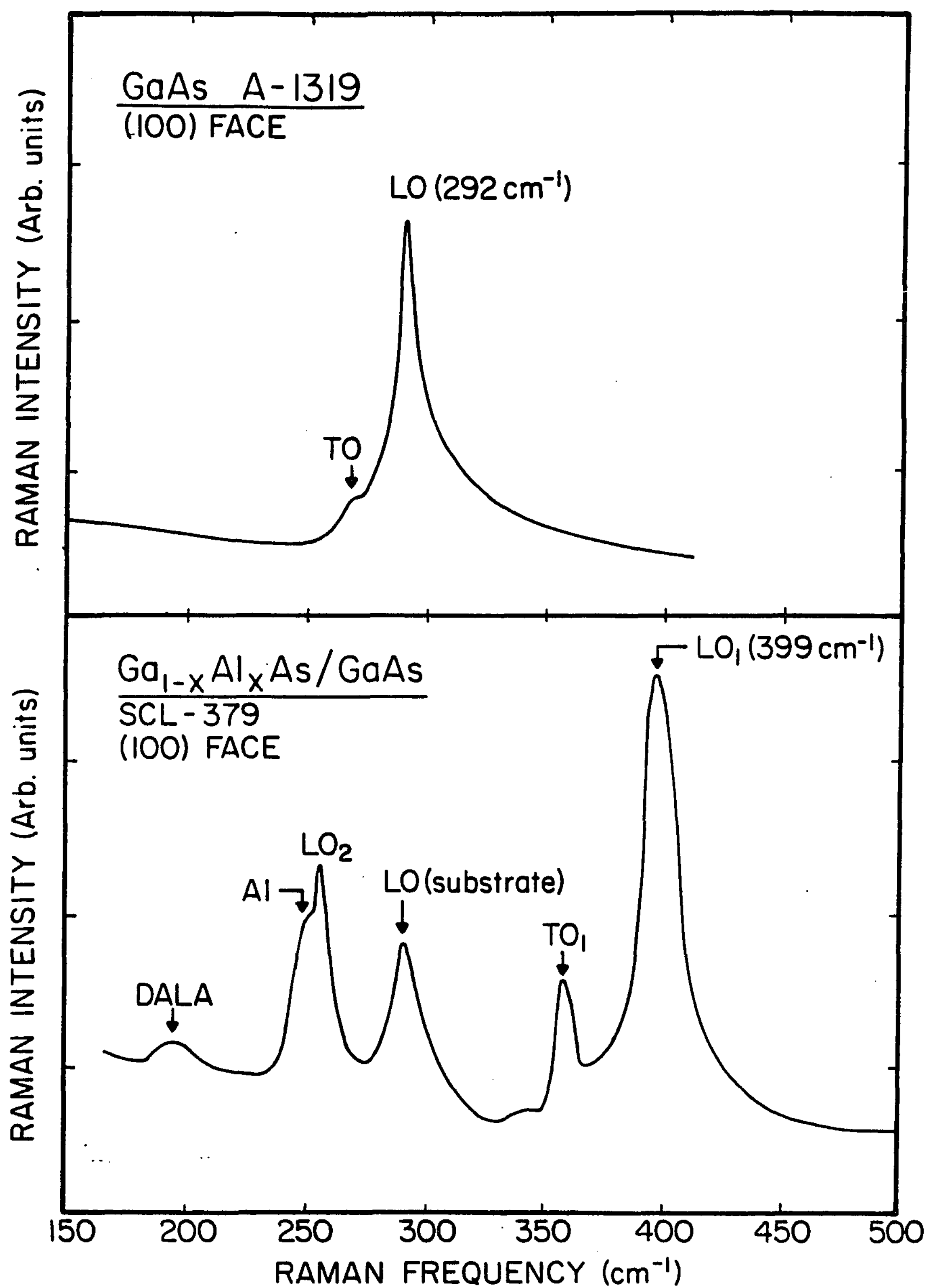

FIG. 9a. Raman spectrum of GaAs A-1319, the substrate used for growing SCL-379.
9b. Raman spectrum of $Ga_{1-x}Al_xAs/GaAs$ sample SCL-379.

space charge layer at the surface[36]. The penetration depth of the light is sufficiently large at 5145 Å so that Raman signals are seen from both (a) bulk material, (L_- and L_+) and (b) the fully depleted region i.e., "bare" LO mode. The linewidth at half maximum, corrected for instrumental resolution) for the bare LO mode is $\Gamma = 3.9\ cm^{-1}$ for sample E-820 while for sample E-1068, $\Gamma = 3.8\ cm^{-1}$.

Figure 9a the Raman spectra of sample A-1319, shows no coupled modes, but has very broad LO peak ($\Gamma \approx 10 cm^{-1}$) and a clearly detectable symmetry forbidden TO mode at $\sim 267\ cm^{-1}$. The absence of coupled modes shows that $n \leq 5 x 10^{17}\ cm^{-3}$. The linewidth of the LO peak suggests that the damage in this substrate is equivalent to the strains produced by polishing with a grit of ~ 1.5 μm in size[38]. The poor quality of this substrate was not confined to the surface region but extended through the bulk. We observed no significant change in the Raman spectrum even after the removal of ~ 100 μm of material and the subsequent preparation of the surface, i.e., mechanical polishing with 1μm grit and then using 0.05μm followed by a chemo-mechanical polishing with syton.

Figures 7b and 8b show the Raman spectra of $Ga_{1-x}Al_xAs/GaAs$ samples SCL-392 and SCL-400, respectively. Signals are observed from both the epilayer and the GaAs substrate at the interface. The latter is seen since for x~0.9, $Ga_{1-x}Al_xAs$ is an indirect gap material and

hence the absorption coefficient is small enough at 5145 Å to allow sufficient light to penetrate the epilayer into the interface. Both of the above figures reveal two LO modes [36,37,40] i.e., LO_1 the "AlAs-like" mode at $\sim 400\ cm^{-1}$ and LO_2 the "GaAs-like" mode at $\sim 250\ cm^{-1}$. The former mode has a linewidth of $\Gamma = 4.4\ cm^{-1}$ for sample SCL-400 and $\Gamma = 5.4\ cm^{-1}$ for SCL-392. A small signal from the symmetry forbidden TO_1 mode ($\sim 364\ cm^{-1}$) is observed in both figures. The disorder activated longitudinal acoustic (DALA) mode $\sim 200\ cm^{-1}$ is present in both the samples[37,41].

In addition to the Raman spectra from the $Ga_{1-x}Al_xAs$ epilayer a signal from the GaAs substrate was detected and is designated L_- in Figs. 7b and 8b. This feature originates from the coupled modes in the GaAs at the interface. Its position is slightly downshifted in frequency from the L_- peak in the corresponding GaAs substrate spectra (see Figs. 7a and 8a). Note also that Figs. 7b and 8b show no "unscreened" LO mode from the GaAs substrate.

The upper left hand corners of figures 7b and 8b shows the Raman spectrum between 500 cm^{-1} and 850 cm^{-1}. The structures in figure 8b to the left of the dashed vertical line, designated 2TO(X) and 2TO(L), are due to second-order two phonon Raman scattering from the GaAs substrate[35]. The other features between 650 cm^{-1} and 800 cm^{-1} in Figs. 7b and 8b are the second-order Raman scattering from the

epilayer. These Raman structures are identified as 2TO(X), 2TO(Γ) and 2LO(Γ)[42].

Figure 9b displays the Raman spectrum from $Ga_{1-x}Al_xAs$/GaAs sample SCL-379. From the epilayer we have observed the LO_1 peak (Γ ~ 13 cm^{-1}), symmetry forbidden TO_1 structure as well as the LO_2 mode, DALA peak and an acoustic local (AL) mode[32,35]. From the GaAs substrate at the interface we have been able to detect the signal from the LO mode.

2.4.1.1 Band bending and carrier depletion .

At the surface of n-GaAs if the Fermi level is pinned there exists a depletion space charge region, the width of which depends on the carrier concentration. If the penetration depth of the incident light is larger than the depletion width Raman spectrum can be observed from both the carrier depleted region and the bulk material. Experimentally, when the 5145 Å laser line is used, the coupled modes can be seen only if the carrier concentration is > $5x10^{17}$ cm^{-3}. This is because the depletion layer thickness becomes larger than the penetration depth of the light at lower carrier concentration, exhibiting only the "unscreened" LO mode. In this region, as shown in Fig. 4, the frequency of the L_+ varies strongly with the carrier concentration, where as the L_- frequency has only a weak dependence on the carrier concentration. From Fig. 4, knowing the frequency position of the L_-

and L_+ mode the carrier concentration of the GaAs bulk region can be easily determined. We find $n = (2.7 \pm 0.1) \times 10^{18}\ cm^{-3}$ and $n = (3.3 \pm 0.1) \times 10^{18}\ cm^{-3}$ for samples E-820 and E-1068, respectively.

The absence of the "unscreened" LO mode from the $Ga_{1-x}Al_xAs$/GaAs interface in the Raman spectra of SCL-392 and SCL-400 shows that there is no band bending at the interface and hence the absence of a depleted space charge layer at the interface.

The downshift of the L_- peak of Figs. 7b and 8b in relation to its position in Figs. 7a and 8a is evidence for a slight depletion of carriers in the interfacial region of the GaAlAs/GaAs heterostructure. This slight reduction in carrier concentration is probably due to a change in the n-type doping level in the GaAs surface region rather than to other effects, e.g., band bending due to interface states. A lowering of the doping concentration at the GaAs surface is expected from crystal growth considerations. First, since the GaAs substrate is doped with Si at about $3 \times 10^{18}\ cm^{-3}$ and since the LPE melt is not doped with the Si, the dopant is expected to outdiffuse from the GaAs substrate into the LPE melt. Secondly, the Te concentration in the melt would result in a doping level of about $10^{17}\ cm^{-3}$ for the LPE growth of pure GaAs (it leads to a doping of $\approx 2.4 \times 10^{16}$ for $Ga_{0.15}Al_{0.85}As$)[43]. Thus, due to Si outdiffusion and low Te doping levels, the GaAs surface layer would be expected to have a lower doping concentration than the bulk. From

the position of the L_- peak position the carrier concentration on the GaAs substrate, after the epilayer was grown, can be estimated. We find the carrier concentration to be $n = 1.3 \times 10^{18}$ in SCL-392 and $n = 1.2 \times 10^{18}$ in SCL-400.

2.4.1.2 Alloy composition

The mode frequencies in $Ga_{1-x}Al_xAs$ as a function of the composition x has been accurately determined by Tsu et al[32] and is shown in Fig. 10. Knowing the frequency positions of the LO_1 and LO_2 using Fig. 10 the composition x of the alloy material can be determined. The alloy composition of all the three samples were found to be $x = 0.82 \pm 0.02$. The fact that we find the same composition x is indicative of the controls possible in the growth procedure.

2.4.1.3 Crystalline quality

The crystalline quality of the various samples can be compared from several aspects of the spectrum including linewidths, observation of the symmetry forbidden TO mode, and the amplitude of the disorder activated longitudinal acoustic (DALA) mode. Samples SCL-392 and SCL-400 display much narrower linewidths and, in relation to the LO_1 peak, much smaller amplitudes for the symmetry forbidden TO_1 and DALA mode. SCL-400 appears to have somewhat better crystalline quality than SCL-392. The poor quality of sample SCL-379 is not surprising in view of the strained nature of the substrate material.

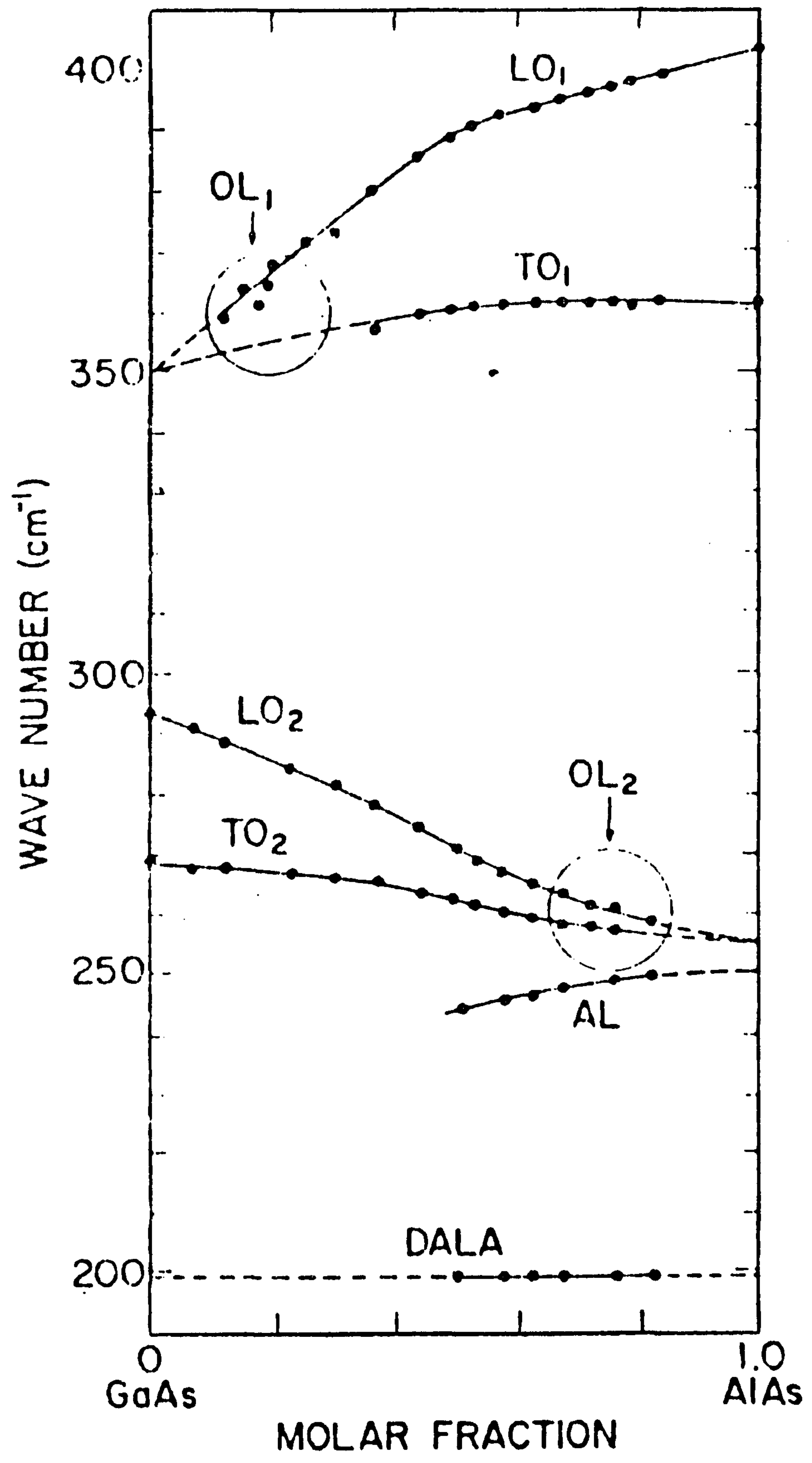

FIG. 10. Variation of the mode frequencies of $Ga_{1-x}Al_xAs$ with composition x. (Ref. 30).

2.4.2 Symmetry forbidden TO modes.

An examination of the polarization selection rules using the "allowed" Raman tensor $\chi_{\alpha\beta}$ (See Table 1a.) shows that scattering from the TO mode is forbidden from (100) surface of zincblende materials in backscattering geometry. We do observe the presence of this mode in various GaAlAs spectra as well as for the GaAs sample A-1319. Several previous investigators[44-47] have reported this forbidden scattering and was believed to be due to slight deviations from the true backscattering geometry. Abstreiter et al[31] have correlated this to the presence of thin layers of carbon at the GaAlAs/GaAs interface. Olego and Cardona[44] has attributed this violation of the selection rule to the wavevector nonconservation induced by the presence of impurities.

The effect of small deviations from the true backscattering geometry, is the same for all the samples since we use the same geometry in all the cases. On the contrary we find the symmetry forbidden mode to be significantly stronger in SCL-379 and its GaAs substrate A-1319. In addition, these modes have been seen even in true backscattering geometry (external angle of incidence ~ 5°). This suggests that the above explanation is not the main cause for this violation of the selection rule. Our results, furthur indicate that this forbidden mode is stronger in the sample which has a lower carrier concentration. Even the presence of surface electric fields does not give rise to TO phonons in backscattering from (100) surface.

The existence of internal strains in the material offers one possible mechanism for the activation of these symmetry forbidden modes. An examination of the strain induced Raman tensor $\chi_{\alpha\beta\eta}$ shows that the presence of internal strains of the form η_{xy}, η_{xy} can indeed give rise to the TO mode. The presence of internal strain is furthur substantiated by the increased line broadening in sample A-1319. The GaAlAs sample grown on this substrate is also strained showing the large forbidden TO mode as well as increased linewidth for the symmetry allowed LO mode.

However, it should be noted that these type of internal strain can not be produced by an external stress since the symmetry of the internal strain produced by an external stress is the same as that of the Raman active phonons of the crystal[26]. It should be possible to see these effects in plastically deformed materials, where the crystal symmetry is not significantly altered by the deformation. This could also be due to the morphology of the surface with regions such as ridges which are not oriented along <100>.

2.4.3 Raman lineshape and microscopic alloy disorder

This section deals with Raman lineshapes in representative ternary alloys $Ga_{1-x}Al_xAs/GaAs$ and $Ga_{0.47}In_{0.53}As/InP$ and their relationship to microscopic alloy disorder. Even though there have been a number of Raman Studies on these alloy systems only recently has the

relationship between the alloy disorder and the lineshape of the allowed modes been noted[10,39,48-50]. We examine these lineshapes using a "Spatial correlation" model, based on finite phonon mode correlations related to the q-vector relaxation induced by the microscopic nature of the alloy disorder. The alloy potential fluctuations destroy the translational invariance, an effect that manifests itself as a breakdown of the usual q=0 selection rule thus leading to broadening and asymmetry of the Raman lineshape. Our interpretation makes it possible to use Raman spectra to evaluate an average "Spatial correlation" length thus obtaining insights into the microscopic nature of the alloy disorder.

Table II summarizes the characteristics of the various samples used in this study. All the GaInAs samples have the same nominal compostion as they were grown lattice matched to the InP substrate.

Figure 11 shows the Raman spectra from the <100> surface of GaAs (x=0) as well as various samples of <100> $Ga_{1-x}Al_xAs/GaAs$. In the back scattering geometry from this surface, only the LO phonon modes are allowed. We will concentrate on the LO phonon structures and hence have not displayed other features such as disorder-activated modes, small symmetry forbidden TO mode, etc. The GaAs spectrum shows a symmetric ($\Gamma_a=\Gamma_b$), Lorentzian lineshape with a natural linewidth Γ_o ($=\Gamma_a+\Gamma_b$) of 3.0 cm^{-1} (corrected for instrumental

TABLE II. Characterstics of the $Ga_{1-x}Al_xAs/GaAs$ and $Ga_{0.47}In_{0.53}As/InP$ samples in Fig. 13.

Sample	Material	Growth Technique
1	$Ga_{0.79}Al_{0.21}As/GaAs$	MOCVD
2	$Ga_{0.7}Al_{0.3}As/GaAs$	MBE
3	$Ga_{0.64}Al_{0.36}As/GaAs$	MBE
4	$Ga_{0.6}Al_{0.4}As/GaAs$	MBE
5	$Ga_{0.6}Al_{0.4}As/GaAs$	Ref. 39
6	$Ga_{0.5}Al_{0.5}As/GaAs$	LPE
7	$Ga_{0.18}Al_{0.82}As/GaAs$	LPE
8	$Ga_{0.1}Al_{0.9}As/GaAs$	LPE
9	$Ga_{0.1}Al_{0.9}As/GaAs$	LPE
10	$Ga_{0.47}In_{0.53}As/InP$	MOCVD
11	$Ga_{0.47}In_{0.53}As/InP$	LPE
12	$Ga_{0.47}In_{0.53}As/InP$	MOCVD
13	$Ga_{0.47}In_{0.53}As/InP$	MBE
14	$Ga_{0.47}In_{0.53}As/InP$	MBE
15	$Ga_{0.47}In_{0.53}As/InP$	VPE

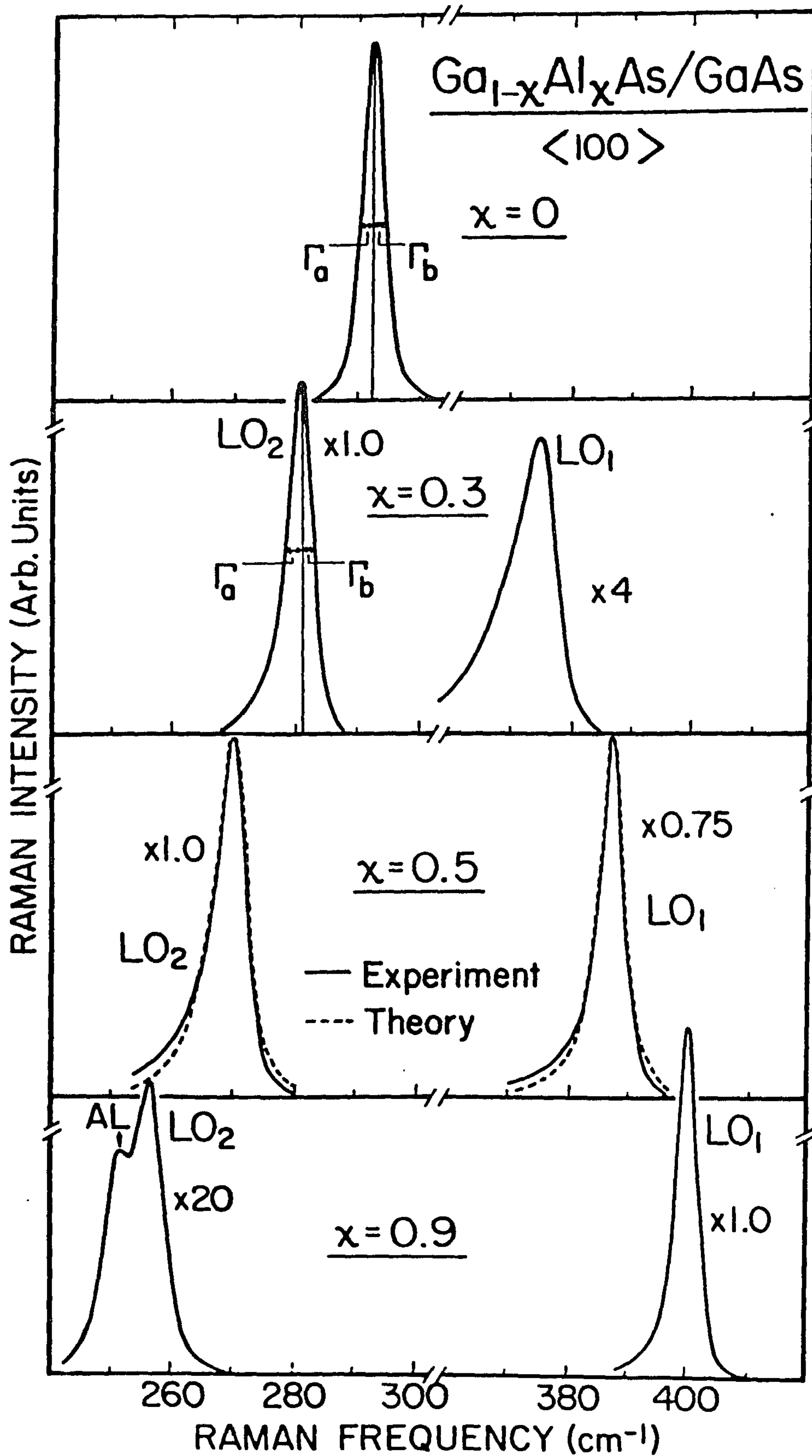

FIG. 11 . Raman spectra from (100) $Ga_{1-x}Al_xAs/GaAs$ samples.

resolution). $Ga_{1-x}Al_xAs$ exhibits a two mode behavior, i.e., an "AlAs-like" mode (denoted by LO_1) and a "GaAs-like" mode (denoted by LO_2, see Fig. 10). For the alloy samples both LO_1 and LO_2 have an asymmetric lineshape ($\Gamma_a > \Gamma_b$) that is broader than the GaAs end point material. As the Al concentration increases the LO_2 mode becomes broader and more asymmetric while the reverse is true for LO_1, i.e., it narrows and becomes more symmetric. This trend has also been noted by Barker et al[48]. For Al rich samples ($x > 0.8$) the extraction of the linewidth and asymmetry for the "GaAs-like" mode was complicated by the presence of a feature at the low energy side[32] (denoted AL in Fig. 11).

In Fig. 12 Raman spectrum from $Ga_{0.47}In_{0.53}As$/InP samples #13, #15, and #11 are displayed. The features present between 220 cm^{-1} and 260 cm^{-1} have been discussed in Refs. 33 and 51. The strong feature at 270 cm^{-1} is the "GaAs-like" LO phonon mode. We were not able to detect any significant structures at the position corresponding to the "InAs-like" LO feature[33,51]. Hence, for the purpose of this study we have focused our attention to only the "GaAs-like" LO phonon.

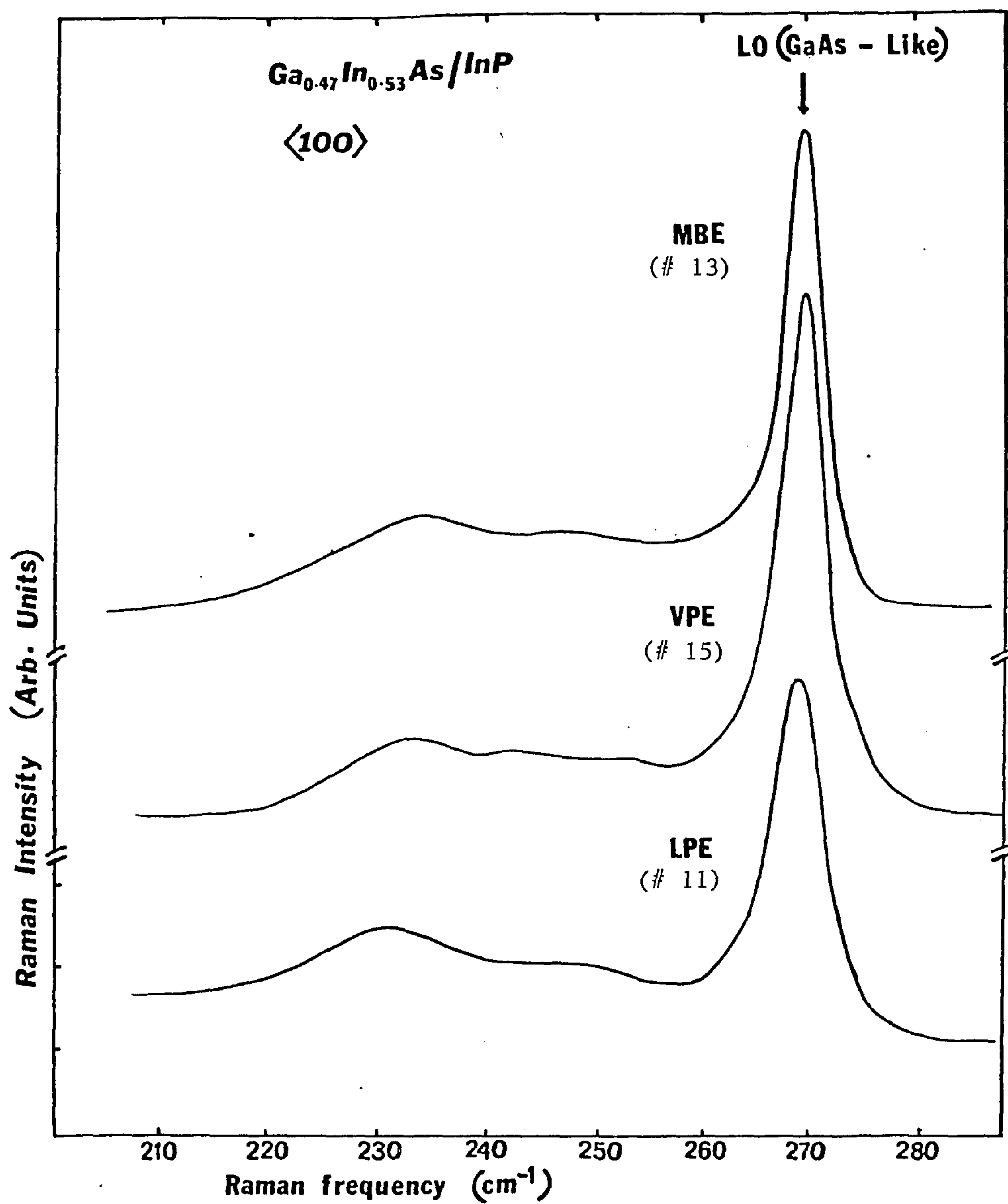

FIG. 12. Raman spectra of $Ga_{0.47}In_{0.53}As/InP$ samples at 300 K.

2.4.3.1 Spatial Correlation model

In this section we outline the "Spatial Correlation" model[52,53] to describe the q-vector relaxation induced by APF.

The cross section for light scattering is given by the Fourier transform of the correlation function of the fluctuations in the polarizability on the dielectric constant of the material. The correlation function due to fluctuations in dielectric constant can be written as

$$G(\vec{r},t) = \langle \Delta\varepsilon(\vec{r}+\vec{r}\,',t+t')\Delta\varepsilon^{*}(\vec{r},t)\rangle \tag{33}$$

where the correlation is between fluctuations in $\hat{\chi}$ at time $t+t'$ and point $\vec{r}+\vec{r}\,'$ with those at t' and $\vec{r}\,'$. The dielectric constant can be expanded in terms of the normal co-ordinate $Q_j(t)$. Then for the first order Raman scattering the correlation function becomes

$$G(\vec{r},t) = \sum_{jj'} \left\langle \frac{\partial\varepsilon}{\partial Q_j}(\vec{r}+\vec{r}\,') \quad Q_{j'}(t+t')\frac{\partial\varepsilon}{\partial Q_j}(\vec{r}\,')Q_j(t)\right\rangle \tag{34}$$

This can be separated into a spatial part and a temporal part since the time dependence appears only in the normal co-ordinate. Hence we obtain

$$G(\vec{r},t) = \sum_j \left\langle \frac{\partial\varepsilon}{\partial Q_j}(\vec{r}+\vec{r}') \quad \frac{\partial\varepsilon}{\partial Q_j}(\vec{r}') \right\rangle \langle Q_j(t+t')Q_j(t)\rangle \tag{35}$$

the summation on j' has been dropped as the normal co-ordinates are orthogonal and statistically independent. The angular brackets represents the thermal average.

From a quantum mechanical calculation one can write the time correlation function

$$\langle Q_j(t+t')Q_j(t)\rangle = \delta_{jj'} \left\{\frac{\hbar}{2\omega_j} \quad [n_j e^{+i\omega_j t} + (1+n_j)e^{-i\omega_j t}]\right\} \tag{36}$$

where we have written n_j for

$$\langle n(\omega_j, T\rangle = [\exp(\hbar\omega_j/kT)-1]^{-1} \tag{37}$$

The time Fourier transform of this correlation function becomes

$$= \delta_{jj'} \left[\frac{\hbar}{2\omega_j}\{n_j\delta(\omega_s-\omega_i-\omega_j) \quad +(1+n_j)\delta(\omega_s-\omega_i+\omega_j)\}\right] \tag{38}$$

where the two terms represents the anti-Stokes and Stokes components of the first order Raman scattering. ω_s is the scattered frequency, ω_i is the incident frequency, and ω_j is the phonon frequency.

In an ideal crystal, the wavefunction of the phonon with wavevector $\vec{q}_j$ is given by:

$$\Phi(\vec{q}_j, r) = u(\vec{q}_j, \vec{r}) e^{-i\vec{q}_j \cdot \vec{r}} \tag{39}$$

where $u(\vec{q}_j, \vec{r})$ is lattice periodic. This combined with the the small wavevector of the incident light gives rise to the usual $\vec{q}_j = \Delta\vec{q} \simeq 0$ selection rule of the first order Raman scattering. In an alloy material because of the alloy potential fluctuations (APF) the phonon wavefunctions become finite in extent. Thus in an alloy due to APF there is a relaxation of the $\vec{q}_j = \Delta\vec{q} \simeq 0$ selection rule. This q vector relaxation can be viewed in terms of a correlation length characterizing the spatial extent of the phonon wavefunction. For the ideal crystal L is infinite. A Gaussian form[54] $\exp(-2r^2/L^2)$ for the spatial decay has been successfully used to describe the q vector relaxation due to finite size effects[53] and that due to structural disorder[55] (ion damaged materials). We assume in the alloy material the phonon wavefunction to be

$$\Psi(\vec{q}_j, \vec{r}) = \{A e^{-2r^2/L^2}\} \Phi(\vec{q}_j, \vec{r}) \tag{40}$$

$$= u(\vec{q}_j, \vec{r}) \Psi'(\vec{q}_j, \vec{r}) \tag{41}$$

where L is the correlation length defining the extent of the spatial decay.

expanding Ψ' in a Fourier series:

$$\Psi' = \int d^3q C(\vec{q}_j,\vec{q})\ e^{i\vec{q}.\vec{r}} \tag{42}$$

we get the Fourier coefficients

$$C(\vec{q}_j,\vec{q}) = \{AL/2\pi^{3/2}\} e^{\{-L^2(\vec{q}_j-\vec{q})^2\}/8} \tag{43}$$

Thus because of the finite spatial extent of the phonon wavefunction $\Psi(\vec{q}_j,0)$ becomes a superposition of the eigenfunctions with q-vectors weighted through the coefficients $C(0,\vec{q})$. Since the square of the transition matrix elements appear in the scattering cross section (Eqns. 8 and 17), the Raman Intensity for the alloy material becomes:

$$I(\omega) \quad \alpha \quad \int d^3q \exp(-q^2L^2/4) \quad I_o(\omega) \tag{44}$$

where $I_o(\omega)$ denotes the spectral lineshape of the Raman line of the end point material. The spectral distribution of the end point sample is given quite accurately by a Lorenztian.

Thus we get the Raman intensity $I(\omega)$ at a frequency ω can be written as

$$I(\omega) \quad \alpha \quad \int_{0}^{1} \frac{\exp(-q^2L^2/4) \quad d^3q}{[\omega-\omega(q)]^2+[\Gamma_0/2]^2} \tag{45}$$

where q is in units of $2\pi/a$, a being the lattice conatant and $\Gamma_0(3.0cm^{-1})$ is the width (full width at half maximum) of the intrinsic Raman lineshape of the end point materials[56]. For the dispersion $\omega(q)$ of the optic phonon we take the analytical model relationship, obtained from a linear chain model[57];

$$\omega^2(q) = A+\{A^2-B[1-\cos(\pi q)]\}^{\frac{1}{2}}. \tag{46}$$

with $A=4.26 \times 10^4$ cm^{-2} and $B=7.11 \times 10^8$ cm^{-4}. Eqn. (46) reproduces quite well the dispersion of LO phonon in GaAs[58]. Similarly, the dispersion of the LO phonon in AlAs has $A=8.20 \times 10^4$ cm^{-2} and $B=2.23\ 10^9$ cm^{-4}. For simplicity we assume a spherical BZ.

A typical lineshape fit using Eqn. (45) and Eqn. (46) for the "GaAs like" and "AlAs like" LO phonon modes in $Ga_{0.5}Al_{0.5}As$ sample is shown by the dashed line in Fig. 11.

Plotted in Fig. 13 are the broadening Γ and asymmetry Γ_a/Γ_b as a function of the coherence length L as determined from Eqns. (45) and (46). The relationship calculated using the dispersion curve for AlAs and GaAs are shown by dashed and solid lines, respectively. The corresponding correlation lengths are shown on the axes marked L_1 and L_2 , respectively. All the integrations were done using trapizoidal rule. Also plotted in this figure are the experimental points for the "GaAs-like" and "AlAs-like" modes of a number of different samples of $Ga_{1-x}Al_xAs/GaAs$ as well as the "GaAs-like" mode of the various $GA_{0.47}In_{0.53}As/InP$ samples. For sample #1 the LO_1 feature was too weak to extract any meaningful Γ and Γ_a/Γ_b. Due to the presence of the AL feature on the low energy side of the LO_2 structure in samples #7, #8, and #9, we were unable to determine the linewidth and asymmetry of this feature. Also we have taken from Ref. 39 a representative experimental data point, i.e., the "GaAs-like" mode of $Ga_{1-x}Al_xAs$ for x=0.4 (sample #5). For samples #11 and #12 the data coincide and hence only one point is plotted. Representative errors in the determination of Γ and Γ_a/Γ_b are shown by vertical and horizontal bars, respectively, for the data of sample #3. The agreement between theory and the experimental points is quite good over the entire range of Γ and Γ_a/Γ_b.

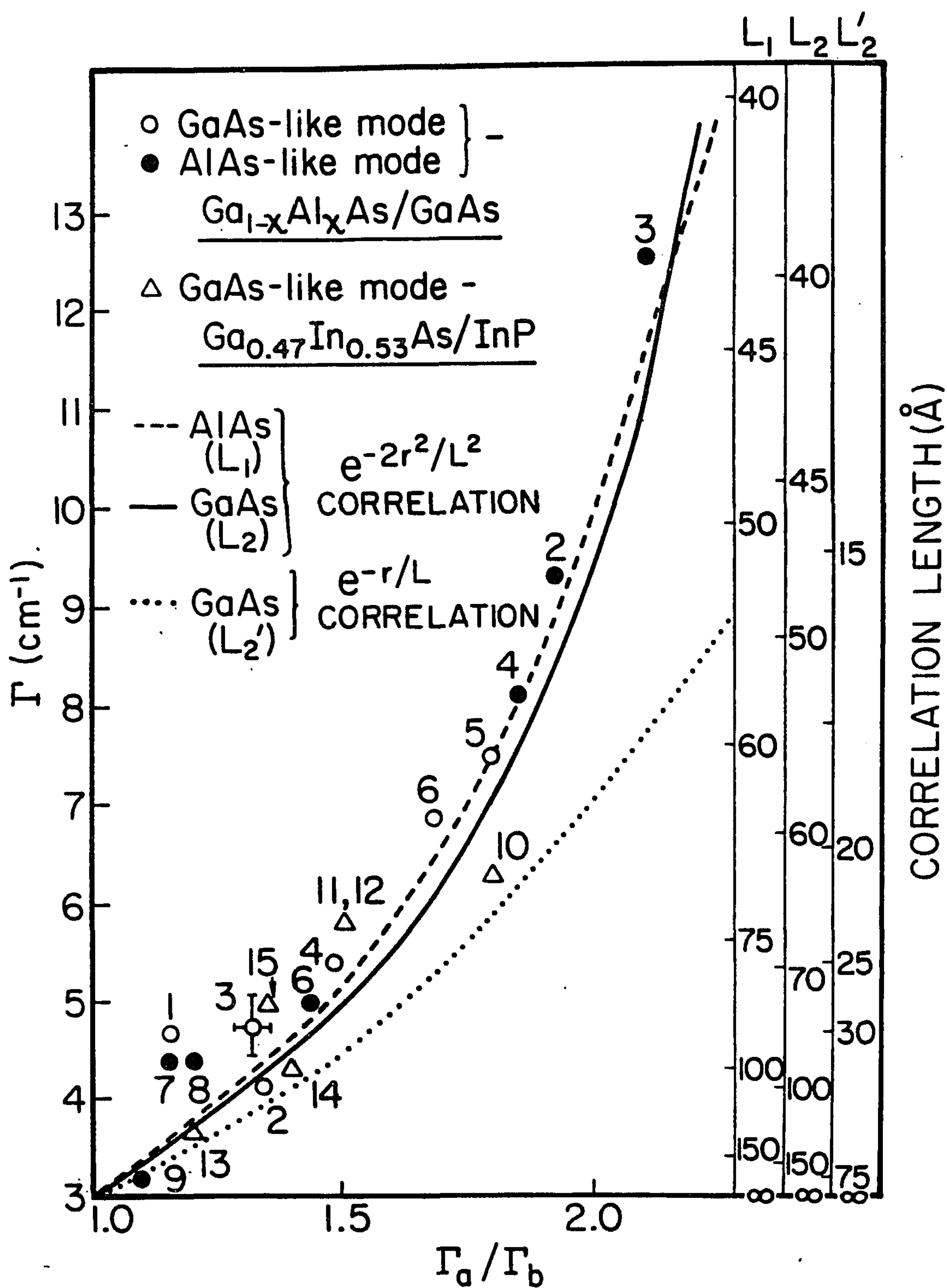

FIG. 13. The relationship between broadening Γ and asymmetry Γ_a/Γ_b as a function of correlation length L.

From Fig. 13 we note that in a given crystal of GaAlAs, the "GaAs-like" mode may have a different spatial correlation length than that of the "AlAs-like" mode. In general as the crystal becomes Al rich the correlation length of the "AlAs-like" mode increases while that of the "GaAs-like" feature decreases. The fact we find a linewidth Γ = 3.2 cm^{-1} for sample #9 (x=0.9) indicates that the natural linewidth of LO phonon in AlAs is also close to that of GaAs, i.e., 3.0 cm^{-1}. The GaInAs samples present an interesting case since they all have the same nominal composition but were prepared with different growth parameters. Figure 13 shows that there are somewhat different correlation lengths for these samples, depending not only on the growth technique but apparently on the difference in the growth conditions for the same method. For example, samples 13 and 14, both prepared by MBE have different correlation lengths. Thus, these results indicate that the microscopic alloy disorder introduced depends in general, on the growth parameters as well as the alloy composition.

The variations in broadening and asymmetry of the LO phonon Raman lines with composition can be understood as follows. In $Ga_{1-x}Al_xAs$ for small values of x (i.e., x<0.01) the Al atoms are widely separated and hence each Al atom vibrates independently of the others giving rise to a local mode, the amplitude of which is

exponentially attenuated within several interatomic distances. As the number of randomly distributed Al atoms increases the eigenfunctions of these local modes overlap and a band of allowed frequencies is formed. At these composition since there is less periodicity in the Al sublattice as compared to the Ga sublattice the correlation length of the former is smaller than the latter. As the composition increases there is an increase in the ordering of the Al sublattice and hence the correlation length becomes longer while the reverse is true for the Ga sublattice which is consistent with our observations. A similar behavior for the lineshapes for the GaAlAs system has been noted by Bonneville[10].

It has been suggested by Shuker and Gammon[52] that the phonon mode correlation can be represented by a spatial correlation function of the form exp(-r/L). We have also examined this function to calculate the Raman lineshapes. The dotted line in Fig. 13 shows the relationship between Γ and Γ_a/Γ_b calculated using the appropriate Fourier transform of this correlation function in Eqn. (45) and the dispersion curve for GaAs in Eqn. (46). The corresponding correlation lengths are shown on the axis denoted L_2'. From Fig. 13 we note that for a given asymmetry the broadening is much smaller than actually measured. Thus, it is clear that these correlation functions are not suitable to describe

the experimental results. It must be pointed out that a different form of disorder, for example point defects may require other correlation functions, depending in general on the nature of the disorder.

Jusserand and Sapriel (JS) have recently presented a model to account for the relation between alloy-induced q-vector relaxation and the asymmetry of the LO phonon mode[39]. Their model differs from ours in several important features: (a) for convenience they used a Lorenztian function to describe the q-vector distribution (as well as a Lorenztian lineshape function), (b) their integral is one dimensional in q-space (dq instead of d^3q), (c) they use a quadratic frequency dispersion which is not valid over the entire BZ and (d) to fit their data, a composition dependent intrinsic linewidth $\Gamma_o(x)$ had to be employed in the Lorenztian lineshape expression. Their use of a composition dependent broadening was probably necessitated by the inadequacy of the assumptions (a),(b) and (c). Note from Fig. 13 that it is possible to fit the experimental data of JS (sample #5) by our approach, which uses only the natural linewidth of the end point materials in the expression for the lineshape. Also JS fit the asymmetry of only the "GaAs-like" mode and only to x=0.5. Thus the "Spatial Correlation" model is much more general and the results are more comprehensive.

While it is clear that the finite extent of a phonon wave function, i.e., q-vector relaxation, can be extended to microstructural geometries such as sublattice disorder that are not microcrystalline, it was not evident that the same spatial-correlation model should be applicable in these cases. Thus this work combined with Refs. 53 and 55 shows that the spatial-correlation model of Eqn. 45 is more general than the initial application implies and therefore indicates that it results from a rather fundamental property of the effects of the disruptions of translational symmetry on phonon propagation. A Gaussian correlation function, arising from the random nature of the distribution, has been suggested by Nemanich[54]. It should also be mentioned that while the spatial correlation length has clear meaning for microcrystalline effects, i.e., microcrystallite size, and structural damage, i.e., average size of the undamaged region, its interpretation for compositional disorder is less evident. It is probably a measure of the extent to which the sublattice is ordered, since the disruption of the periodicity is the cause for the finite spatial correlation of the phonon wave function. This conclusion is furthur evidenced by the composition dependence of L_1 and L_2 for the $Ga_{1-x}Al_xAs$ system. Thus it is clear that the parameter yields valuable information about the distribution of the constituent atoms in a nominally disordered alloy.

Thus we have demonstrated that the spatial-correlation model with a single physically meaningful parameter successfully accounts for the asymmetric broadening of the LO phonon Raman lineshapes induced by APF.

Chapter III

MODULATION SPECTROSCOPY

Measurements of the optical properties of semiconductors both at the fundamental absorption edge and above have become of great interest mainly because the structure in the optical spectra can be correlated with interband transitions, and hence the bandstructure parameters of the semiconductor. Modulation spectroscopy is a powerful tool to determine the bandstructure parameters of the material.

In modulation spectroscopy some parameter of the sample being measured is varied so as to produce a change in the optical reflectance or transmittance of the solid. The optical properties may be modified directly by applying a periodic external perturbation such as electric or magnetic field, temperature, uniaxial stress, etc or a repetitive internal modulation such as wavelength modulation[3,4,59-64]. The periodic variation of the measurement parameters gives rise to sharp, differential like spectra in the region of photon energies where the refractive index changes, i.e., where optical excitation processes occur.

In an optical reflection or absorption spectrum the structures due to critical points are usually superimposed on a slowly varying background and they may often be obscured by the noise of the background. These optical structures can greatly be enhanced by the various modulation techniques.

The fundamental quantity which describes the optical response of the material is the complex dielectric function

$$\tilde{\varepsilon}(\omega) = \varepsilon_1(\omega) + i\varepsilon_2(\omega) = \tilde{n}^2 \tag{47}$$

where $\tilde{n}=n+ik$ is the complex refractive index of the material. The real and imaginary parts of $\tilde{\varepsilon}(\omega)$ are related to those of $\tilde{n}$ by:

$$\varepsilon_1 = n^2 - k^2 \tag{48}$$

$$\varepsilon_2 = 2nk \tag{49}$$

For near normal incidence, the reflectivity at the discontinous interface between two different, but homogeneous media (substrate/ambient) can be written using Fresnel's equations as

$$R = \frac{|(\tilde{n}-\tilde{n}_a)|^2}{|(\tilde{n}+\tilde{n}_a)|^2} \tag{50}$$

where $\tilde{n}$ and $\tilde{n}_a$ are the refractive indices of the material and the ambient, respectively.

The dielectric function exhibits features which are due to singularities in the combined density of states at certain points in the BZ called Van Hove singularities[65] or 'critical points'. The imaginary part of the dielectric function $\varepsilon_2(\omega)$ due to a given pair of valence and conduction bands is given by[60]:

$$\varepsilon_2(\omega) = (Q/\omega^2) \int_{E_{cv}=\hbar\omega} \frac{ds}{|\nabla_k E_{cv}(\omega)|} |\vec{e}.\vec{P}_{cv}(k)|^2 \tag{51}$$

where $E_{cv}(\omega) = E_c(\omega)-E_v(\omega)$ is the interband energy, P_{cv} is the momentum matrix elements between the given pair of valence and conduction bands, and

$$Q = (2/2\pi^3)(4\pi^2 e^2/m^2) \tag{52}$$

e and m are the electronic charge and mass, respectively. The integration is to be carried out on a constant energy surface given by $E_{cv}=\hbar\omega$. The real part ε_1 is related to ε_2 by the Kramers Kronig relationship:

$$\varepsilon_1(\omega) = 1 + (2/\pi)P\int_0^{\infty} \frac{\omega'\varepsilon_2(\omega')}{\omega'^2-\omega^2} d\omega' \tag{53}$$

The matrix elements P_{cv} between a given pair of valence and conduction bands are smooth functions of k and hence we find that structures in the dielectric function occurs whenever the gradient of the interband energy vanishes, i.e,. when

$$\nabla_k[E_c(\vec{k})-E_v(\vec{k})] = 0. \tag{54}$$

Points in k space for which Eqn. 53 is satisfied are the critical points. These critical points occur at k=0 by symmetry or at high symmetry points on the BZ boundary where $\nabla_k E_c(k) = \nabla_k E_v(k) = 0$. These may also occur along high symmetry lines, e.g.; along axes of three or fourfold symmetry.

Four types of critical points can occur between two nondegenerate bands: at a maximum, at a minimum or at either of two types of saddle points. To see the shape of the critical points, we expand the interband energy as a function of the wavevector about a critical point $\vec{k}_0$ in a power series.

$$E_{cv}=E_{cv}(\vec{k}_0)+\tfrac{1}{2}\sum_{ij}(\partial^2 E_{cv}(\vec{k})/\partial k_i \partial k_j)|_{k=k_0}(\vec{k}-\vec{k}_0)_i(\vec{k}-\vec{k}_0)_j \tag{55}$$

where indices i,j represent the co-ordinate axes x,y and z. The linear term does not appear since the gradient vanishes. Choosing a co-ordinate system which diagonalizes Eqn. 55 we get:

$$E_{cv}(\vec{k})=E_g+\hbar^2/2[(k_x-k_{x0})^2/2m^*_x+(k_y-k_{y0})^2/2m^*_y+(k_z-k_{z0})^2/2m^*_z] \tag{56}$$

where $E_g = E_{cv}(\vec{k}_0)$ and

$$1/m^*_i = 1/\hbar(\partial^2 E_{cv}/\partial k_i^2), \; i = x,y,z \tag{57}$$

are the reduced effective masses. If all the effective masses are positive the critical point is a minimum (M_0). If one (M_1) or two (M_2) masses are negative one has a saddle point. A maximum (M_3) corresponds to all masses being negative. The singular part of the dielectric function has the form

$$\varepsilon(\omega) \sim i^{r+1}(E-E_g)^{\frac{1}{2}} \tag{58}$$

at an M_r type critical point. Fig 14 shows the singular part of the dielectric constant at the four possible three dimensional critical points.

In modulation experiments the perturbation changes the dielectric function $\tilde{\varepsilon}$. Let us assume that the real and imaginary parts of the dielectric function is changed by the amounts $\Delta\varepsilon_1$ and $\Delta\varepsilon_2$, respectively. Then it can be shown that

$$\Delta R/R = \mathrm{Re}\,\{2\tilde{n}_a \widetilde{\Delta\varepsilon}/\tilde{n}(\tilde{\varepsilon}-\tilde{\varepsilon}_a)\} \tag{59}$$

$$= \mathrm{Re}\{(\alpha - i\beta)\widetilde{\Delta\varepsilon}\} \tag{60}$$

$$= \alpha(\varepsilon_1,\varepsilon_2,\varepsilon_a)\Delta\varepsilon_1 + \beta(\varepsilon_1,\varepsilon_2,\varepsilon_a)\Delta\varepsilon_2 \tag{61}$$

where α and β are the Seraphin coefficients, which have a characteristic energy dependence for most semiconductors.

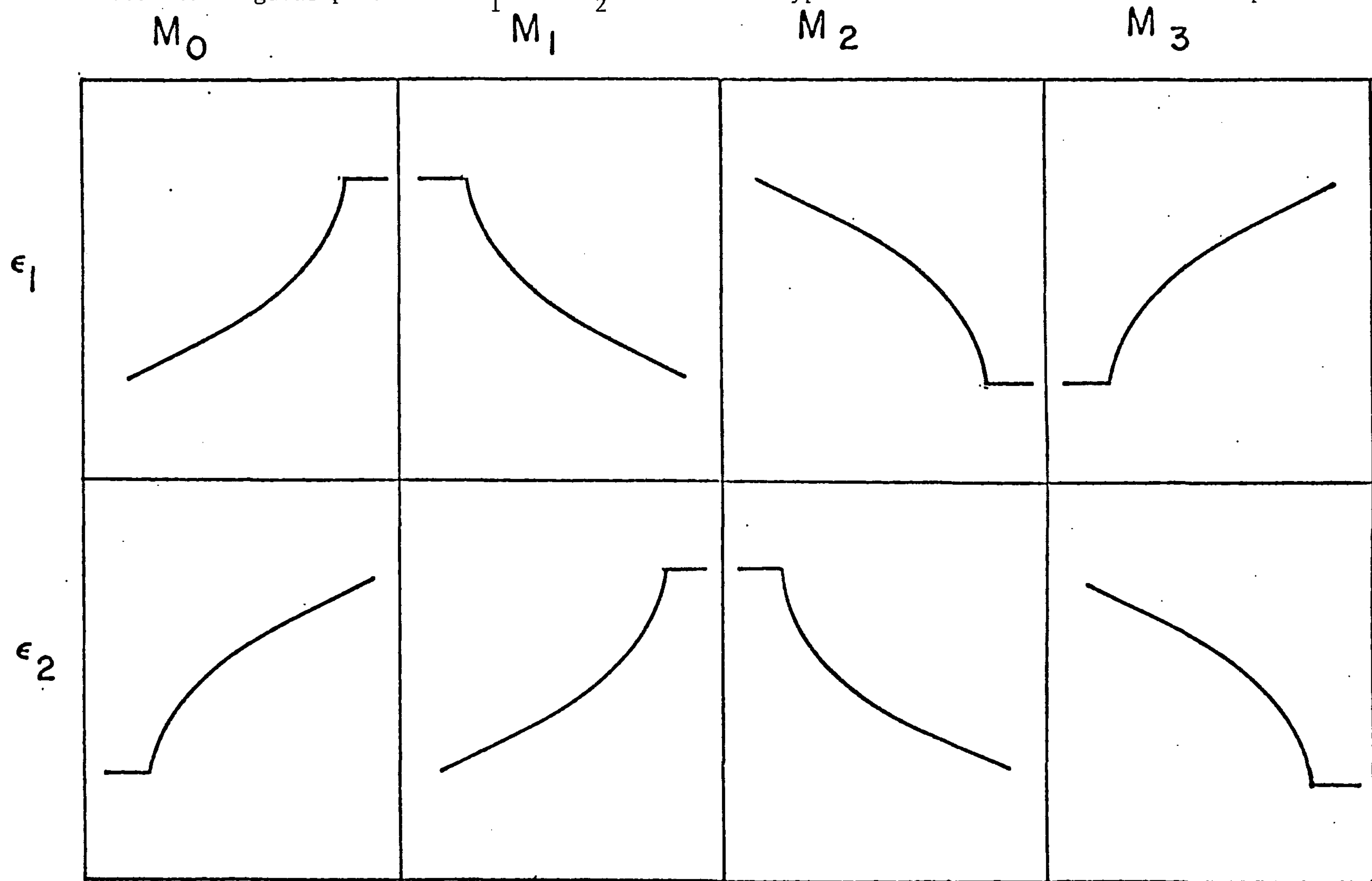

FIG. 14. Singular portion of ϵ_1 and ϵ_2 at the four types of three dimensional critical points.

3.1 Electric Field Modulation

3.1.1 Third derivative spectra.

In electric field modulation techniques, the perturbation due to an electric field $\vec{\xi}$ is $H' = e\vec{\xi}.\vec{r}$. This changes the dielectric function ε of the unperturbed solid by $\Delta\varepsilon(\vec{\xi})$. In contrast to many forms of modulation spectroscopy, the perturbation term $e\vec{\xi}.\vec{r}$ due to the electric field does not have the periodicity of the lattice, and therfore destroys the translational invariance of the Hamiltonian in the field direction. This property of the field perturbation is in effect responsible for the relationship between low field electroreflectance and the third derivative of the unperturbed dielectric function. In other modulation techniques, where the lattice periodicity of the Hamiltonian is preserved, the spectra are related to the first derivative of the unperturbed dielectric function.

Several methods can be found in the literature[66-70] for the calculation of the dielectric function in the presence of an electric field. We briefly describe the method adopted by Aspnes and Rowe[67,68], to calculate the field induced change in the dielctric function, and to show the third derivative nature of the electroreflectance lineshape under "low" electric field conditions.

The zero field dielectric function in the one electron approximation is given by[68]

$$\varepsilon_{cv} = (Q'/\pi\omega^2) \int_{BZ} d^3k \, \langle ck|G_0|ck\rangle \tag{62}$$

where

$$Q' = (4\pi^2 e^2/m^2)(2/2\pi^3)|\vec{e}.\vec{P}_{cv}|^2 \tag{63}$$

and

$$G_0 = [H_0 - E_v(\vec{k}) - \hbar\omega - i\Gamma]^{-1} \tag{64}$$

and the momentum matrix elements P_{cv} are assumed to be independent of k. H_0 is the unperturbed Hamiltonian, Γ is the broadening parameter, and $|ck\rangle$ is the Bloch state of the electron in the band c with momentum k. In the presence of a uniform electric field $\vec{\xi}$

$$H_0 \longrightarrow H = H_0 + e\vec{\xi}.\vec{r} \tag{65}$$

and

$$G_0 \longrightarrow G = G_0[1 + e\vec{\xi}.\vec{r}G_0]^{-1} \tag{66}$$

we expand G, to second order in $\vec{\xi}$ and use the transformation to the crystal momentum representation

$$\langle n'k'|r|nk\rangle \cong -i\nabla_k \delta_{nn'} \delta(k-k') \tag{67}$$

to obtain

$$\Delta\varepsilon_{cv} = \varepsilon_{cv}(\omega,\Gamma,\mathcal{E}) - \varepsilon_{cv}(\omega,\Gamma,0) \tag{68}$$

$$= (2Q'e^2/\pi\omega^2) \int d^3k \ [\frac{1}{W} \vec{\mathcal{E}} \cdot \nabla_k (\frac{1}{W} \vec{\mathcal{E}} \cdot \nabla_k \frac{1}{kW})] \tag{69}$$

where

$$W = E_{cv}(k) - \hbar\omega - i\Gamma \tag{70}$$

The above equation neglects interband tunneling. The above expression can be simplified to obtain:

$$\Delta\varepsilon_{cv}(\omega,\Gamma,\mathcal{E}) = (2Q'/\pi\omega^2) \int d^3k \ (\hbar\Omega)^3 \ [E+i\Gamma-E_{cv}(k)]^{-4} \tag{71}$$

where $E=\hbar\omega$ and

$$(\hbar\Omega)^3 = (1/8)e^2(\vec{\mathcal{E}} \cdot \nabla_k)^2 E_{cv} = e^2 \mathcal{E}^2 \hbar^2 / 8\mu_{\parallel} \tag{72}$$

where $\mu_{\parallel}$ is the interband reduced effective mass of the bands c and v evaluated in the field direction. Thus we obtain from Eqns. 62 and 71

$$\Delta\varepsilon_{cv}(E,\Gamma,\mathcal{E}) = (1/3E^2)(\hbar\Omega\frac{\partial}{\partial E})^3 E^2 \varepsilon_{cv}(E,\Gamma) \qquad (73)$$

Thus the electric field induced change is closely related to the third derivative with respect to energy of the unperturbed dielectric function.

The quantity $\hbar\Omega$ is the characteristic electro-optic energy of the system. A simple physical meaning can be given to $\hbar\Omega$ by calculating the average energy per particle, $\langle\Delta W\rangle$, absorbed in a collision period, τ for a collection of classical particles of charge -e, mass $\mu_{\parallel}$, and zero average initial velocity (zero initial current) being accelerated in a uniform field, $\vec{\mathcal{E}}$. Then we obtain:

$$\langle\Delta W\rangle = e^2\mathcal{E}^2\tau^2/(2\mu_{\parallel}) \qquad (74)$$

The lifetime, τ is related to the broadening energy Γ by $\tau = \hbar/(2\Gamma)$. If we interpret $\langle\Delta W\rangle$ as the field induced uncertainty in the unperturbed electron energies, similar to the interpretation of Γ as the lifetime induced uncertainty in these levels, then we find the ratio $\langle\Delta W\rangle/\Gamma \simeq (\hbar\Omega/\Gamma)^3$. Hence, perturbation theory and the above low field

limit is applicable to the intraband mechanism when the average energy gained per particle by acceleration in the field is small compared to the natural lifetime induced uncertainty, in the unperturbed electron energy levels. In practice the above low field limit is valid if the characteristic energy $\hbar\Omega < \Gamma$. In this limit the field enters only as a scaling prefactor $\mathcal{E}^2$. Experimentally this low field limit can be recognized whenever the spectral amplitude scales as $\mathcal{E}^2$, and no change is observed in the lineshape. Usually as a rule of thumb, this low field limit is applicable whenever $\Delta R/R \leq 10^{-4}$. Since the lineshape is field invariant, it is not necessary to use square wave modulation nor even to modulate from flatband.

Since the low-field electroreflectance (ER) structure of a single critical point is well localized to within an energy range not exeeding few broadening parameters, the actual energy bandstructure in the vicinity of a critical point can usually be replaced with a simple parabolic model as in Eqn. 55. Then from Eqn. 59 using Eqns. 71 and 56 we get:

$$(\Delta R/R) = \mathrm{Re}[Ce^{i\theta}(E-E_g+i\Gamma)]^{-n} \tag{75}$$

where C and θ are the amplitude and phase factor which vary slowly with E, and hence can essentially be considered energy independent for small changes in E. C and θ determine the amplitude and asymmetry of the lineshape respectively and Eg and Γ determine the location and width of the structure. For three dimensional critical points (i.e., all the effective masses are finite) n=2.5, and for two dimensional critical points (i.e., one of the masses is infinite) n=3 whereas n=3.5 for a one dimensional critical point. If the structure is due to an exciton, n=2.0.

The EER lineshape may be affected by the contributions of the electron-hole interaction, and also in most cases due to the inhomogenities of the perturbing electric field on the reflecting surface.

Including the contributions from these effects, we can write a generalized expression for the modulated reflectance as[71-73]:

$$\Delta R/R = \mathrm{Re}\ [C_s C_{ex} C_{in} e^i e^j \Delta\varepsilon^{ij}] \tag{76}$$

where

$$c_s = 2n_a/n(\varepsilon-\varepsilon_a) \tag{77}$$

$$C_{ex} = [1-g(\varepsilon-1)]^2 \tag{78}$$

$$C_{in} = -2ik \int dz'\ e^{-2ikz'} [\ \mathcal{E}(z')/\ \mathcal{E}(0)] \tag{79}$$

The factor $C_s = \alpha - i\beta$ gives the Seraphin coefficients, C_{ex} represents the contribution from the electron-hole Coulomb interaction and g is the exciton strength parameter, which can be assumed to be a constant for a given structure. The effect of the electron-hole interaction is to mix the singular part of ε_2 at an M_r critical point, to the singular portion of ε_2 at an M_{r+1} critical point. C_{in} is the factor arising from the electric field inhomogenity in the low field limit. In the above equation we have used the fact that $\Delta\varepsilon(\xi_p,\Gamma,E) \sim \xi_p^2$ and $k=n\omega/c$ is the wavevector of the light in the material.

In Eqn (75) the amplitude is only a scaling factor for the lineshape determined by the other variables θ, n, E_g and Γ . If the dielectric function is a slowly varying function of energy in the vicinity of the critical point then Eqn. (76) shows that the effect of the factors C_s, C_{ex} and C_{in} is essentially to change the amplitude and phase factor, leaving the energy location and width of the structure unchanged. Though additional spectroscopic information is contained in the amplitude and phase factor, a detailed knowledge of the various contributions are necessary to extract these.

3.2 Experimental Details

In this section we describe in detail the experimental setup and the details of the method in EER spectroscopy. In these modulated optical

studies, we have used the electric field modulation technique via the semiconductor/electrolyte interface. The modulating voltage is applied between the sample, whose surface is in contact with the electrolyte, and a platinum counter electrode. The electrolyte used was a 3% (by weight) tartaric acid in water, mixed with ethyleene glycol in the ratio 1:2, called the Hartnagel electrolyte[75]. In some cases the measurements were also performed using a mixture of glycerine and water in the ratio 1:4 as the electrolyte. Only a small area (typically ~ 4 mm^2) of the sample was exposed to the monochromatic incident light, and the rest being electrically insulated by covering with Miccro-stop, a commercial photoresist (Miccroproducts, Pyramid Plastic inc., 220 W, 5th street, Hope, Arkansas 71801). The electrical contacts were usually made on the back side of the sample using silver paint. In the case of samples having insulating substrates the contacts were made on the epitaxial layer itself. The $(Ga_{1-x}Al_x)_{0.47}In_{0.53}As/InP$ ($0 \le x \le 1$) samples were also biased positive with respect to the platinum counterelectrode. The biasing was adjusted in such a way that even during the negative cycle of the modulating square wave, the voltage with respect to the counterelectrode is not driven negative. This was done to prevent etching. Typical modulating voltages were ~1 V peak to peak square wave and a bias voltage ≈+0.5V. The modulating voltages were kept to a minimum so that no strong electrical conduction sets in. The ER

signal phase was monitored to detect any changes on the surface such as oxide growth etc. In the case of GaAlAs/GaAs samples, typical modulating voltage used were 1 V peak to peak and bias voltage 0.5 V. Other conditions were similar to that of GaAlInAs samples.

3.2.1 Optics and Electronics

3.2.1.1 visible and near uv

The schematic of the experimental setup for the EER system is shown in Fig. 15.

Light from a 150 watt Xenon arc is passed through the monochromator (GCA model EU 700-56). The monochromatic light coming through the exit slit was focused onto the sample by means of a spherical mirror or a lens. The sample was immersed in the electrolyte contained in a fused quartz cell, which has an optically high quality front window. The modulating voltage was a square wave at 200 Hz and was applied between the sample and the Pt counterelectrode by means of a function generator (HP model 3311 A), which also provided a reference signal to the lock-in amplifier (PAR model 186A or Ithaca model 391A). The reflected light was collected by the photomultplier tube (PMT S-1 or S-20).

The reflected light collected by the PMT had a large background light intensity corresponding to the product of the incident light

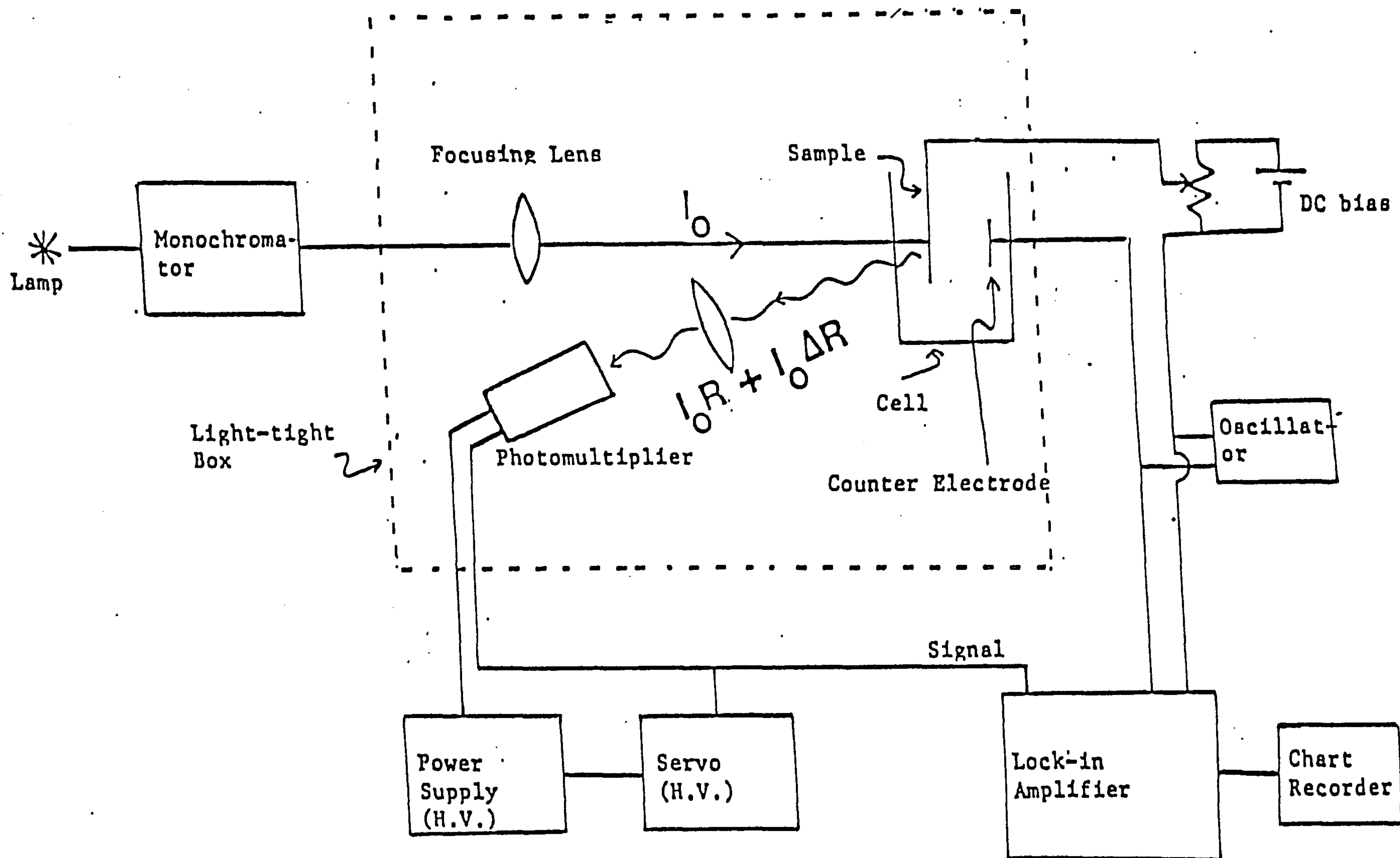

Fig. 15. Schematic functional block diagram of EER set up.

intensity I_0 and the average sample reflectivity R. Superimposed on this large background signal was a small intensity modulation with an amplitude $I_0\Delta R$, ΔR being the change in R due to the modulating field. Hence the output of the PMT contained a DC part proportonal to I_0R and an AC part proportional to $I_0\Delta R$, which varied with the modulating frequency. Hence the ratio of the AC part to the DC part gave $\Delta R/R$. The changes $\Delta R/R$ was typically $\sim 10^{-4}$. These changes can easily be detected by the usual phase sensitive detection techniques. The DC output I_0R of the PMT was fed into a servo amplifier (mechanical or electronic) which adjusted the high voltage of the PMT in order to keep the DC output I_0R, constant. The AC component of the output signal $I_0\Delta R$, is detected by the lock-in amplifier. The output signal of the lock-in amplifier is proportional to $\Delta R/R$, the relative change in reflectance. The output signal from the lock-in amplifier was connected to a chart recorder.

The servo machanism automatically corrects for any fluctuations in the reflected intensity due to - (a) changes in the incident light intensity (a common problem in arc lamps) (b) changes on the surface of the sample. Thus in normalized modulated spectra, it is not necessary to collect the entire reflected light from the sample surface since the common factor I_0 is eliminated.

For the visible and near ultraviolet regions of the spectrum the light source used was a Xenon arc lamp. An S-20 PMT was used for the wavelength region from 2000 to 8000 Å, and S-1 PMT for wavelength in the region 8000 to 11000 Å.

3.2.1.2 Infrared Range

The photoresponse of the S1 photomultiplier extends only up to ≃1.1μm. Beyond this range in the infrared, a PbS cell was used, in the photoconducting mode, as the detector. The schematic of the experimental setup using the PbS detector is shown in Fig. 16. A quartz halogen lamp was used as the light source. The monochromatic light coming from the Jarrel Ash 1/4 meter monochromator with grating blazed at 1μm was focused using a spherical lens (focal length ≃ 10 cm) onto the sample surface, which was immersed in the electrolyte. To minimize the absorption of electrolyte in this wavelength range, the sample was mounted very close to the window of the electrolytic cell thus permitting only a thin film of the electrolyte between the cell window and the sample surface. To avoid the reflected light from the front surface of the cell window reaching the detector, the window was made in a wedge shape as shown in Fig. 16. The reflected light from the sample is focused onto the PbS detector using another spherical lens (focal length = 10 cm). The signal from the PbS was fed to the Lock-in amplifier. The Lock-in output which is proportional to $I_0 \Delta R$ is

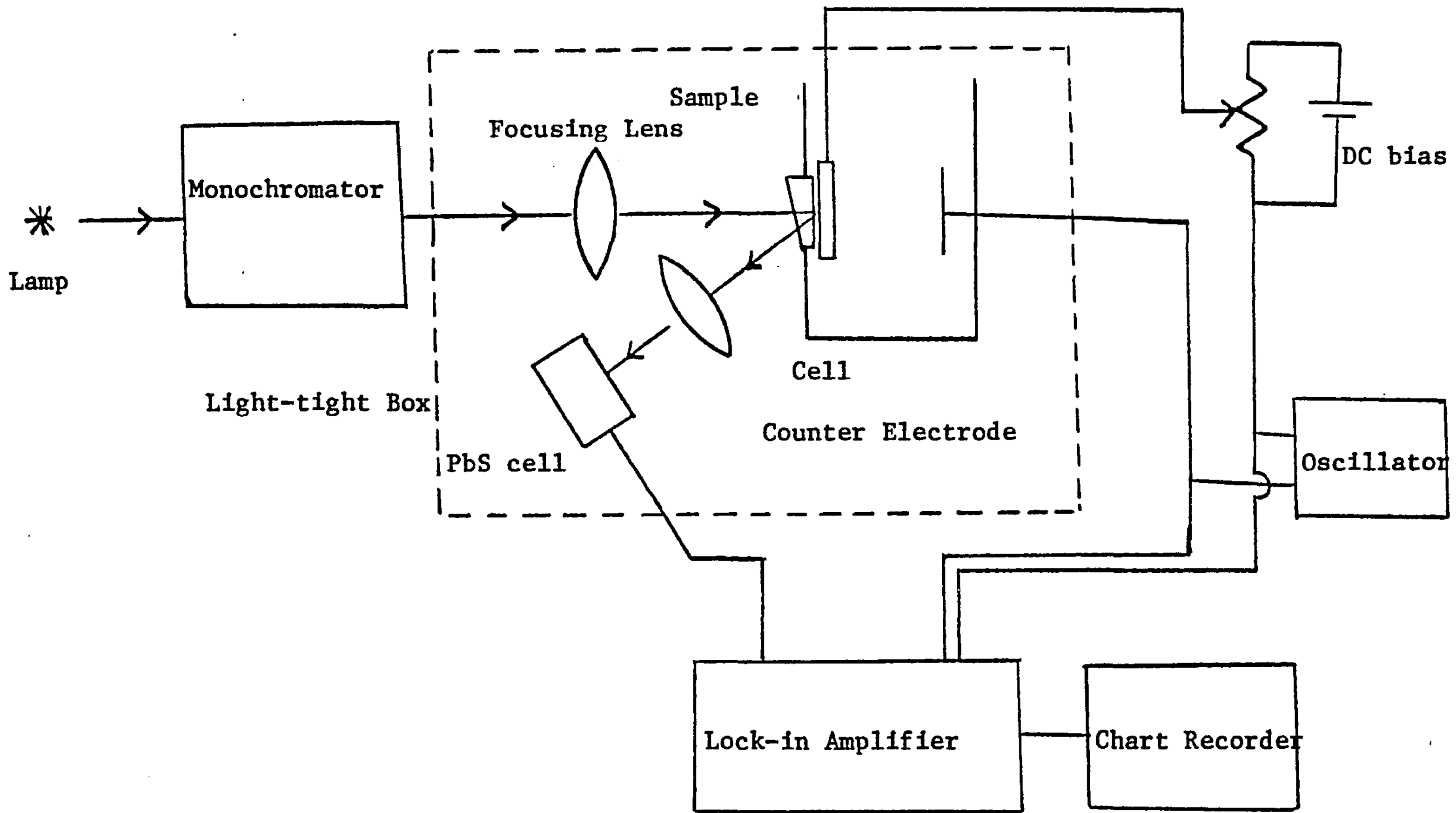

FIG. 16. Schematic of the electrolyte electroreflectance setup in infrared region.

recorded on the chart recorder. The signal proportional to I_0 was measured separately by chopping the incident light at a frequency Ω_I and by phase sensitive detection at frequency Ω_I. The normalization in this case was achieved by a numerical division of the $I_0\Delta R$ spectrum by I_0R. It was found that this procedure gave better accuracy when using PbS cell for small signal levels.

3.3 Sample details.

All the GaAlInAs/InP samples were provided by Dr.Gary Wicks of Cornell University. The samples were grown lattice matched to (100) InP using MBE. Details of the sample growth technique is given in Ref. 75. The MBE growth was carried out in a Varian 360 MBE system. The lattice matched conditions were deduced from photoluminecence (PL) at 4K and x ray diffractometer measurements. In practice, the In flux was maintained at nominally constant value and the Al and Ga fluxes were altered within the constraint $F_{Al} + F_{Ga} = 0.47(F_{Al} + F_{Ga} + F_{In})$. The InP substrates were chemically etched in $H_2SO_4:H_2O_2:H_2O$ and the native oxides were removed by heating in vacuum to 500 C in an As_4 flux. The growth temperature ranged between 530-570°C. The composition of the alloy system were determined from Rutherford backscattering measurements.

3.4 Experimental Results

As explained in the previous sections, the features observed in the EER spectra are due to critical points in the BZ. To establish the correspondence between the observed spectra and the critical points, the band structure of GaAs, (a prototype III-V semiconductor) along <100> and <111> are shown in Fig. 17. The principal optical transitions between the valence and the conduction bands in the energy range up to 10 eV are shown by vertical arrows. Displayed in Fig. 18 are the room temperature electrolyte electroreflectance spectra of GaAs. Three distinct groups of structures are present in the spectra. The first group ~ 1.5 eV is denoted by E_0 and $E_0+\Delta_0$. The structure denoted by E_0 corresponds to the fundamental gap and arises from transitions Γ_{8v} - Γ_{1c} at the zone center. The subsidiary structure denoted by $E_0+\Delta_0$ is the spin orbit split component, and arises from transitions between Γ_{7v} and Γ_{1c}.

Above the fundamental gap, there is a second group of structure (~ 3ev) denoted by E_1 and $E_1+\Delta_1$. These features are due to transitions along <111>, between the spin orbit split Λ_3 valence bands and the lowest lying Λ_1 conduction band. The other structures lying (~ 4.5 ev) are denoted by E_0' and $E_0'+\Delta_0'$, E_2 and $E_2+\delta$. E_0' arises from transitions at Γ point between the top of the valence band, and the second conduction band. Δ_0' is the spin orbit splitting of the second

FIG. 17. Bandstructure of GaAs along (100) and (111) directions.(Ref. 6)

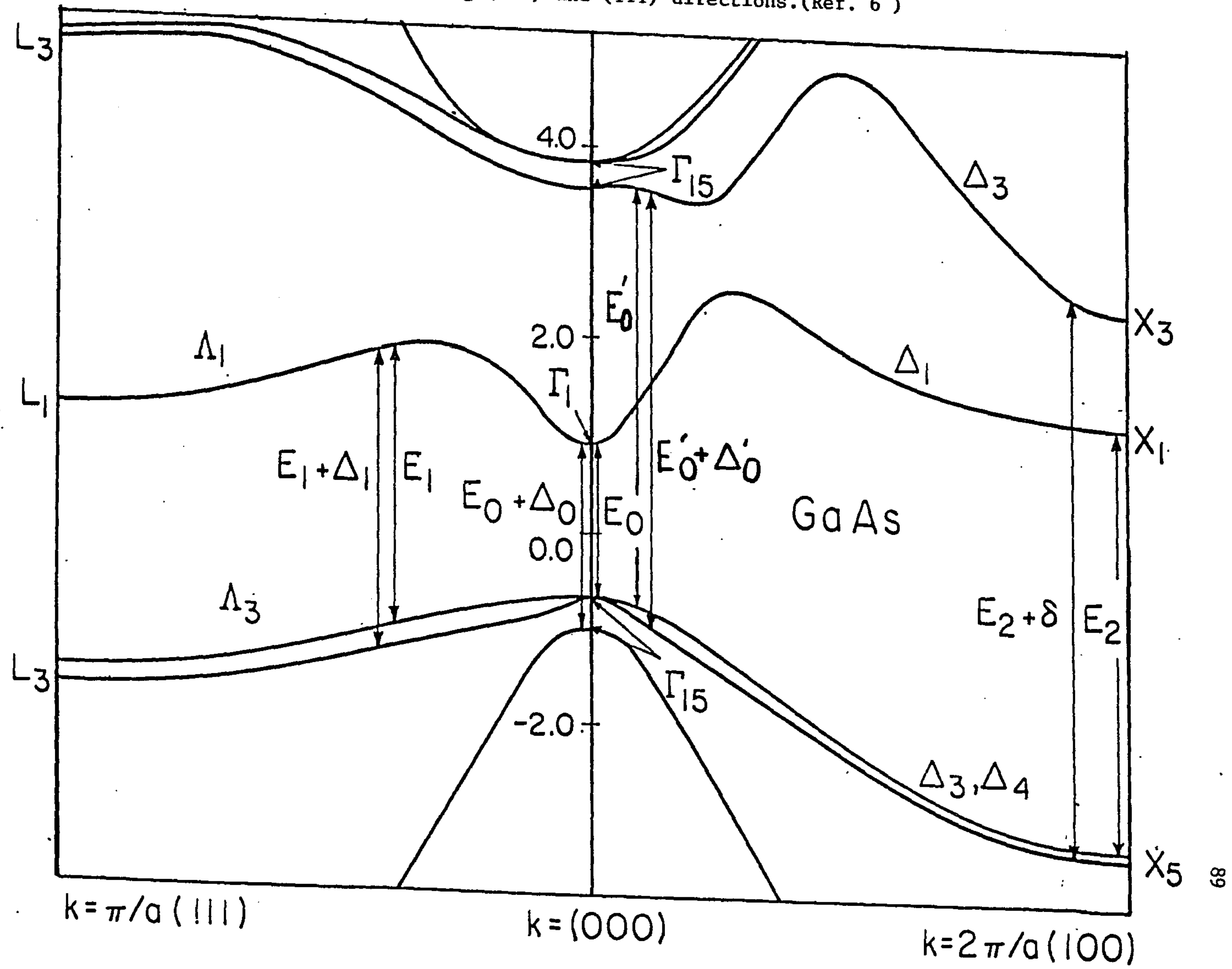

FIG. 18. Electroreflectance spectrum of n GaAs at 300 K.

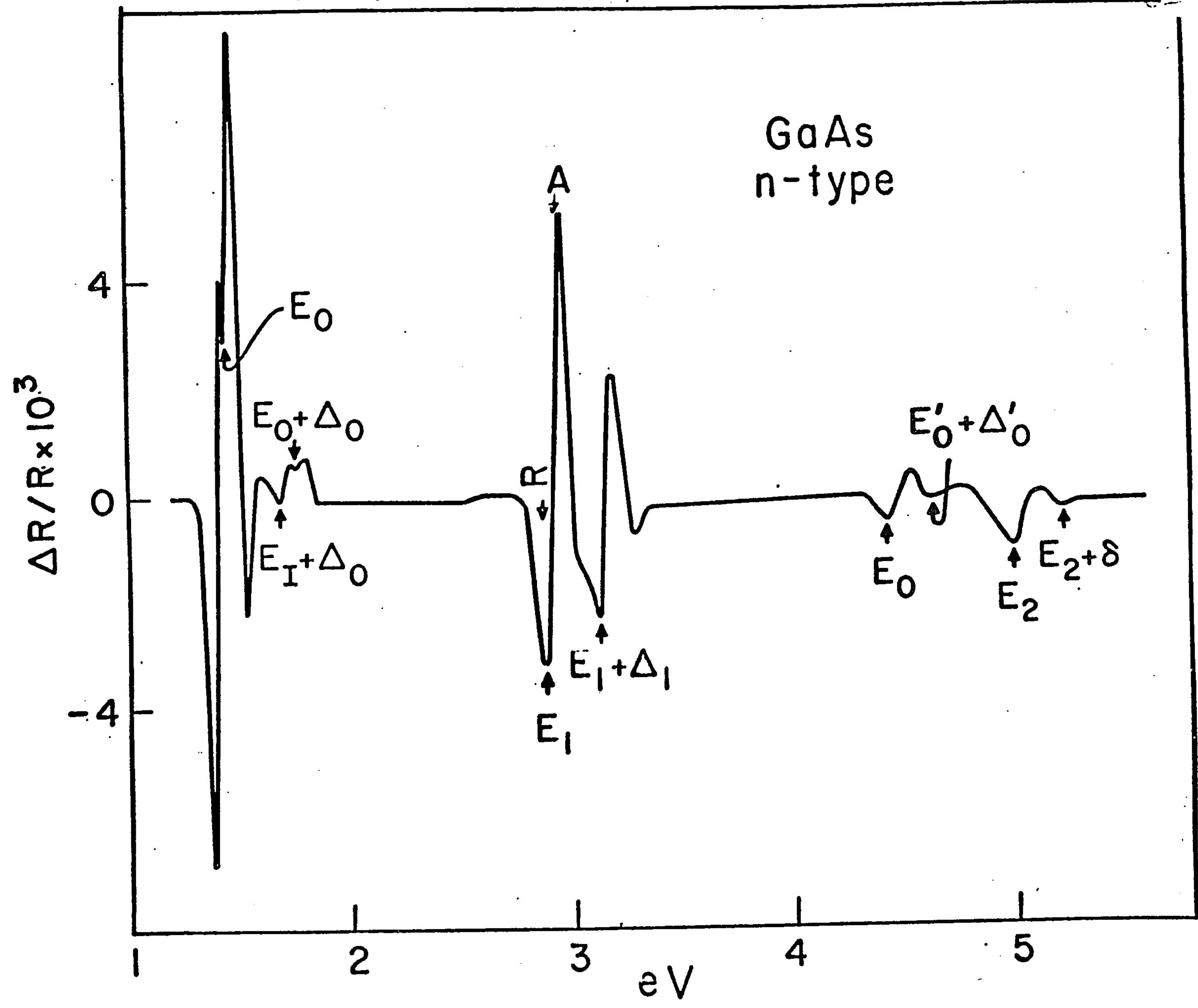

conduction band. The transitions X_5 - X_1 and X_5 - X_3 give rise to the features E_2 and $E_2 + \delta$ shown in the figure.

3.4.1 Electroreflectance: GaAlInAs/InP

The room temp EER spectra of the various samples, in general, were typical of the other ternary and quaternary alloys of zinc blende structure. The spectra from samples in the entire composition range $0 \le x \le 1$, exhibit three distinct groups of features in the energy range ≈ 0.5 eV to 6 eV. These spectral features correspond to E_0's, E_1's and E_0''s.

3.4.2 E_0 and $E_0 + \Delta_0$ transitions.

Displayed in Figs. 19 to 24, are the room temperature EER spectra of the various $(Ga_{1-x}Al_x)_{0.47}In_{0.53}As$ samples grown lattice matched to InP ($0.04 \le x \le 1$). All samples exhibit well resolved spectral features E_0 and $E_0 + \Delta_0$. The structures corresponding to both E_0 and $E_0 + \Delta_0$ move up in energy position as the Al fraction increases from 0 to 1.

No significant changes in the lineshapes were observed for small changes in the modulating voltage. This shows that the lineshapes are well described by the low field regime (refer section 3.1.1)

The various bandstructure parameters of this quaternary alloy system are determined by analyzing the different spectral features using Eqn. (75). The main focus were on the accurate determination of

FIG. 19. Electroreflectance spectrum of $(Ga_{1-x}Al_x)_{0.47}In_{0.53}As/InP$ at 300 K for x=0.04

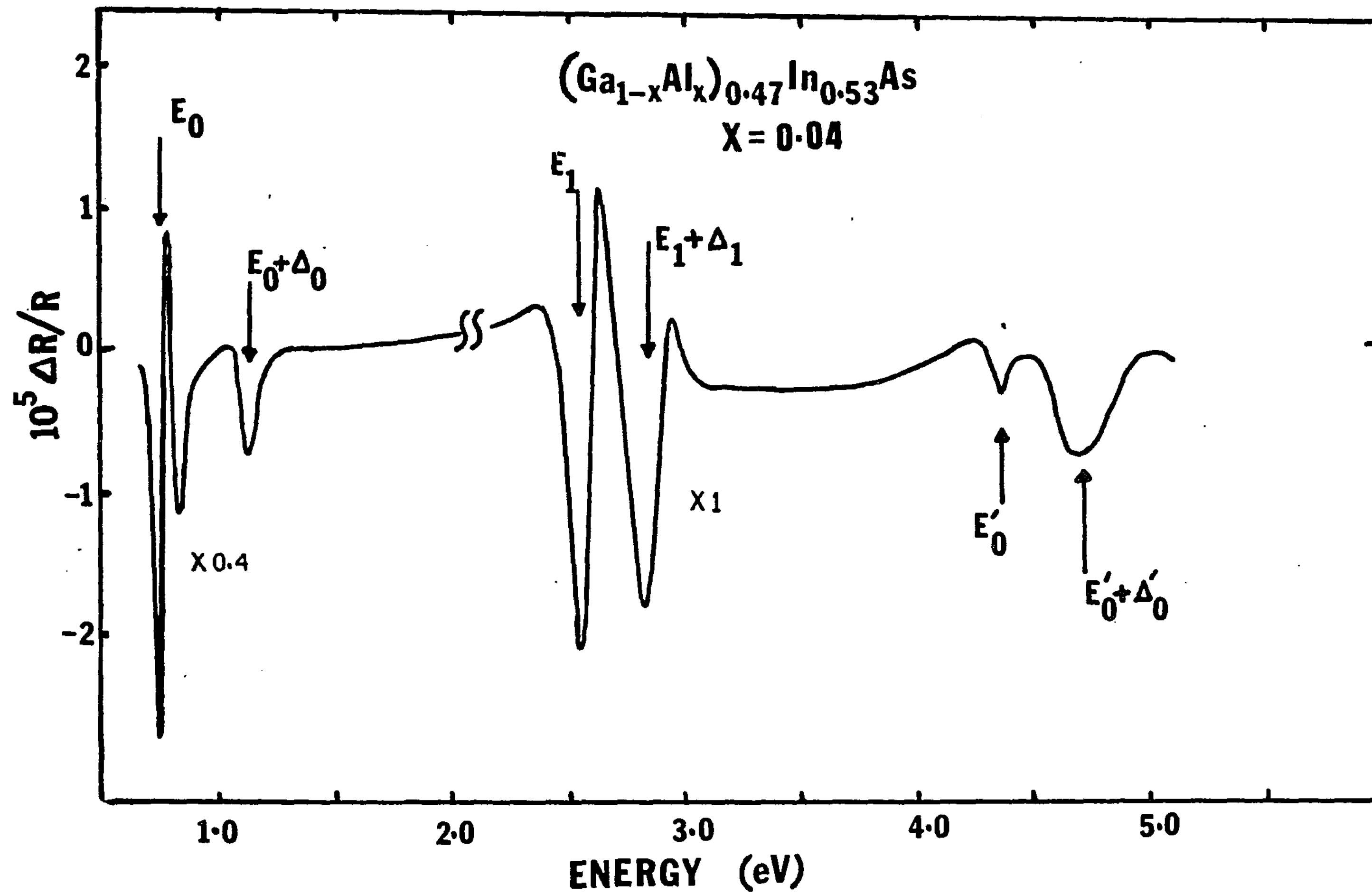

FIG. 20. Electroreflectance spectrum of $(Ga_{1-x}Al_x)_{0.47}In_{0.53}As/InP$ at 300 K for x=0.2

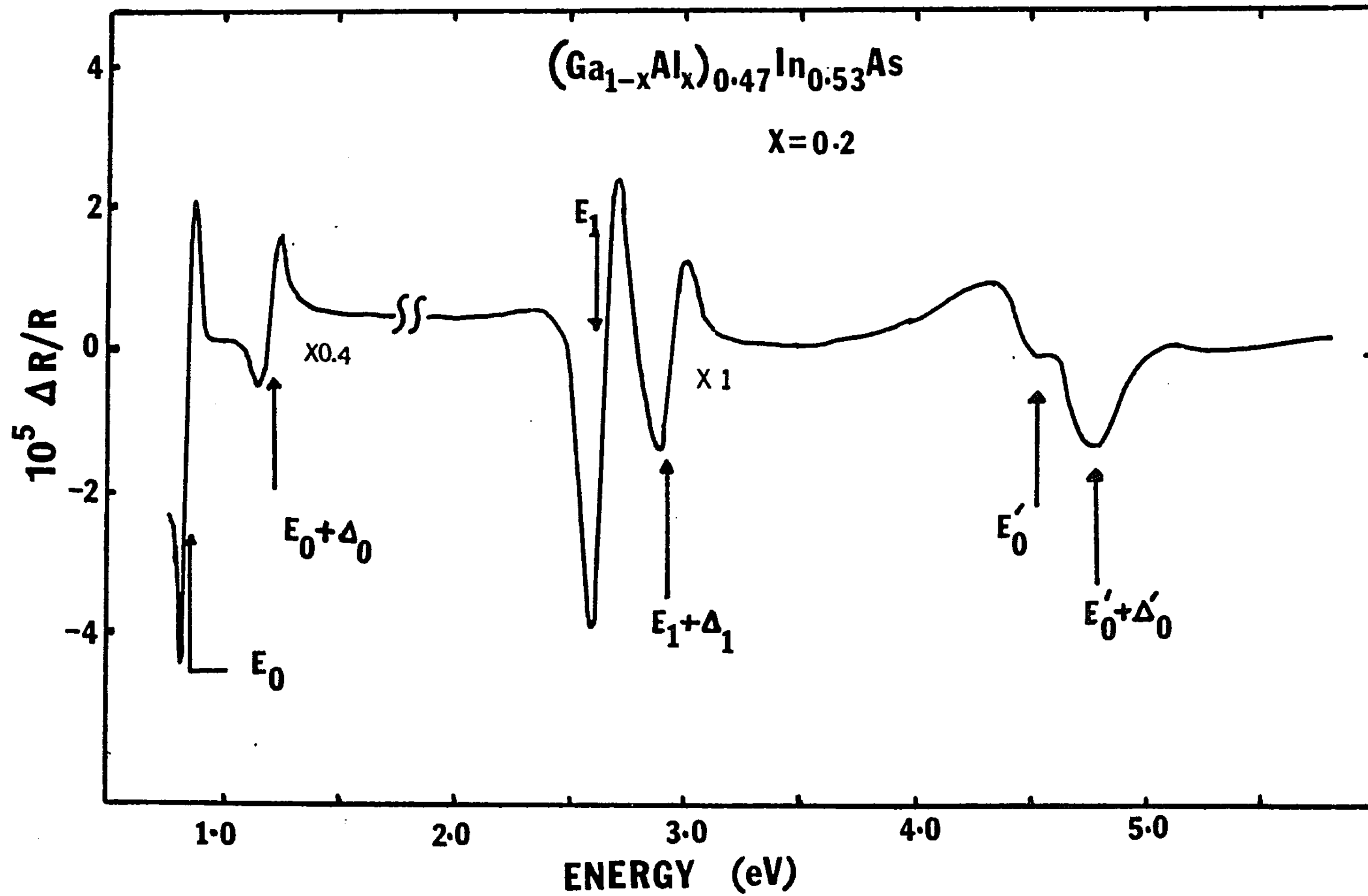

FIG. 21. Electroreflectance spectrum of $(Ga_{1-x}Al_x)_{0.47}In_{0.53}As/InP$ at 300 K for x=0.4

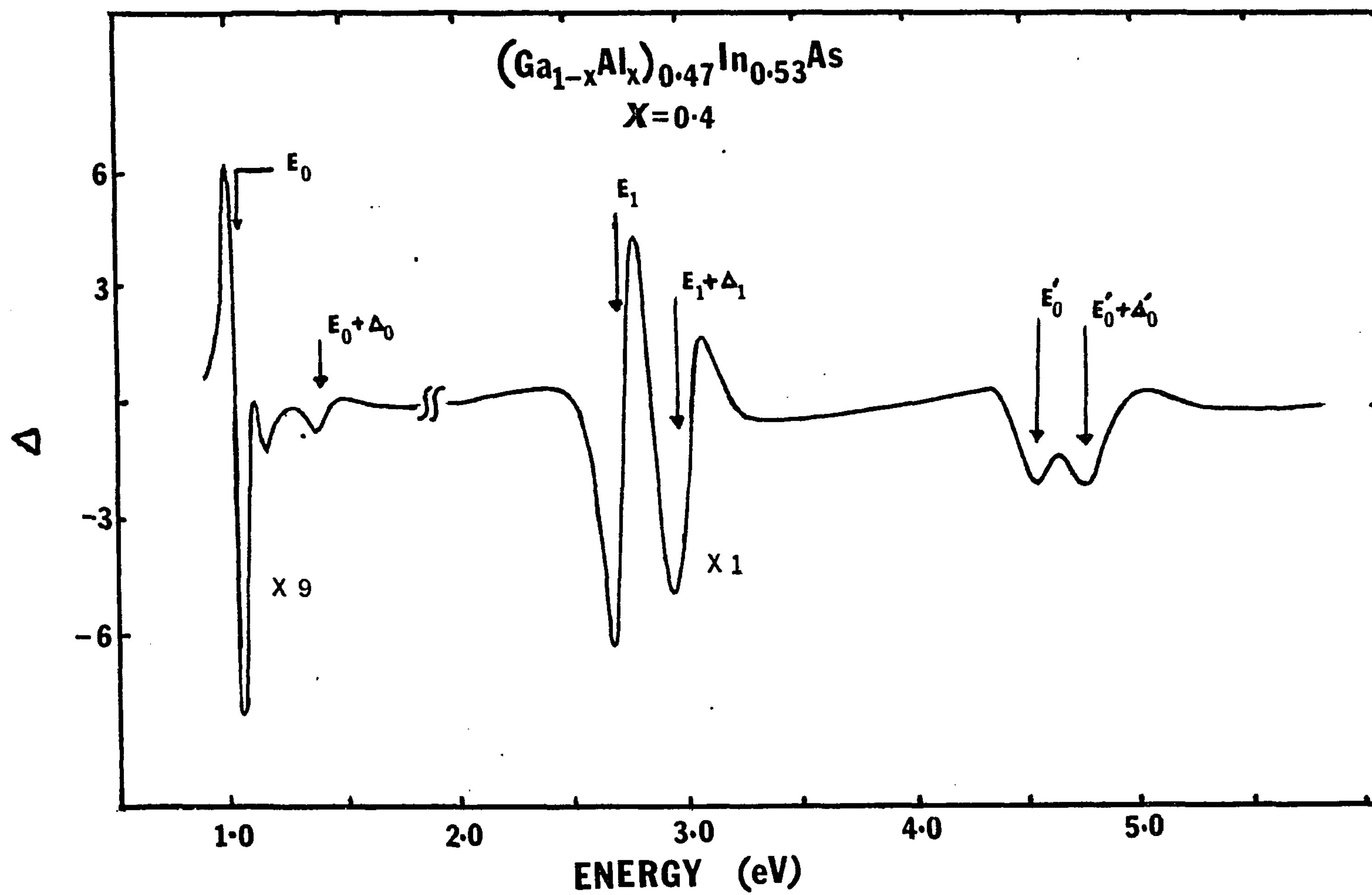

FIG. 22. Electroreflectance spectrum of $(Ga_{1-x}Al_x)_{0.47}In_{0.53}As/InP$ at 300 K for x=0.6

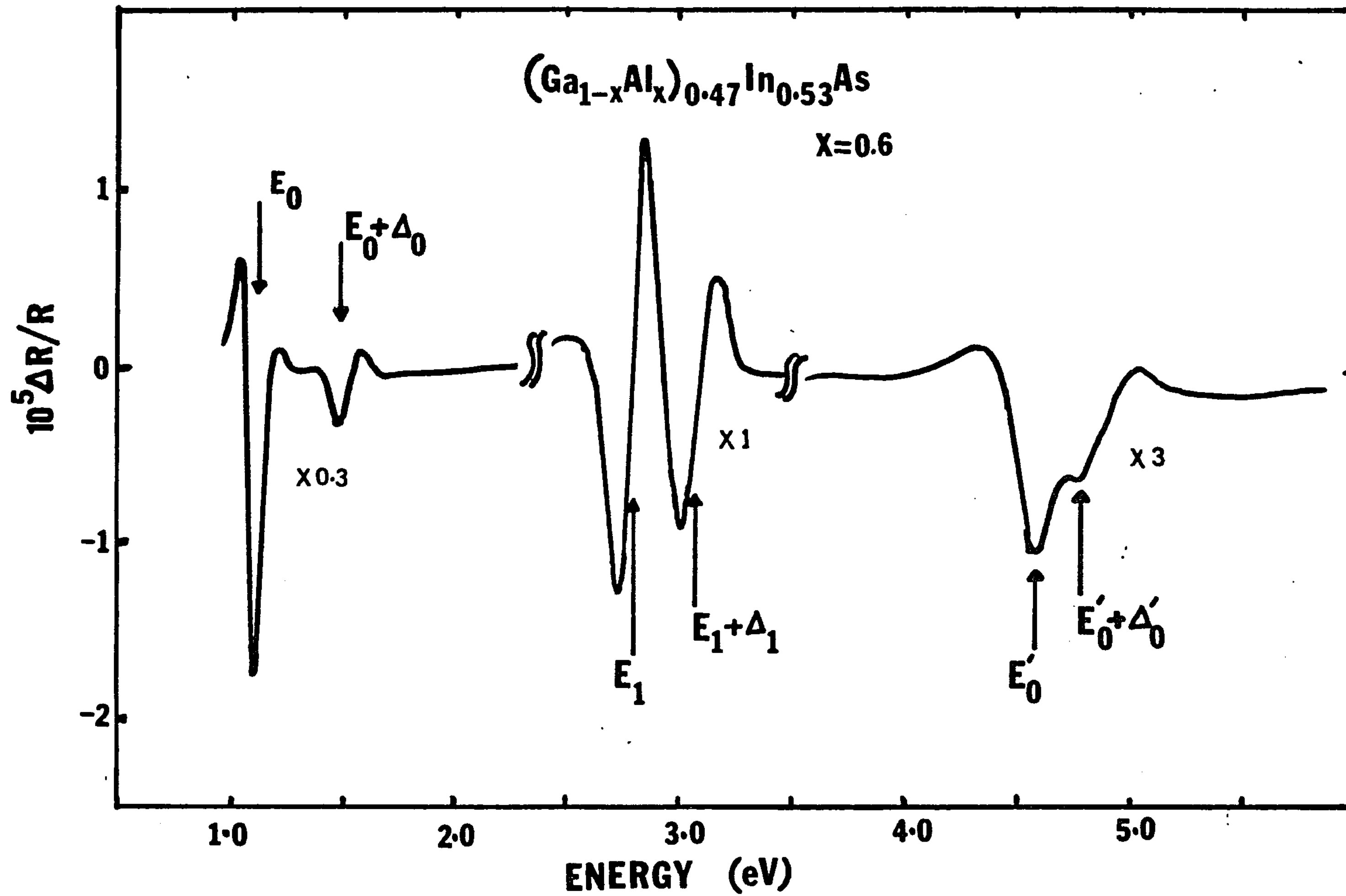

FIG. 23. Electroreflectance spectrum of $(Ga_{1-x}Al_x)_{0.47}In_{0.53}As/InP$ at 300 K for x=0.8

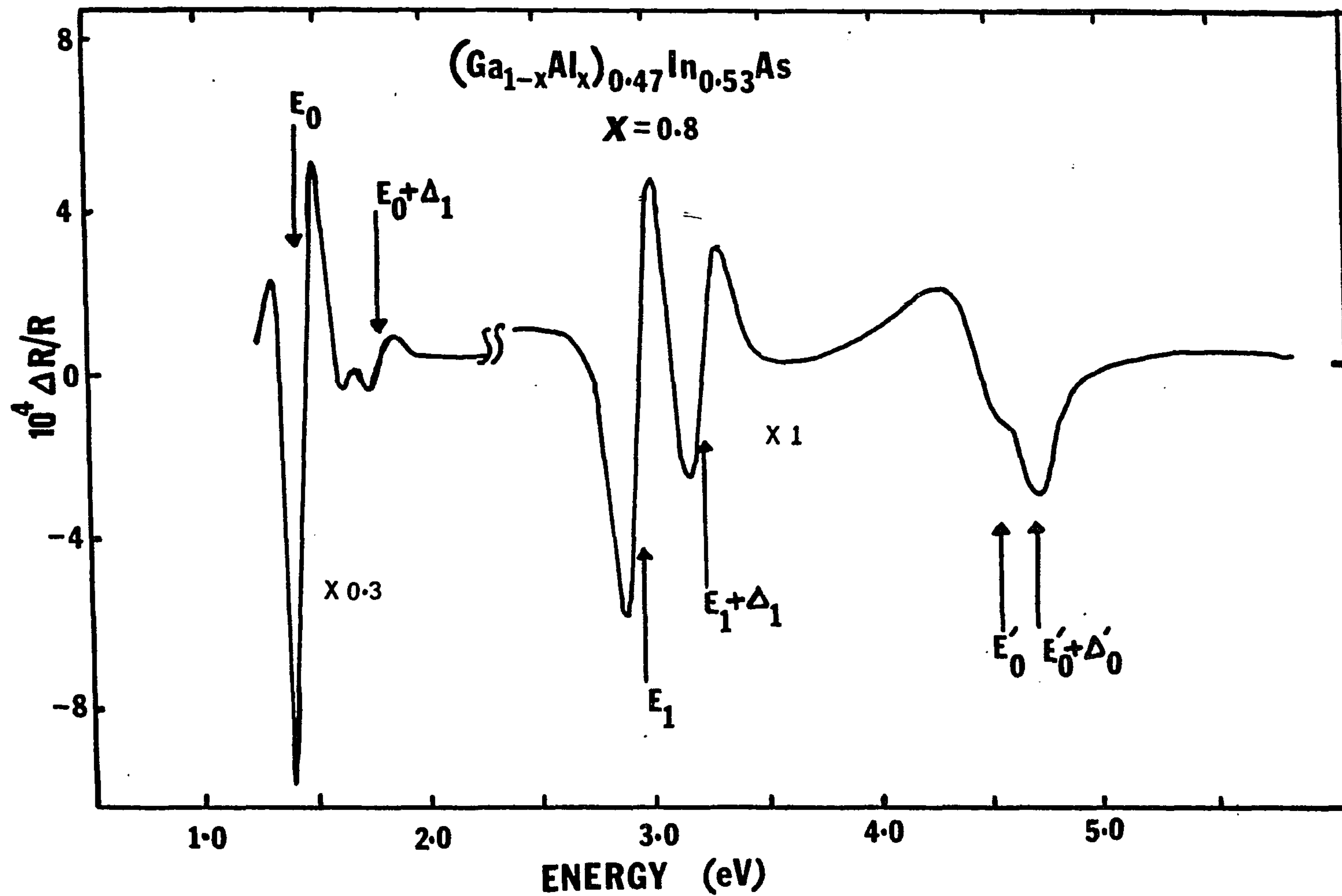

FIG. 24. Electroreflectance spectrum of $(Ga_{1-x}Al_x)_{0.47}In_{0.53}As/InP$ at 300 K for x=1.0

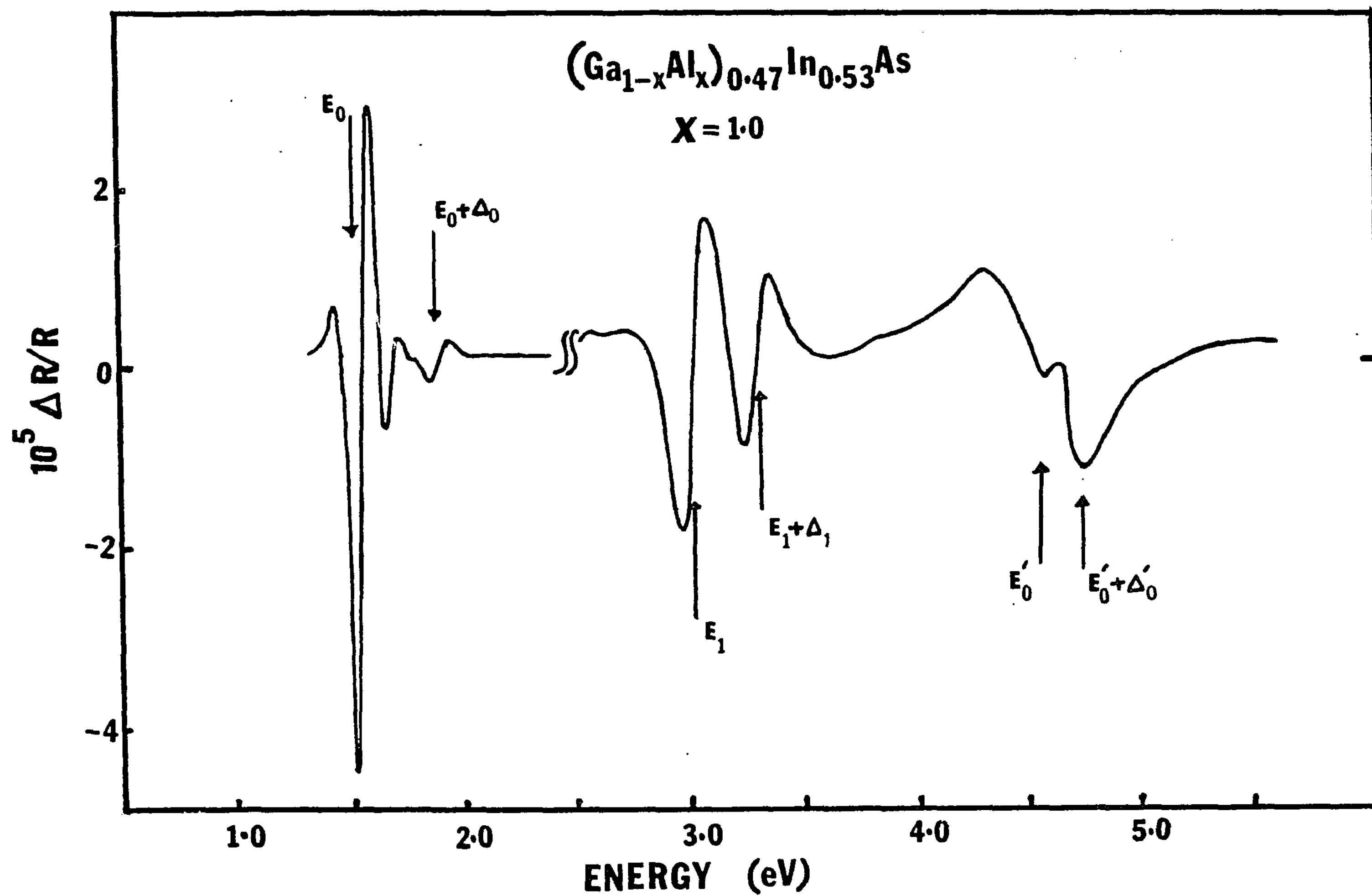

the transition energies and the broadening parameters in the composition range 0<x<1. An accurate phase analysis can be done only if one knows the complex prefactors in Eqn. 75 which depends on the bulk optical constants and the possible field inhomogenites in the material. A least square fit was performed using Eqn. 75 for E_0 and $E_0+\Delta_0$ features to determine the critical point energies and the broadening parameters. These structures are three dimensional critical points and hence n=2.5 in Eqn. 75. The transition energy E_g, broadening parameter Γ, the amplitude C, and the phase factor θ were taken as adjustable parameters and they were varied to obtain the best fit to experimental structure. Fig. 25 shows a typical fit using Eqn. 75 for the E_0 feature of sample with x=0.4. The solid line represents the experimental data and the dotted line is the fit obtained with parameters as shown at the top right hand corner of the Fig. 25.

Presented in Table III are the E_0 and $E_0+\Delta_0$ critical point energies as well as the broadening parameters obtained for the various compositions, x, of the quaternary $(Ga_{1-x}Al_x)_{0.47}In_{0.53}As$. Also tabulated are the spin orbit splittings Δ_0 at various compositions.

3.4.3 E_1 and $E_1+\Delta_1$ transitions

The group of features seen between 2.2 eV to 3.5 eV in figures 19 to 24 correspond to the E_1 and $E_1+\Delta_1$ transitions. Since the E_1 and $E_1+\Delta_1$ features overlap, it was necessary to perform a least squares fit

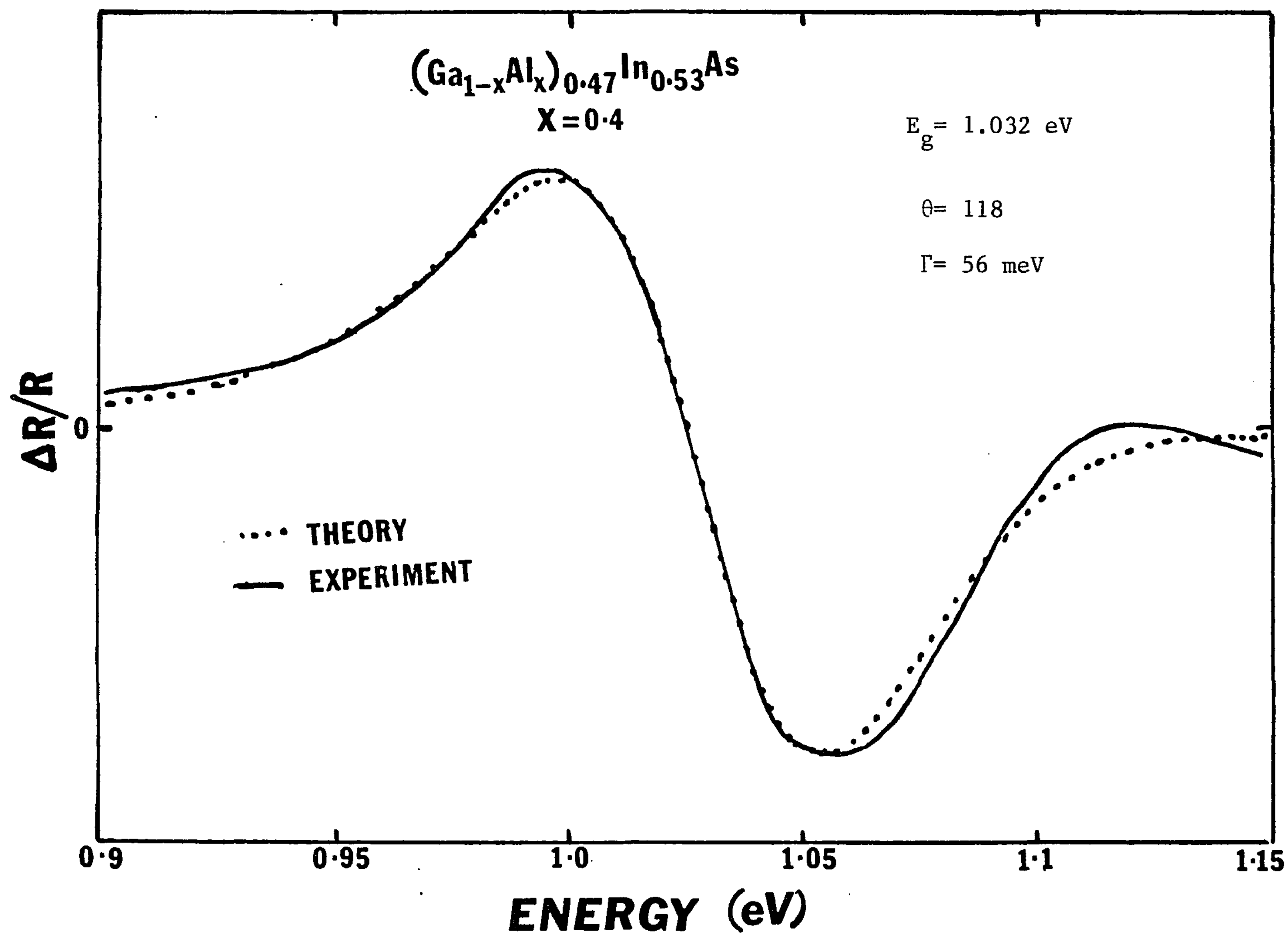

FIG. 25. A typical lineshape fit for the E_0 feature using eqn. 75.

Table IV. The transition energies and broadening parameters for the various $(Ga_{1-x}Al_x)_{0.47}In_{0.53}As/InP$ samples measured at room temp.

composition x	E_o (eV)	$\Gamma(E_o)$ (meV)	$E_o+\Delta_o$ (eV)	$\Gamma(E_o+\Delta_o)$ (meV)	E_1 (V)	$\Gamma(E_1)$ (meV)	$E_1+\Delta_1$ (meV)	$\Gamma(E_1+\Delta_1)$ (meV)	E_o' (eV)	$E_o+\Delta_o'$) (eV)
1.0	1.534	61	1.891	74	3.012	151	3.291	157	4.592	4.768
0.8	1.394	84	1.798	101	2.93	170	3.213	190	4.575	4.732
0.6	1.101	65	1.469	98	2.78	133	3.077	167	4.595	4.783
0.4	1.032	56	1.410	73	2.713	136	2.994	180	4.572	4.776
0.2	0.824	66	1.233	92	2.626	133	2.906	176	4.502	4.783
0.04	0.752	42	1.120	45	2.558	119	2.843	196	4.365	4.723
0	0.744	23	1.101	24	-	-	-	-	-	-

considering the contributions from critical points of two pairs of bands $\Lambda_3 - \Lambda_1$. Hence the lineshape expression becomes:

$$\Delta R/R = C_1 e^{i\theta_1}(E-E_{g_1}+i\Gamma_1)^{-n} + C_2 e^{i\theta_2}(E-E_{g_2}+ i\Gamma_2)^{-n} \tag{80}$$

The structures were fit using the above equation constraining the phase factor to be equal (i.e., $\theta=\theta_1=\theta_2$). The upper spin orbit split valence bands and the lower conduction bands are nearly parallel along the <111> direction in zinc blende semiconductors. If the bands are strictly parallel along the <111>, E_1 and $E_1+\Delta_1$ would be two dimensional (2D M_0) critical points. However the conduction band actually curves downward slightly relative to the valence bands. Thus an alternate description is 3D M_1 critical points. We have analysed the data considering E_1 and $E_1+\Delta_1$ as 3D critical points (i,e., n=2.5), and also as a 2D critical point. Though the fit obtained in both cases were quite good, the mean square deviation of the fitted curve was found to be larger for 3D than for 2D. Similar results have been reported for the quaternary system GaInAsP grown lattice matched to InP[76]. A typical fit using Eqn. 80 for E_1 and $E_1+\Delta_1$ structures are shown in Fig. 26. The solid line represents the experimental data and the dotted line is the lineshape given by Eqn. 80 with the parameters as shown at the bottom

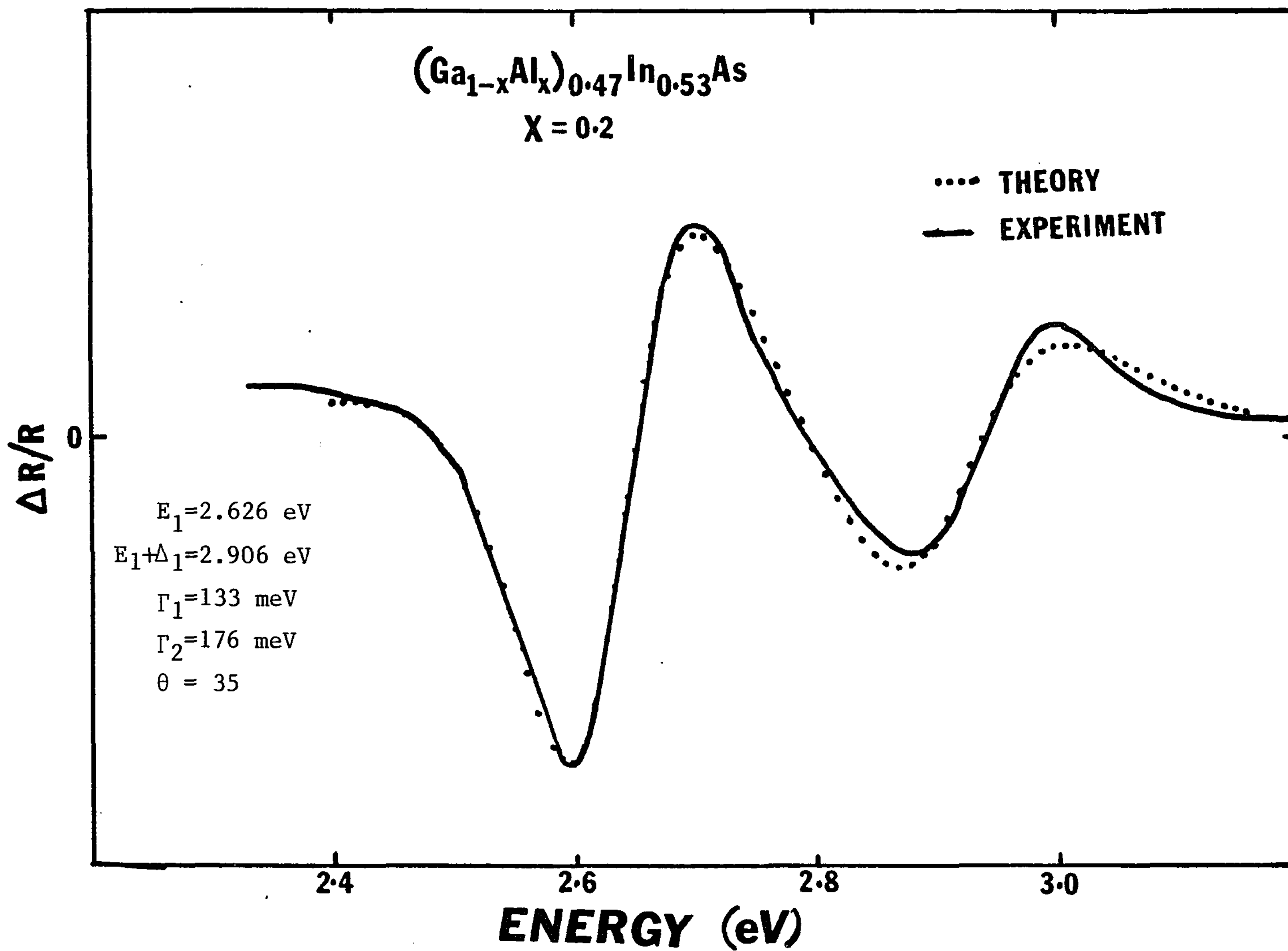

FIG. 25. A typical lineshape fit for E_1 and $E_1+\Delta_1$ features using eqn.80 .

left hand corner of Fig. 26. The transition energies, the spin orbit splittings energies and broadening associated with the E_1 critical point is also tabulated in Table III.

3.4.4 E_0' and $E_0'+\Delta_0'$ transitions.

The structures corresponding to the critical points E_0' and $E_0'+\Delta_0'$ are also seen in figures 19 to 24. The energy positions of the E_0' and $E_0'+\Delta_0'$ features are taken as the corresponding peak position as there is only one well defined peak for each structure.

3.4.5 Composition dependence of transition energies

The composition dependence of the E_0 and $E_0+\Delta_0$ are shown in Fig. 27. The variation of the spin orbit splitting parameter Δ_0 is plotted at the bottom of Fig. 27. Displayed in Fig 28 are the composition dependence of the E_1, $E_1+\Delta_1$, E_0', and $E_0'+\Delta_0'$ optical features. The solid lines in Figs. 27 and 28 represent a least square quadratic fit of the energy, to the measured transition energies i.e., $E=\underline{a}+\underline{b}x+\underline{c}x^2$. The values of the quadratic fitting parameters $\underline{a}$,$\underline{b}$ and $\underline{c}$ for the E_0, $E_0+\Delta_0$, E_1, $E_1+\Delta_1$, E_0' and $E_0'+\Delta_0'$ features as well as the spin orbit splittings Δ_0 and Δ_1, are listed in Table IV. Also listed in this table are the values of $\underline{a}$, $\underline{b}$ and $\underline{c}$ for E_0 obtained from a recent room temperature photoluminescence measurement[11] as well as a recent theoretical calculation[12] (dotted line in Fig. 27).

The behaviour of the x=0 end point sample was interesting. The spectrum of this sample is presented in Fig. 29. This material exhibits very sharp E_0 and $E_0+\Delta_0$ features in relation to other samples, where as, this shows very poor signals for the higher lying transitions, for example, E_0' and $E_0'+\Delta_0'$ are not resolved. This unusual behavior is probably related to the growth conditions as previous investigators have reported good EER lineshapes for the LPE grown GaInAs. Also the lineshapes obtained by third drivative of the dielectric function measured by scanning ellipsometry for $Ga_{0.47}In_{53}As/InP$ were quite similar to other III-V alloys[76]

In general our results are in good agreement with other measurements where such a comparison can be made. For example our values of the E_0 as a function of x are in very good agreement with the room temperature photoluminescent work of Olego et. al[11]. The results for the end point (or near end point) materials $Ga_{0.53}In_{0.47}As$[76-80] or $\{((Ga_{0.96}Al_{0.04})_{0.47})In_{0.53}As\}$, $Al_{0.53}In_{0.47}As$[81] are consistant with other published results. Note also that the theory of Aymerich[12] has accounted quite well for the composition dependence of the bandgap E_0

As mentioned earlier the $Ga_{0.53}In_{0.47}As$ samples exhibit the narrowest lineshapes for E_0 and $E_0+\Delta_0$. Even at small Al concentrations (x=0.04), the broadening parameter is higher by approximately a factor of two. For Al composition $0.2 \leq x \leq 1.0$, even though there are some

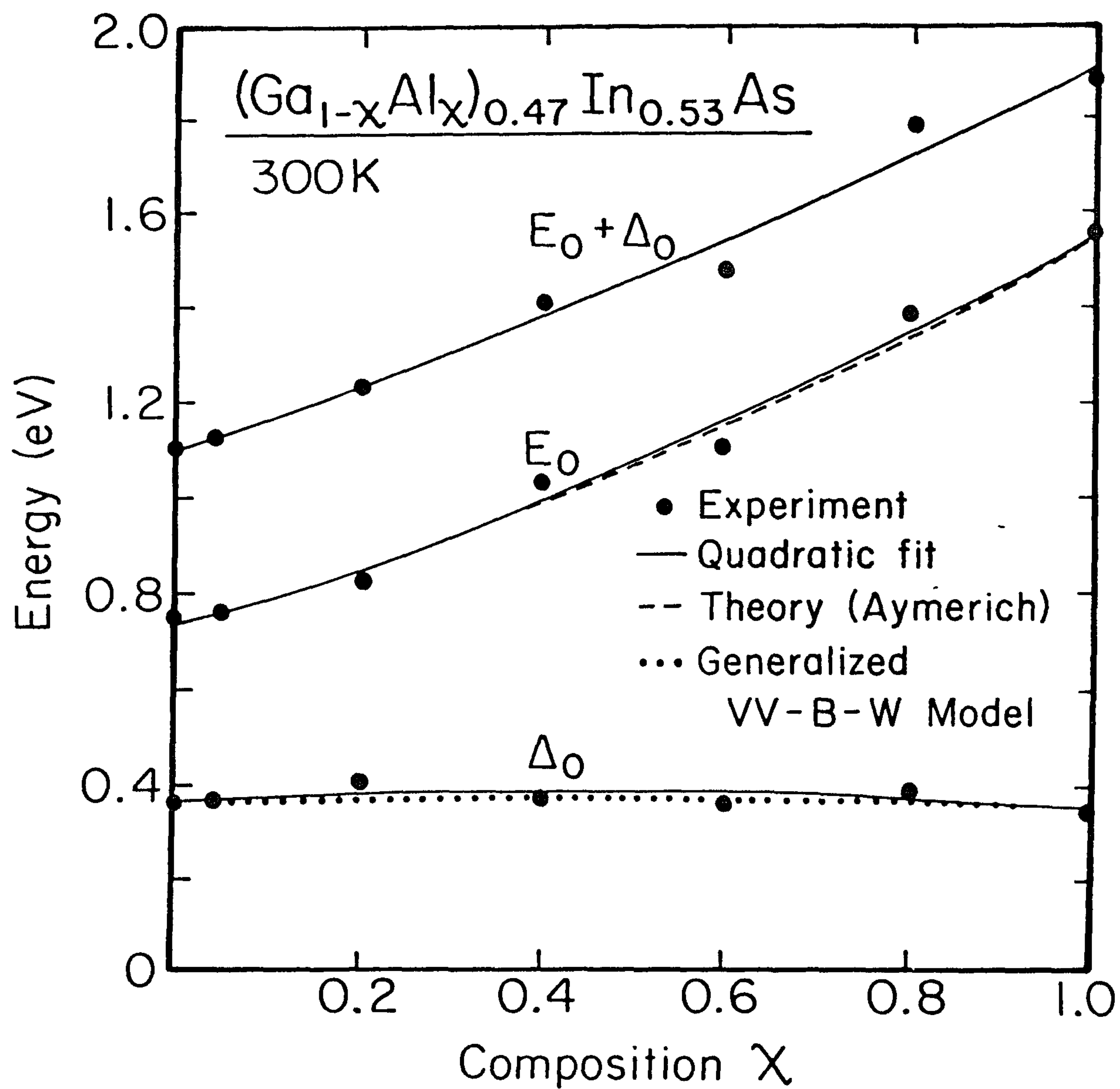

FIG. 27. Variation of the E_0, $E_0+\Delta_0$, and Δ_0 energies as a function of composition x. The dashed line the theory of Aymerich (Ref. 12).

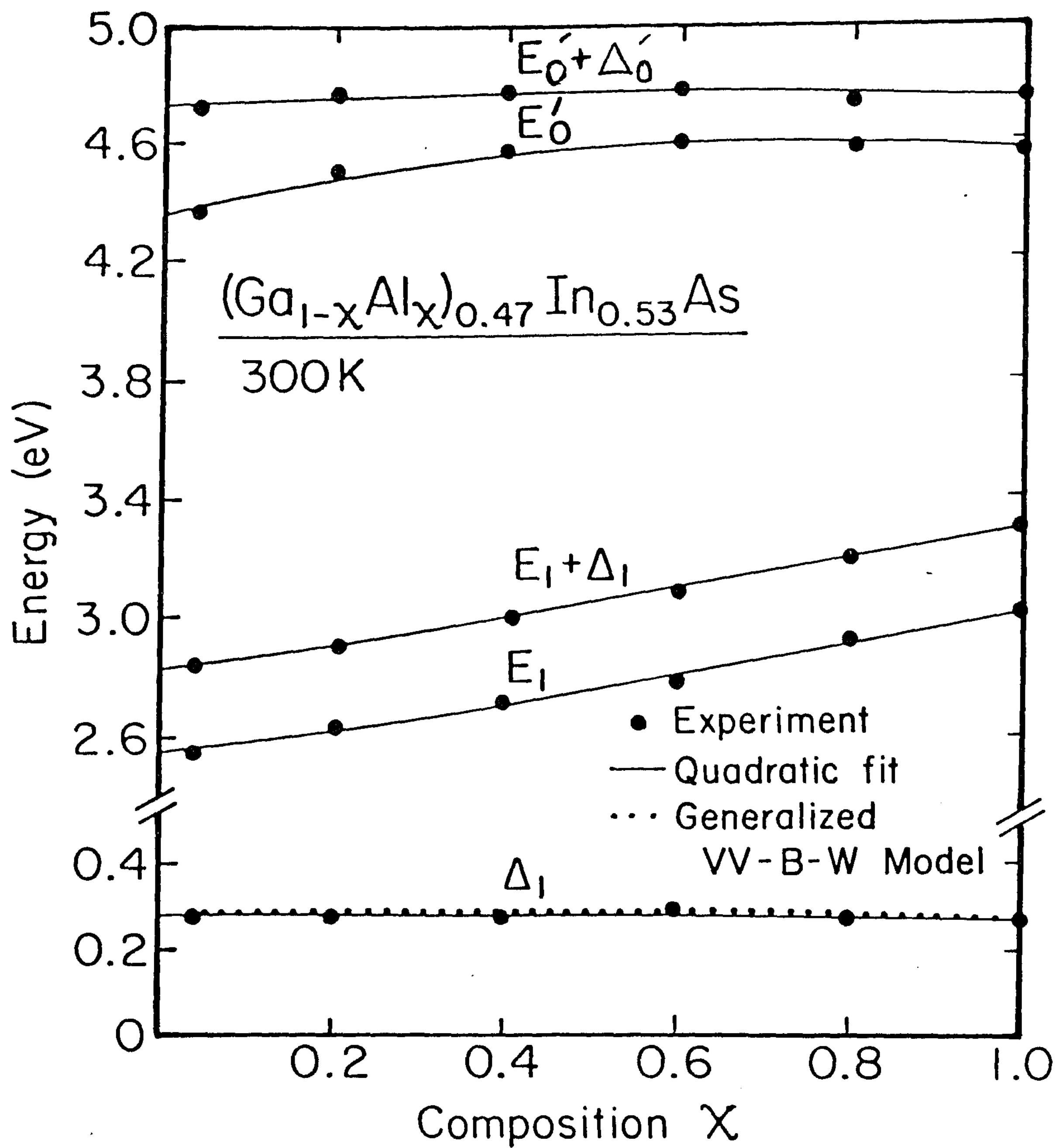

FIG. 28. Variation of E_1, $E_1+\Delta_1$, E_0', and $E_0'+\Delta_0'$ energies as a function of composition x.

Table IV. Values of the quadratic fitting parameters a, b and c obtained by fitting the various E versus x curves to equation $E = a + bx + cx^2$

Transition	a	b	c
E_0	0.73±0.03[a]	0.54±0.04[a]	0.28±0.04[a]
	0.76±0.04[b]	0.52±0.05[b]	0.25±0.03[b]
	0.73[c],[d]	0.51[c]	0.26[c]
$E_0+\Delta_0$	1.10±0.03[a]	0.64±0.04[a]	0.18±0.04[a]
E_1	2.55±0.03[a]	0.36±0.04[a]	0.11±0.04[a]
$E_1+\Delta_1$	2.83±0.03[a]	0.39±0.04[a]	0.08±0.04[a]
E_0'	4.36±0.04[a]	0.69±0.05[a]	-0.48±0.05[a]
$E_0'+\Delta_0'$	4.74±0.04[a]	0.15±0.05[a]	-0.13±0.04[a]
Δ_0	0.37±0.02[a]	0.10±0.02[a]	-0.10±0.03[a]
Δ_1	0.28±0.02[a]	0.03±0.02[a]	-0.03±0.03[a]

(a) This work

(b) Ref. 11

(c) Ref. 12

(d) In order to adjust for the temperature difference between Ref. 12 (low temperatures) and our work (300 K) this value of a has been fixed at the experimental number.

FIG.29. Electroreflectance spectrum of $(Ga_{1-x}Al_x)_{0.47}In_{0.53}As/InP$ at 300 K for x=0.0

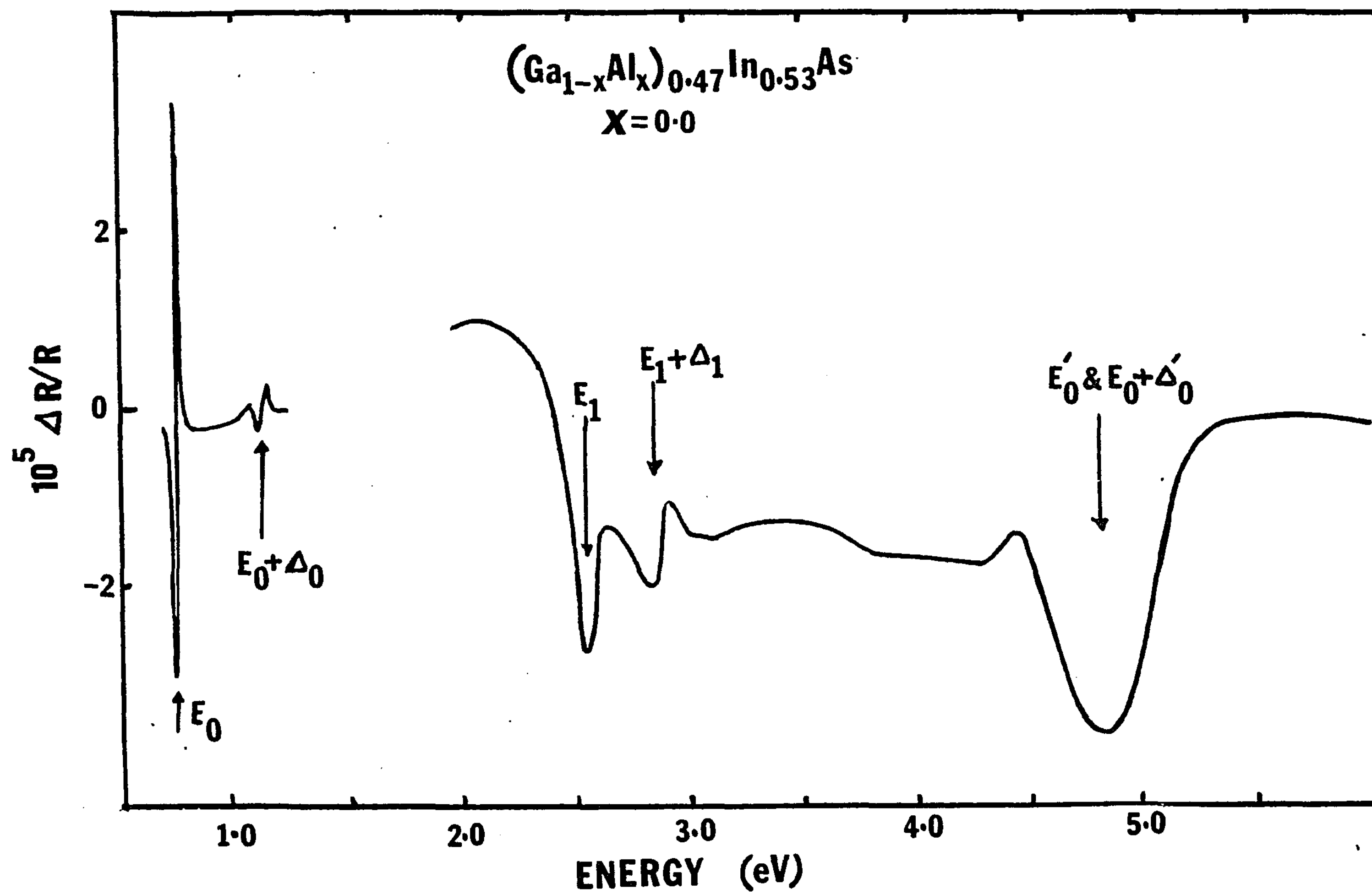

variations, the broadening remain approximately the same. In all cases $E_0+\Delta_0$ has a larger broadening than E_0. The behavior of E_1 and $E_1+\Delta_1$ are also of similar nature except for the fact that $Ga_{0.53}In_{0.47}As$ exhibits poor lineshapes for E_1 and $E_1+\Delta_1$

The changes in broadening parameter Γ are believed to be due to potential fluctuations resulting from the random atomic placement of the alloys. In general there are contributions from both the cation and the anion sublattices. In $(Ga_{1-x}Al_x)_{0.47}In_{0.53}As$ there is only variation in the distribution of the cation Ga and Al. Our results indicate that the changes in the contribution to Γ from the Ga sublattice as the composition varies is balanced by that from the Al sublattice. A similar study in the quaternary alloy system InGaAsP, where there are contributions from anion sublattice and cation sublattice, it has been shown that the primary origin for the variations in $\Gamma(E_1)$ is the anion disorder[76]. The unusual decrease in the broadening $\Gamma(E_0)$ and $\Gamma(E_0+\Delta_0)$ for the x=0 sample is not clearly understood at present.

3.5 Electroreflectance: GaAlAs/GaAs

The room temperature electrolyte electroreflectance spectra from the three samples SCL-392, SCL-400 and SCL-379 are shown in figures 30,31, and 32, respectively. The spectra of all the samples are similar to that reported earlier. The various features $E_0, E_0+\Delta_0, E_1, E_1+\Delta_1$, $E_0', E_0'+\Delta_0', E_2, E_2+\delta$ are shown by arrows.

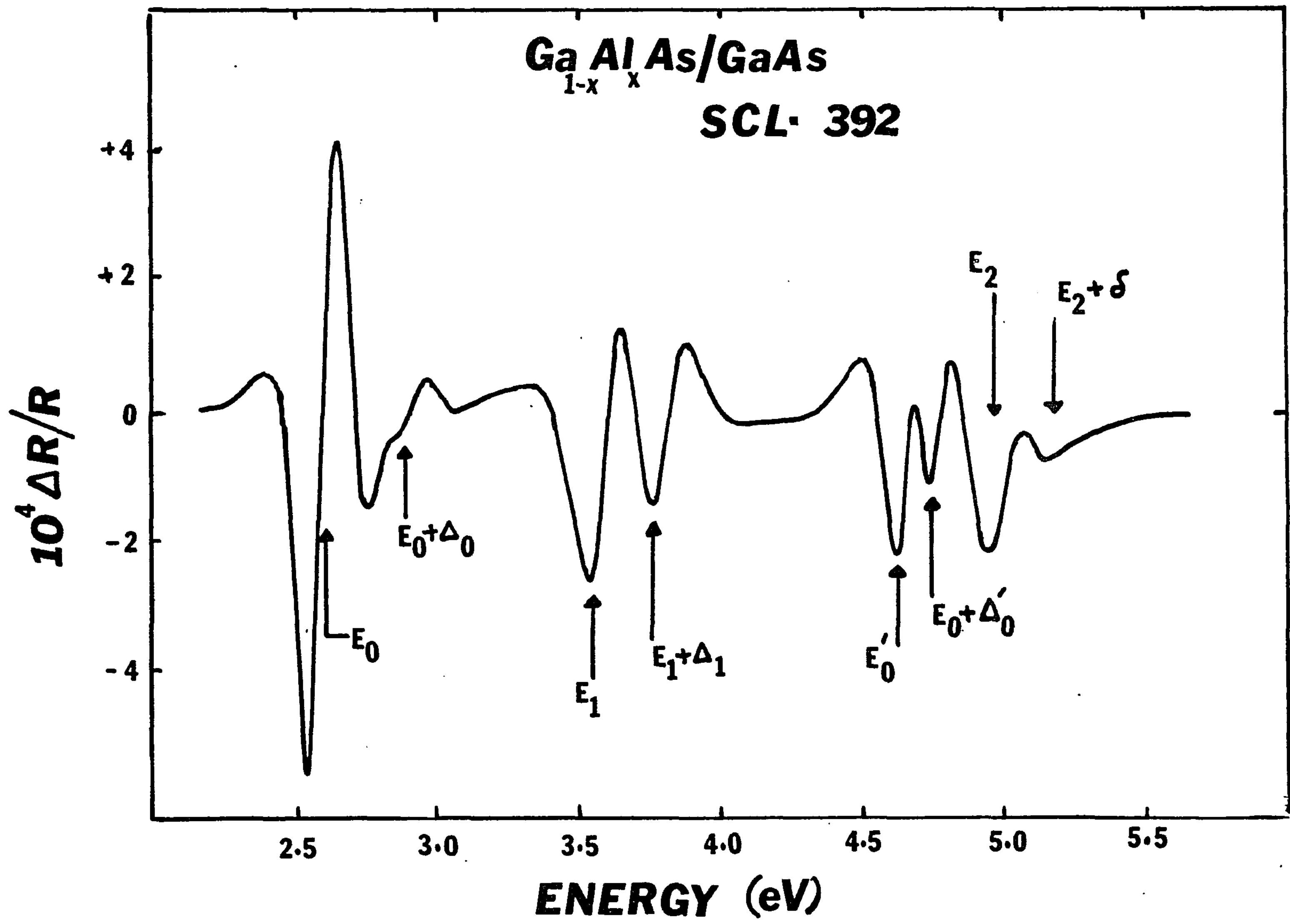

FIG. 30 . Electroreflectance spectrum of $Ga_{1-x}Al_xAs/GaAs$ sample SCL-392.

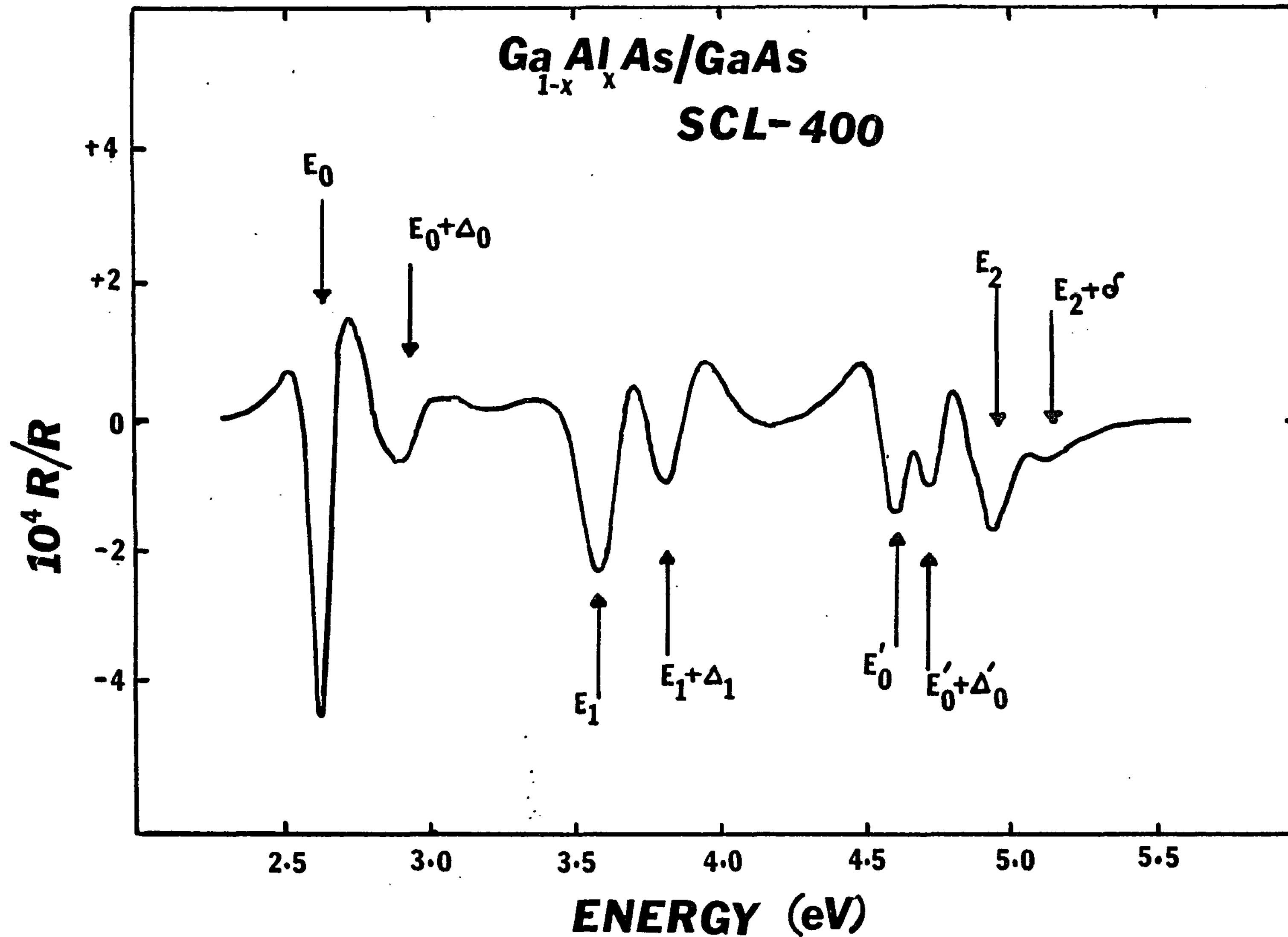

FIG. 31 . Electroreflectance spectrum of $Ga_{1-x}Al_xAs/GaAs$ sample SCL-400

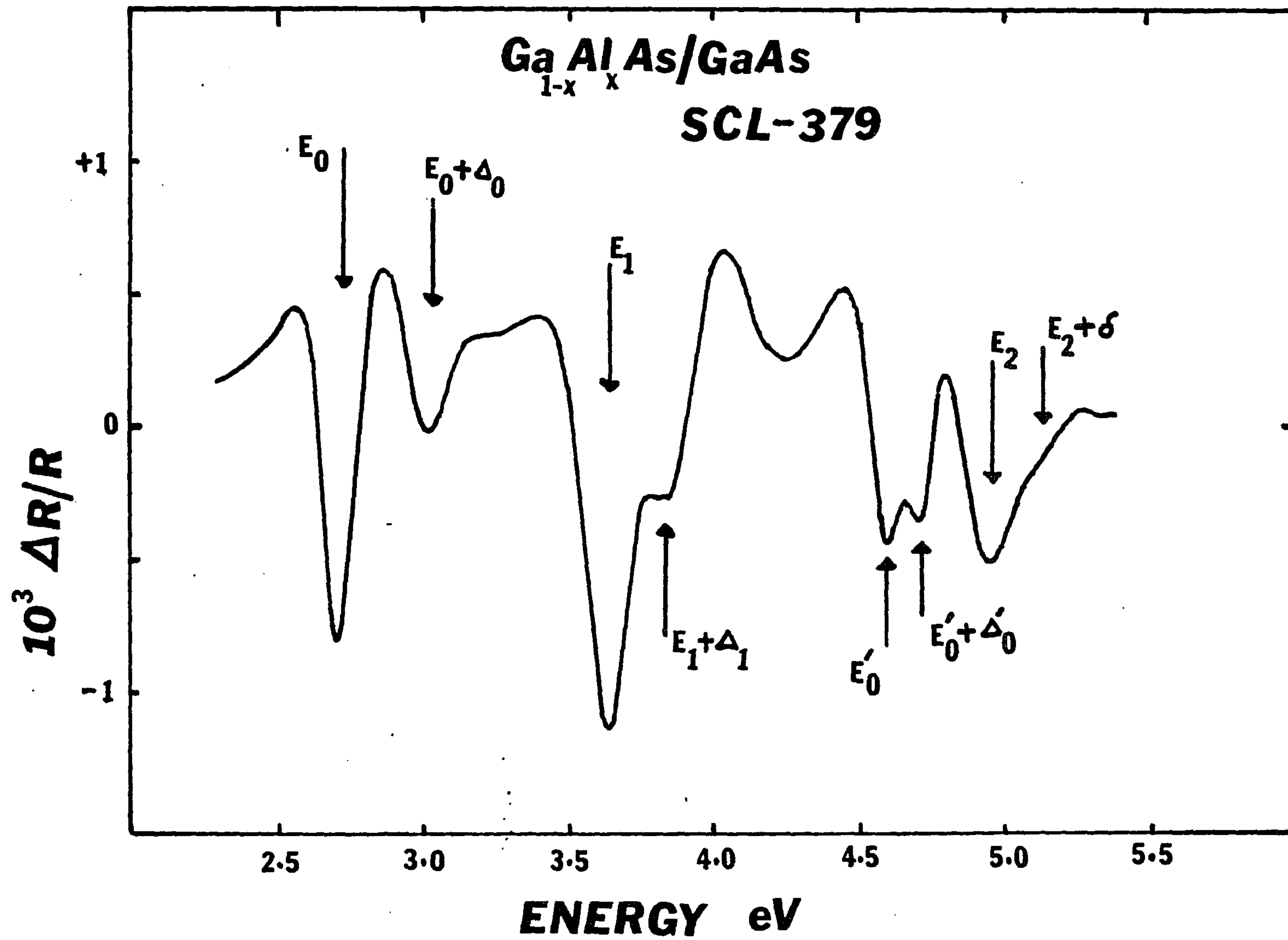

FIG. 32. Electroreflectance spectrum of $Ga_{1-x}Al_xAs/GaAs$ sample SCL-379.

The compositional variation of the fundamental gap E_0 and higher gaps have been measured by Berolo and Wooley[82]. The energy position of the E_0 peak indicates that, there is some variation in composition in the three samples as determined by this technique. The E_0 feature in SCL 400 occurs at 2.641 eV indicating that x=0.81±0.01 for this material, whereas the energy position of the sample SCL-392 indicates a composition x=0.80±0.01 and that of SCL-379 gives x=0.84±0.01. These values are more accurate than that determined from the Raman scattering measurements (see Chapter II) but both agree within experimental error.

The E_1 and $E_1+\Delta_1$ features for these samples lie in the energy range 3.4 to 4 eV. Samples SCL-392 and SCL-400 exhibit well resolved structures for the E_1 and $E_1+\Delta_1$ whereas in SCL-379 E_1 and $E_1+\Delta_1$ merge together and $E_1+\Delta_1$ is seen only as a shoulder.

Other features E_0', $E_0'+\Delta_0'$, E_2 and $E_2+\delta$ are present in all the samples in the energy range 4.4 to 5.5 eV. In samples SCL-400 and SCL-392 these features are better resolved. $E_2+\delta$ is seen only as a weak shoulder in SCL-379.

The quality of the various epilayers as seen by the electronic properties is clear from the EER spectra. Sample SCL-379 which has poor quality substrate, exhibit much broader lineshapes for the various interband transitions. In addition these features are less resolved in this sample.

3.6 Composition dependence of the spin orbit splittings.

It has been observed experimentally in semiconductor alloys, that the energies of various interband transitions and spin-orbit splitting parameters vary quadratically with alloy composition,[6,7,83] i.e.,

$$E(x) = \underline{a} + \underline{b}x + \underline{c}x^2 \quad (81)$$

or

$$E(x) = \underline{a} + \underline{b}'x + \underline{c}x(x-1) \quad (82)$$

where $\underline{a}$ and $\underline{b}'$ (= $\underline{b}$ + $\underline{c}$) are determined by the end point material of the alloy series and $\underline{c}$, the bowing parameter, measures the deviation from linearity.

The nonlinear composition dependence of the various energies is a measure of the change in crystal potential (both periodic and aperiodic) across the alloy field. The aperiodic part arises from the potential fluctuations introduced by the random placement of one element (cation or anion) in an otherwise compositionally ordered alloy. Recent extended x ray absorption fine structure (EXAFS) studies have furthur showed that in alloys such as GaInAs, the Ga-As and In-As bondlengths remain almost the same as that of the end point materials GaAs and InAs, although the average lattice constant follow Vegard's

law. This results in bondlength alternations and causes structural distortion in these materials.

In general, the bowing of the compositional variation of the band gaps is a result of the virtual crystal variation, microscopic alloy disorder as well as the structural disorder due to the bond length alternations[5]. The variation of the spin orbit splittings with composition as predicted by the VCA is essentially linear, though significant bowing were seen experimentally. In addition, when the alloy system is grown lattice matched to their substrate material, any virtual crystal variation due to volume effects are eliminated. Thus the bowing of the spin orbit splittings in these alloy systems can provide important information regarding the microscopic alloy disorder as well as the structural distortion arising from bondlength alternations[5].

In ternary alloys having zincblende structure it is found[6,7] that the bowing for

1. the spin orbit splitting parameter Δ_0 (of the $\Gamma_{15,v}$ valence band) is downward, i.e., positive value of $\underline{c}(\Delta_0)$
2. for Δ_1 (spin orbit spliting of the of the $\Lambda_{3,v}$ valence bands) it is upward, i.e., negative value of $\underline{c}(\Delta_1)$.

However the recent studies of the quaternary alloys InGaAsP/InP and the present study of GaAlInAs/InP have revealed negative values of $\underline{c}(\Delta_0)$ as well as $\underline{c}(\Delta_1)$. Listed in Table V are the values of $\underline{a}$, $\underline{b}$ and $\underline{c}$

for Δ_0 and Δ_1 for these quaternary systems as determined by various investigations. Note that for InGaAsP/InP system even though there is some variation in $\underline{c}(\Delta_1)$ all the reported numbers are negative. We have also listed in Table V the average of the three values of $\underline{a}$, $\underline{b}$, and $\underline{c}$.

According to the VV-B-W model[6,7] a positive value of $\underline{c}(\Delta_0)$ arises from an interband mixing of the s-like conduction band states $(\Gamma_{1,c})$ into the p like valence band states $(\Gamma_{15,v})$ which effectively decreases Δ_0. It should be pointed out that such a mixing may be due to either alloy potential fluctuations, bondlength alternations or both. In the VV-B-W model this interband effect can be written as

$$\Delta_0(x) = [1-f(x)]\langle\Delta_0(x)\rangle \tag{83}$$

where $\langle\Delta_0(x)\rangle = \underline{a} + \underline{b}'x$ see Eqn. 82. The function $f(x)$ is the fraction of the conduction band states mixed into the valence bands by alloy disorder and can be written as:

$$f(x) = D(x)/\bar{E}_0(x) \tag{84}$$

Table V. Values of the quadratic parameters a, b, and c for the spin-orbit splitting parameters Δ_0 and Δ_1 for $In_{1-y}Ga_yAs_xP_{1-x}$ and $(Ga_{1-x}Al_x)_{0.47}In_{0.53}As$ lattice matched to InP. All measurements were made at room temperature.

		a	b	c
		InGaAsP/InP		
Δ_0		0.114[a]	0.26[a]	-0.12[a]
		0.119[b]	0.30[b]	-0.107[b]
		0.11[c]	0.42[c]	-0.152[c]
	average	0.114	0.327	-0.093
Δ_1		0.135[a]	0.33[a]	-0.20[a]
		0.145[b]	0.33[b]	-0.064[b]
		0.133[d]	0.124[d]	-0.07[d]
	average	0.138	0.209	-0.11
		GaAlInAs/InP		
Δ_0		0.37[e]	0.10[e]	-0.10[e]
Δ_1		0.28[e]	0.03[e]	-0.03[e]

(a) Reference 78 (b) Reference 79

(c) Reference 80 (d) Reference 76

(e) This work

where $D(x)$ is the mean square fluctuation in crystal potential divided by an appropriate bandwidth, and $\overline{E}_0(x)$ is a weighted energy gap given by:

$$3/\overline{E}_0(x) = 2/\langle E_0(x)\rangle + 1/\langle E_0(x)+\Delta_0(x)\rangle \qquad (85)$$

In Eqn. 85 $\langle E_0(x)\rangle$ and $\langle E_0(x) + \Delta_0(x)\rangle$ are the compositionally linear averaged energy gap and spin orbit split component, respectively.

For the alloy $MF_{1-x}G_x$

$$D(x) = x(1-x)C_{FG}^2/A \qquad (86)$$

where A is a bandwidth constant (A=1 eV) and C_{FG} is the dielectrically defined electronegativity difference between elements F and G.

$$C_{FG} = be^2(z_G/r_G - z_F/r_F)\exp(-Rk_s) \qquad (87)$$

In the above expression b is a constant (b=1.5), z_G is the valency and r_G is the covalent radius of the element G, k_s is the linearized Thomas-Fermi screening wavevector for the valence electrons and $R=(r_G+r_F)/2$.

For the spin orbit splitting of the Λ_3 valence bands, VV-B-W proposed a disorder induced intraband interaction which effectively increases Δ_1 i.e., negative value for $\underline{c}(\Delta_1)$. This term can be written as :

$$\Delta_1(x) = \langle\Delta_1(x)\rangle + KD(x)/\langle\Delta_1(x)\rangle \tag{88}$$

where K is a factor which indicates the strength of the proposed selection rule for the disorder induced fluctuating potential.

The negative value of $\underline{c}(\Delta_0)$ and $\underline{c}(\Delta_1)$ for the quaternary alloys can be accounted for by including both intra and interband effects for these spin orbit splittings, thus generalizing the VV-B-W model. By including these effects for the spin orbit splittings we can write:

$$\Delta_i(x) = \langle\Delta_i(x)\rangle - \frac{D(x)}{\overline{E}_i(x)}\langle\Delta_i(x)\rangle + KD(x)/\langle\Delta_i(x)\rangle \tag{89}$$

where i= 0 or 1. In the above expression $\overline{E}_0(x)$ is given by Eqn. 85. and $\overline{E}_1(x)$ by:

$$3/\overline{E}_1(x) = 2/\langle E_1(x)\rangle + 1/\langle E_1(x)+\Delta_1(x)\rangle \tag{90}$$

for the quaternary alloy $In_{1-y}Ga_yAs_xP_{1-x}$

$$D(x,y) = \{C^2_{Ga-In} y(1-y) + C^2_{As-P} x(1-x)\}/A \tag{91}$$

where A is the bandwidth constant (A=1 eV) and C_{A-B} is the electronegativity difference between elements A and B. Note that we have interchanged x and y in the usual notation for InGaAsP. The lattice matched condition x = 2.2 y plus the values of C^2_{Ga-In} and C^2_{As-P} from Ref. (83) yields

$$D(x) = 0.07x + 0.149x(1-x) \tag{92}$$

In the case of the other quaternary system $(Ga_{1-x}Al_x)_{1-y}In_yAs$ the expression for D(x,y) is given by:

$$D(x,y)=\{C^2_{Ga-Al}xy(1-x)+C^2_{Ga-In}(1-x)(1-y)y+C^2_{Al-In}xy(1-y)\}/A \tag{93}$$

For lattice matched system y=0.47 and hence:

$$D(x) = 0.07 + 0.026x + 0.015x(1-x) \tag{94}$$

where we have used C_{Ga-Al} and C_{Ga-In} from Ref. (83) and C_{Ga-Al} form Ref. (84). In eqn. 92 and 94 only the term containing x(1-x) are relevant to calculate the bowing, since the other terms are related to the end points.

We have used the generalized expression Eqn. 89 to fit the $\Delta_0(x)$, and $\Delta_1(x)$ data for InGaAsP, with Eqn. 92 and InGaAlAs with Eqn. 94, grown lattice matched to InP. The results for InGaAsP are displayed in Fig. 33. The solid lines are given by the relation $E=\underline{a}+\underline{b}x+\underline{c}x^2$, with $\underline{a}$, $\underline{b}$ and $\underline{c}$ for $\Delta_0(x)$, and $\Delta_1(x)$ being the average values listed in Table V. The dashed line in Fig. 33 shows the fit to the generalized VV-B-W model (Eqns. 89 and 92). We have adjusted the magnitude of the parameters K to get the results for both $\Delta_0(x)$ and $\Delta_1(x)$ simultaneously, thus yielding a value of K=0.15. Note that the agreement between the average experimental values (solid lines), and the theory (dashed line) is good, and the negative bowing of Δ_0 and Δ_1 have been accounted for. By considering only the interband effect on the Δ_1 data, VV-B-W have obtained a value of K = 0.14 for ternary alloys, while Kelso et.al[76] have found a value of K = 0.07 for the InGaAsP system. Our value of K is close to that of VV-B-W but is somewhat larger than that quoted by Kelso et. al.

Plotted in Fig. 34 are the compositional variation of $\Delta_0(x)$ and$\Delta_1(x)$ for GaAlInAs/InP. The solid line represent a quadratic fit to the

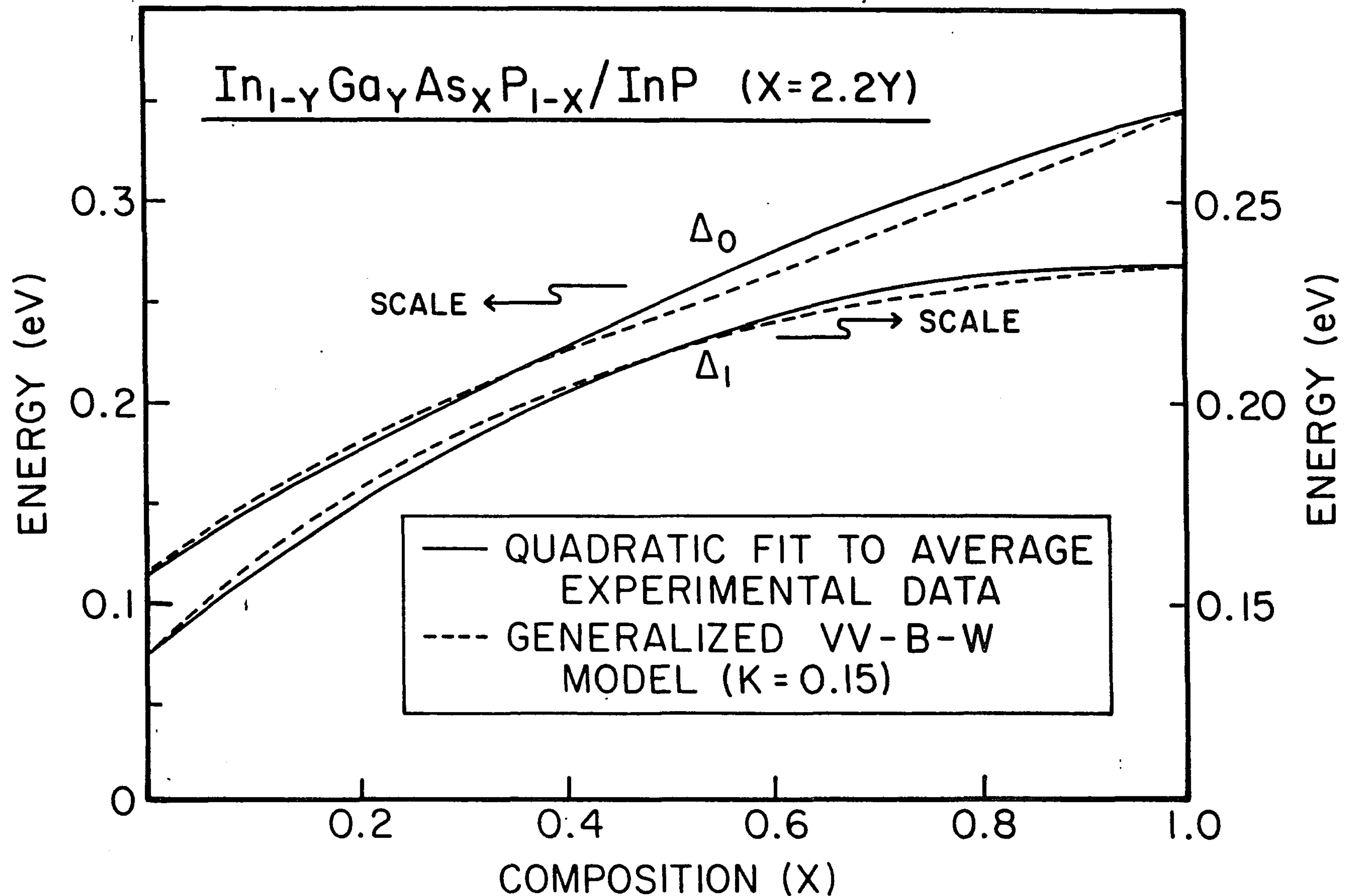

Fig. 33. Variation of the spin-orbit splittings with alloy composition x for $In_{1-y}Ga_yAs_xP_{1-x}$ lattice matched to InP. (x=2.2y)

experimental points with the parameters (a,b,c) listed in Table V. The dashed line again shows the fit to this data using Eqns. 89 and 94. We obtained a value of K=1.4 for this quaternary alloy system. As for the InGaAsP system, the generalized VV-B-W model again accounts for the upward bowing of Δ_0 as well as Δ_1.

The variation in magnitude of K between the two alloy systems is not completely understood at present. It may indicate the difference in strength of the proposed selection rule for the fluctuating potential, as pointed out by VV-B-W. For the $(Ga_{1-x}Al_x)_{0.47}In_{0.53}As$ alloy system, since the electronegativity difference of Ga and Al is small, we expect no significant deviation from linearity, for both $\Delta_0(x)$ and $\Delta_1(x)$ [see Eqn. (94)]. The fact that we observe an upward bowing for both $\Delta_0(x)$ and $\Delta_1(x)$ thus necessitating a larger value for K, may suggest that, there is more alloy disorder present in this system or there is a larger contribution to the valence-conduction band mixing as a result of the structural distortion in this alloy system.

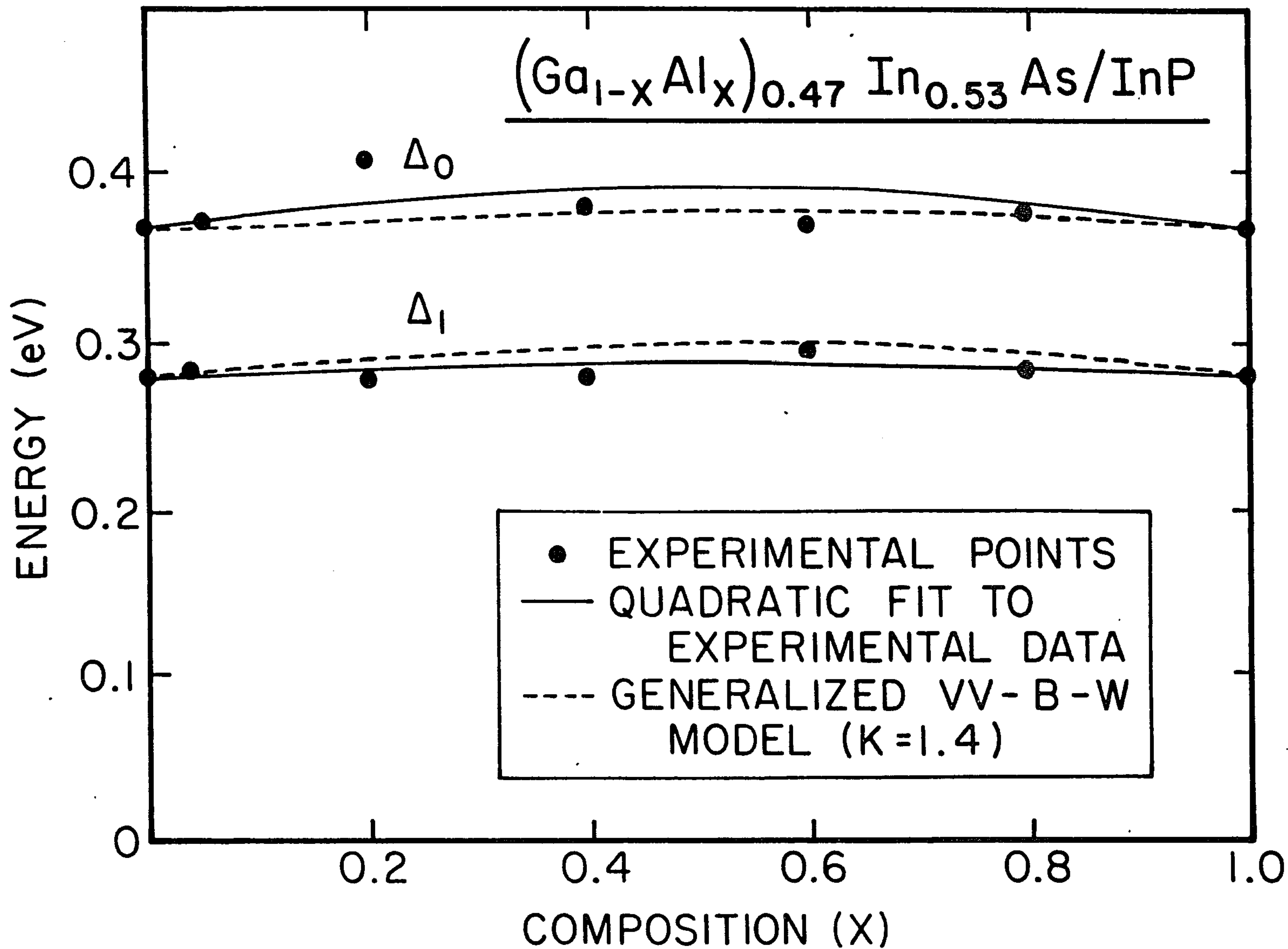

FIG. 34. Variation of the spin-orbit splittings with alloy composition x for $(Ga_{1-x}Al_x)_{0.47}In_{0.53}As$ grown lattice matched to InP.

Chapter IV

ION BEAM SPECTROSCOPY

In recent years there has been a tremendous growth in the use of ion beams for material analysis. Depth profiling of the constituents of various semiconductor structures can be accomplished by several of these ion beam techniques including Rutherford backscattering (RBS), nuclear profiling, and secondary ion mass spectrometry (SIMS)[85]. SIMS and other techniques like Auger electron spectroscopy (AES)[86], although have been used extensively for depth profiling, have the disadvantage that they require the removel of the layers of material by such procedures as ion milling and hence are destructive.

In RBS[87] light MeV ions (primarily protons or alpha particles) are scattered from target nuclei through their coulombic interaction. This technique has been extremely useful for the analysis of composition of surface films and thickness of these films. RBS, though nondestructive, in not suited to determine the presence of low z (atomic number) elements in a high z matrix since the scattering from the light element is obscured by that from the surrounding high z elements. The use of nuclear reactions, in these cases, provides adequate sensitivity and resolution.

Ion induced nuclear reactions have been applied to a wide range of near surface analysis problems. This technique consists of irradiating a sample with a beam of nuclear particles having sufficient energy so that nuclear reactions are produced and detecting the resulting characteristic radiation. The presence of narrow resonances in many light nuclei provide a method of accurate depth profile. In composite materials with Al as a constituent nondestructive depth profiling can be done by the use of $^{27}Al\ (p,\gamma)\ ^{28}Si$ reaction. The applicability of this technique for other elements is limited only by the requirement that sharp and isolated resonances exist in their reaction cross section.

4.1 Nuclear profiling technique

The Al profiling technique makes use of the nuclear reaction

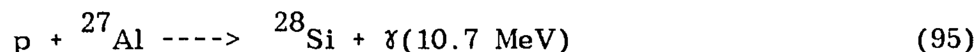

$$p + {}^{27}Al \dashrightarrow {}^{28}Si + \gamma(10.7\ MeV) \qquad (95)$$

In the cross section of this reaction there is a very narrow isolated resonance at a proton energy of 992 KeV (laboratory), the resonance width being only about 100 eV. Hence, if a sample is bombarded with protons at the resonance energy, the characteristic 10.7 MeV γ ray is proportional to the number of Al atoms present at the surface of the

target material, since as the protons penetrate the sample they lose energy and hence they are no longer at resonance. If the incident beam energy is raised, the yield of γ rays from the surface will be negligible because the protons are above the resonance energy. These protons reach the resonance energy at some depth inside the material and now the yield of the characteristic γ ray yield will be proportional to the Al at this depth. Hence, by measuring the γ ray yield versus proton beam energy the distribution of Al as function of depth x can be determined. Figure 35 shows the energy spectrum of the γ rays emitted from a pure GaAs sample and a GaAlAs sample. The integrated reaction cross section from a thick Al target is displayed in Fig. 36, exhibiting the sharp resonance at 992 KeV. When the GaAlAs layer is thicker than ~ 2.5 μm, the contribution from weaker and broader resonances at ~ 780 KeV and 1130 KeV have to be taken in to account[19].

There are several effects which tend to broaden the measured profile and thus limit the depth resolution. The principal among these are (1) energy straggling and (2) instrumental width.

4.1.1 Energy straggling

When a monochromatic beam of ions pass through a given thickness of the material there is an energy loss for the material as well as a spread in the energy distribution due to the statistical nature of the

energy loss mechanism, i.e., energy straggling. The energy straggling is caused by two factors: one due the electronic collision processes and the other due to the nuclear collision processes.

Several theories have been proposed to describe the straggling phenomena. The first theoretical work was done by Bohr[88] who described the process by successive binary collisions between the projectile ion and the target electron and obtained the following expression for the straggling width Ω_B:

$$\Omega_B^2 = 8\pi N z_1^2 z_2 e^4 x \tag{96}$$

where Ω_B is the straggling width (the full width at half maximum of the beam = $(4\ln 2)^{\frac{1}{2}}\Omega_B$, assuming a Gaussian energy distribution), z_1 and z_2 are the atomic numbers of the projectile and the target, respectively, N is the atomic density, e is the electronic charge, and x is the thickness of the target. This theory was based on three assumptions:

1. The velocity of the projectile is much greater than that of the orbital electrons of the target atoms.
2. The energy loss is small compared to the total energy of the projectile and
3. The target atoms are randomly distributed.

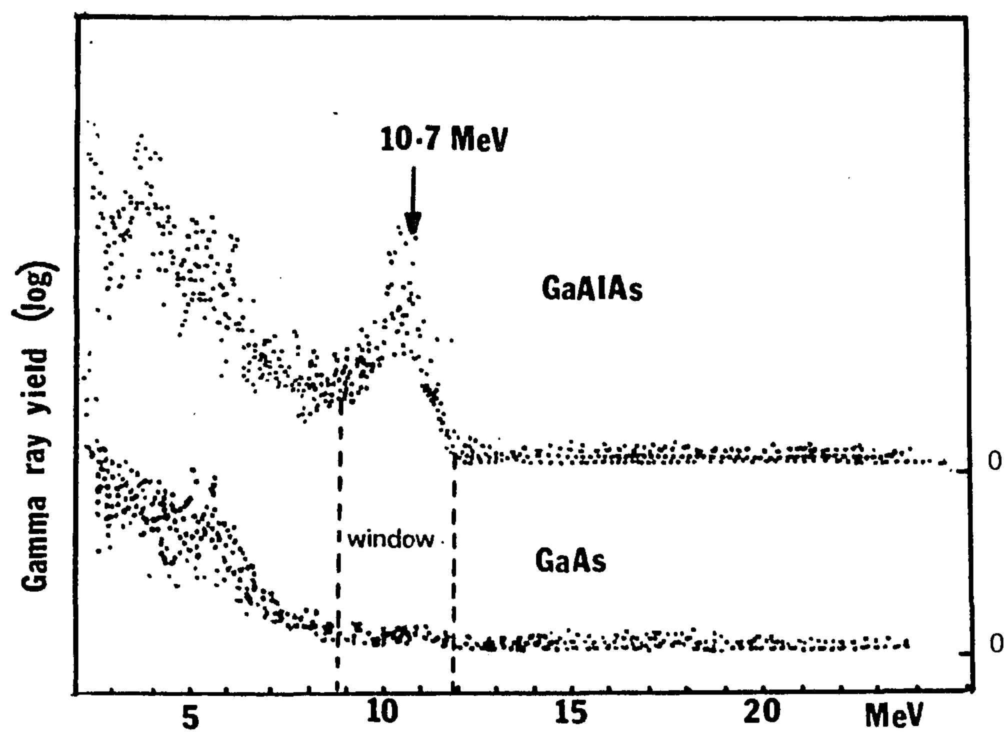

FIG. 35. Gamma ray yield from a pure GaAs sample and a $Ga_{1-x}Al_xAs$ sample.

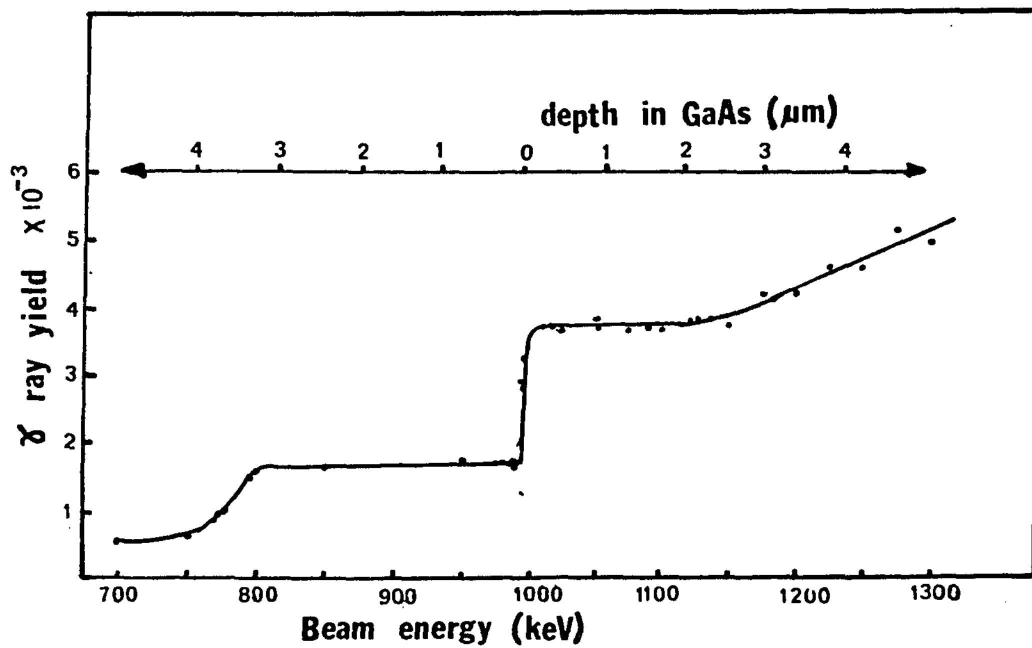

FIG. 36. Integrated reaction cross section for $^{27}Al(p,\gamma)^{28}Si$ reaction, measured with a thick target. (Ref. 19)

At low and medium energies the first assumption starts to break down. The third assumption neglects any correlation effects and effects due to channeling. Linhard and Sharff (LS)[89] have extended Bohrs theory by applying a correction factor for low and medium energies to get:

$$\Omega^2_{LS} = \Omega^2_B \text{ for } \chi \geq 3 \tag{97}$$

$$\Omega^2_{LS} = \Omega^2_B L(\chi) \text{ for } \chi \leq 3 \tag{98}$$

where χ is the reduced energy variable

$$\chi = v^2/(v_o^2 z_2) \tag{99}$$

v is the velocity of the projectile, v_0 is the orbital velocity of the Bohr hydrogen atom ($v_0 = e^2/\hbar$) and $L(\chi)$ is the stopping number which is related to the energy loss

$$dE/dx = (4\pi z_1^2 e^4 N z_2) L(\chi)/(mv^2) \tag{100}$$

where m is the electron mass. Bondurup and Hvelplund[90] has refined LS calculations by using a more realistic model for the atomic charge

distribution. Chu[91] calculated the straggling widths by using an atomic charge distribution based on the Hartree-Fock-Slater model and the Bondurup and Hvelplund's formulation. His results reveal an oscillatory structure in the straggling width as a function of the atomic number of the target material. A comparison of these various theoretical results are shown in Fig. 37.

The effect of the energy straggling is to produce an approximately Gaussian distribution for the energy of the proton beam with a mean energy given by the depth. For a given material the straggling width calculated from theory varies significantly from model to model, and also different experiments yield different value for K for the same material. One common feature of all the above theoretical treatments is that they predict a straggling width, Ω_s, (full width at half maximum = $(4\ln 2)^{\frac{1}{2}}\Omega_s$) proportional to the square root of the thickness of the target material x, i.e.,

$$\Omega_s = Kx^{\frac{1}{2}} \tag{101}$$

The proportionality constant K differs from model to model. The above relationship has also been verified by experiments.

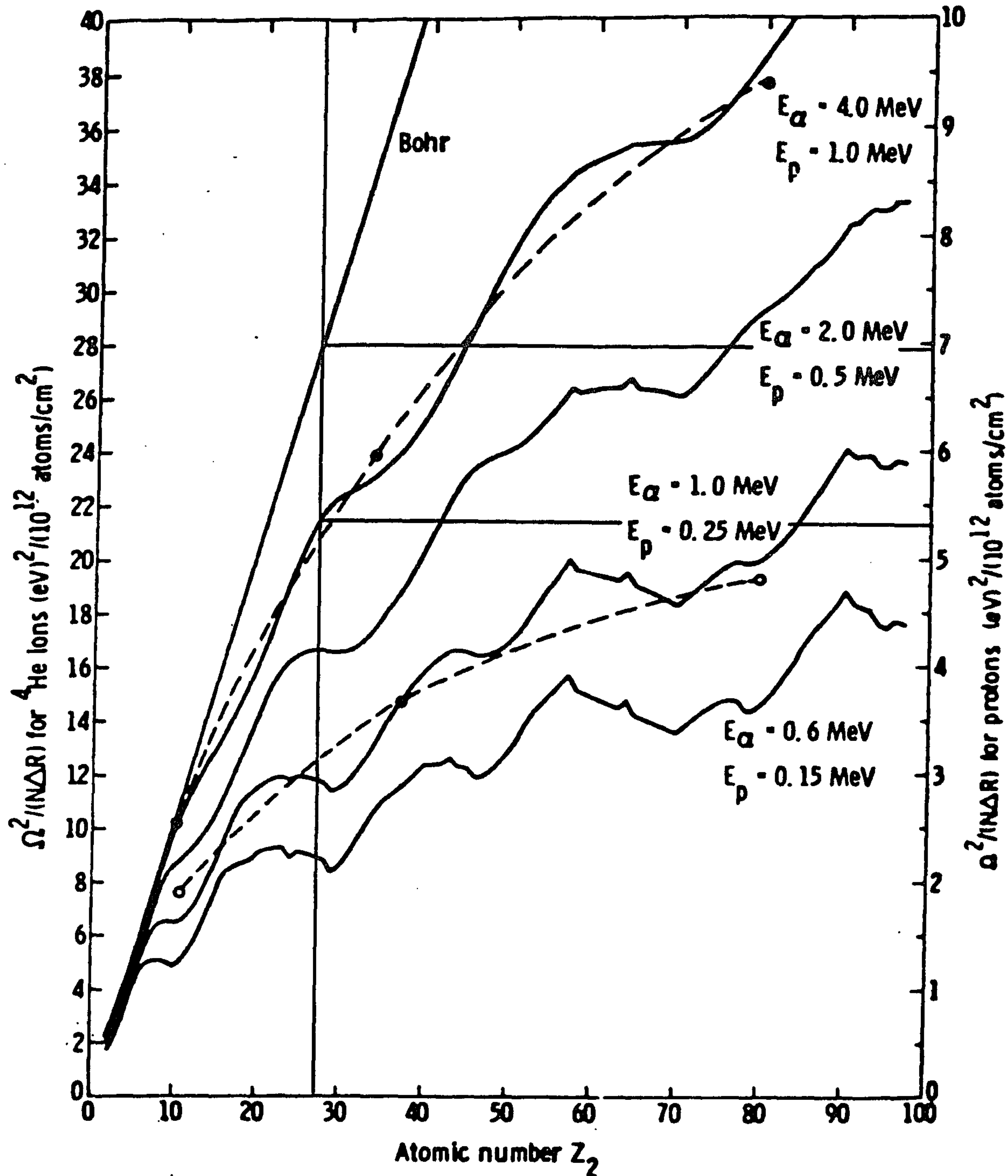

FIG. 37. Energy straggling calculated for protons (right scale) and for ^{4}He ions (left scale) for all elements at various energies. The dashed curve represent the calculations using Thomas-Fermi model while the solid curves represent the calculations of Chu (Ref. 91).

In order to extract the true Al profile from the measured yield it is necessary to have an accurate value for the straggling width in the material. This is especially important in the case of heterostructures with an abrupt or graded interface region or buried layer structures where for example GaAlAs layer in buried inside the GaAs epilayer.

There have been several experimental studies for the determination of the straggling width for different elements[92-93]. The discrepencies in the results between the various measurements for the same element is as much as 30 percent. Furthurmore, previous to this study there have been no experimental studies of straggling in GaAlAs. The estimation of the straggling width by interpolation between measured straggling values in nearby elements in the periodic table is also questionable, due the existence of an oscillatory behavior in straggling width as a function of atomic number, as shown by Chu[91].

The simple relationship between the straggling width and the thickness given by Eqn. 101 and the ability to make GaAlAs/GaAs samples with a step function profile provides a direct method of accurately determining the straggling parameter K in GaAlAs. In addition, this method is also applicable to determine the straggling parameter in GaAs if the samples with known profiles are prepared such that GaAs is grown on the top of GaAlAs.

4.1.2 Instrumental width

In addition to the broadening of the beam due to energy straggling there is a constant instrumental width due to the energy spread of the incident beam. This effect broadens the measured profile at the surface of the sample as well at any depth inside the sample. A typical instrument width is ~ 2.8 KeV.

Broadening due to the inherent width of the resonance is completely negligible in this case since the resonance width is only ~ 100 eV for the Al (p,γ) Si reaction at E_r = 992 KeV.

4.2 Experimental details

All the nuclear profiling experiments were done at the Brooklyn College Dynamitron accelerator. The schematic of the experimental setup is shown in Fig. 38. The ion source at the high voltage end of the machine generates and focuses protons for acceleration. These protons after acceleration pass through the energy analysing magnet and a slit feedback system which controls the energy. A switching magnet directs the beam to the beamleg containing the target. The beam size is limited by two apertures, one, 1 mm in diameter kept near the sample and the other, ~ 2 mm in diameter ~ 15 inches apart from the first aperture. These were made of tantalum to minimise any background radiation on proton bombardment. The proton beam in directed through these

apertures and focused onto the sample using electrostatic steerers and quadrupole lenses (electric and magnetic), located along the beam transport system.

The samples were mounted on a circular disc made of copper on which four samples can be mounted simultaneously. Copper was selected because it does not produce any background near 10.7 MeV and also it acts as a good heat sink. The disc is attached to a vacuum feedthrough by which the samples are rotated into position without breaking the vacuum. The vacuum inside the beamtube were maintained at 10^{-6} torr using a turbomolecular pump backed by a rotary pump.

Slight amounts of oil vapors reaching the beamtube from the pumps give rise to a serious problem of carbon buildup onto the target. The oil vapor dissociate on proton bombardment and the resulting carbon atoms deposit onto the target surface. Even small traces (several Å) of carbon deposition can easily be detected by studying the γ ray yield from a thick Al target. After long periods (few hours) of run the midpoint of the excitation curve seem to shift to higher energies indicating that the incident proton loses some of its energy before reaching the resonance energy. A coaxial cold trap was constructed near the target, which reduced this problem significantly.

The beam current was kept $\approx$ 200 nA/mm^2. A higher beam current appeared to heat up the sample.

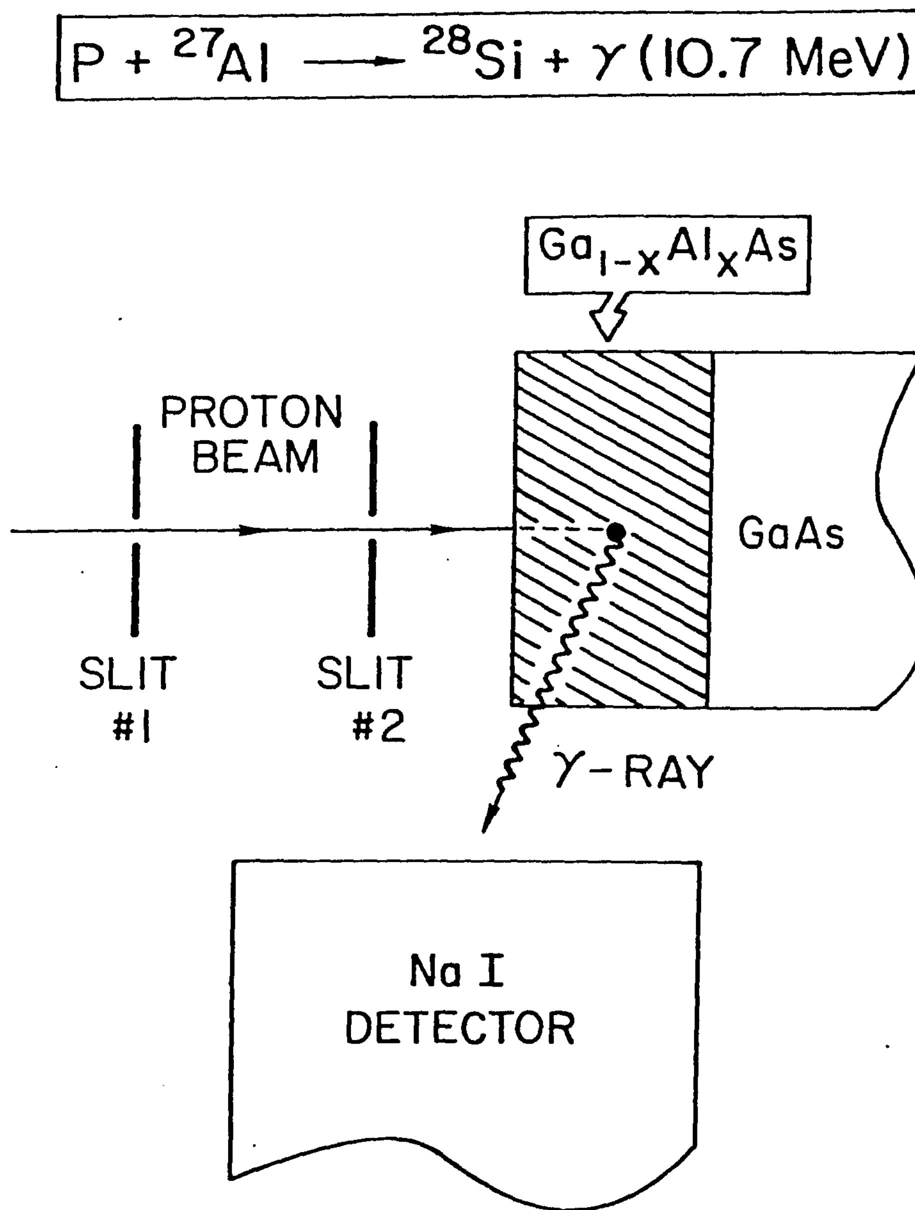

FIG. 38. Schematic representation of the experimental arrangement for nuclear profiling.

A block diagram of the detection system is shown in Fig. 39. The γ rays emitted from the sample are detected by the NaI detector (3" thick and 3" in diameter) kept ~ 1 cm from the sample. At this distance a leakage current (~ 10 nA) was noticed between the target and the ground, when the high voltage was applied to the detector. To avoid this effect the detector was enclosed in an insulating cup. The signals from the NaI detector was fed into a preamplifier and then to an amplifier (ORTEC model 452), the output of which was sent to the TN 1700 multichannel analyser. The discriminators were set such that only the 10.7 MeV peak is selected, as indicated by the window in Fig. 35. In this energy region a beam independent background of ~ 10 counts (due to cosmic rays) was found for a running time of ~ 5 minutes. In addition, there was a constant background ~ 25 counts/80 μcoulomb exited by the beam (in GaAs substrate, target chamber and beamleg). The output pulses were given to a scalar (ORTEC model 431) for counting.

The charge accumulated onto the sample surface is fed into a charge integrator (ORTEC model 439) which gives a pulsed output for preset amount of charge. This output pulses were counted with a second scalar (ORTEC model 776) operated in the master mode controlling the scalar counting the γ rays. The scalars were usually set to count the γ rays for 80 μcoulombs of charge.

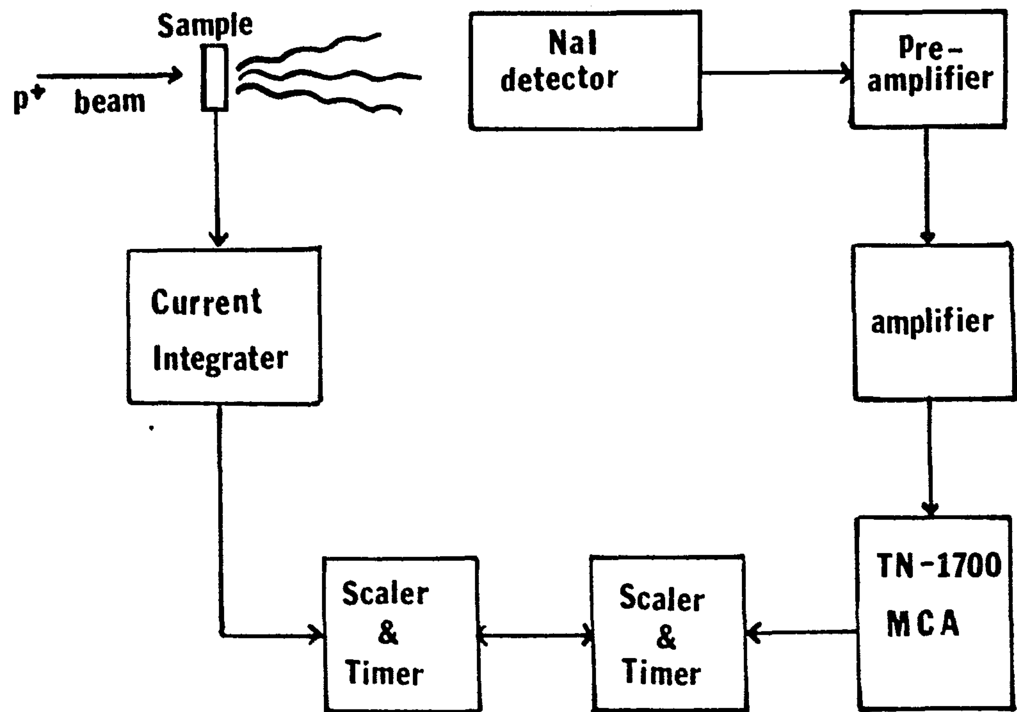

FIG. 39. Schematic representation of the detection system for the nuclear profiling measurements.

The incident energy was controlled using a slit feedback system following magnetic analysis. Previous to each run the energy calibration of the system was determined independently by measuring the excitation curve near for the Al (p,γ) Si reaction for a pure thick Al target. Care was taken not to alter the energy calibration during each run by maintaining the focusing parameters which seem to affect the calibration.

4.3 Sample details.

The samples used in this study were GaAlAs/GaS structures grown by MBE with various epilayer thicknesses. The sample characteristics are presented in Table VI. Two of the samples were fabricated with MBE grown GaAs buffer layers while the third sample was grown directly onto the GaAs substrate. For sample MBE 31-3 a buffer layer of p-GaAs (~ 1 μm), followed by a layer of n-GaAs substrate (~5000 Å) was grown on an n-type substrate at 600° C. This was followed by a GaAlAs epilayer (~ 1000 Å). For sample MBE 32-x, the epilayer of GaAlAs (~ 4000 Å) was grown on a semi-insulating GaAs substrate on which two buffer layers of GaAs - one p-type (~ 1.5μm) and the other n type (~ 2 μm) was grown by MBE at 550° C. In preparing the third sample MBE 49-4 the epilayer was grown directly onto a p-type GaAs substrate, which was thermally cleaned without excess As. The MBE

Table VI. Characteristics of the $Ga_{1-x}Al_xAs/GaAs$ samples used for nuclear profiling measurements.

Sample	Substrate	Buffer layer 1	Buffer layer 2	Epilayer thickness	Al composition
MBE 31-3	GaAs	1μm	0.5μm	1200Å	0.4
		p type	n type		
MBE 32-x	GaAs	1.5μm	2μm	4000Å	0.4
		p type	n type		
MBE 49-4	GaAs	nil	nil	8000Å	0.5

Table VII. The measured straggling coefficient (K_M) and thickness for the two samples MBE 31-3 and MBE 32-X. The ratio K_M/K_B, where K_B is the Bohr straggling coefficient, is also listed.

Sample	Thickness (A^o)	K_M (eV $A^{o-1/2}$)	$\frac{K_M}{K_B}$
MBE 31-3	1080 ± 20	72.0 ± 3.6	0.89 ± 0.05
MBE 32-x	3880 ± 80	68.3 ± 1.4	0.84 ± 0.02

procedures used for all samples were designed to produce abrupt interfaces between the GaAlAs and GaAs regions. The composition x was evaluated by Raman scattering[32] and found to be 0.4 for samples 31-3 and 32-x and x = 0.5 for sample MBE 49-4. These values were the same as predicted from the growth conditions.

4.4 Data analysis and results

Figure 40a and 40b shows the experimental γ ray yield, indicated by dots, for sample MBE 31-3 and MBE 32-x, the two step function samples, respectively, after background subtraction. In order to calculate the energy lost by the proton beam in traversing a given thickness of the material the following relation was used:

$$E_0 = E_r + \int_0^x (dE/dx')dx' \tag{102}$$

where E_r is the resonance energy (992 KeV) and dE/dx is the rate of energy loss of the protons in the solid. For the samples used in this study the maximum energy loss was ≤ 60 KeV and it was sufficient to use a linear fit to dE/dx.

$$dE/dx = a + bE \tag{103}$$

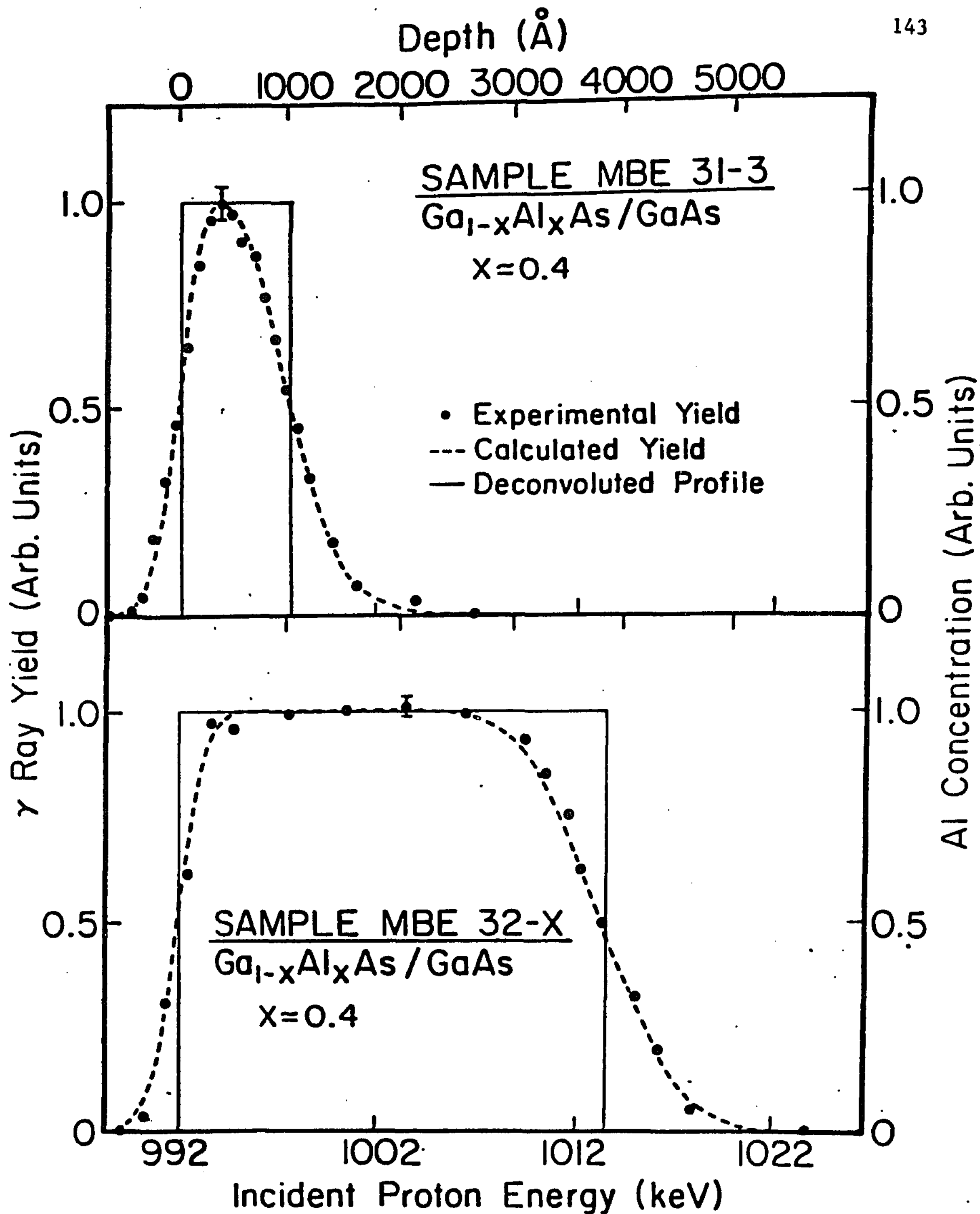

FIG. 40. Gamma ray yield (in arbitrary units) as a function of incident energy for MBE samples (a) 31-3 and (b) 32-x. The dashed lines represent best fit curves to the data (shown by dots) calculated from eqn. 106.

where the parameters a and b were determined from the stopping power data compiled by Anderson and Ziegler[94]. The stopping power for the composite material was determined by using the Bragg's rule[95].

$$\varepsilon^{A_mB_n} = m\varepsilon^{A} + n\varepsilon^{B} \qquad (104)$$

where $\varepsilon^{A_mB_n}$ is the stopping cross section of the compound A_mB_n or a mixture of atoms A and B in the atomic ratio m to n and where ε^{A} and ε^{B} are the stopping cross section of the constituents A and B.

The depth $x(E_0)$ indicated at the top of the figure was then calculated for which the energy loss was equal to the difference between E_0 and the resonance energy E_r.

Assuming a Gaussian distribution for the incident beam profile, the spread in energy of the incident beam (instrumental width) Ω_0 was determined by measuring the difference between 0.12 and 0.88 points of the step height of the excitation yield curve for the pure thick Al target. We obtain a value Ω_0 = 2.8 KeV for the incident beam spread. This has again been verified from the slope of the front surface yield of the GaAlAs/GaAs samples.

The beam energy distribution at a depth x inside the material $f(x,E_0)$ is given approximately by a Gaussian function, i.e.,

$$f(x,E_0) = (\Omega_0^2+\Omega_s^2)^{-\frac{1}{2}}\exp[-(E_0-E(x))^2/(\Omega_0^2+\Omega_s^2)] \tag{105}$$

where Ω_0 is the incident beam width, Ω_s is the straggling width, E_0 is the incident proton energy and $E(x)$ is the mean energy of the protons at a depth x as obtained from Eqn. 102. Figure 41 shows a plot of the beam profile spread due to the straggling at various depths inside the sample according to the Bohr theory. The energies labeling the curves are proton bombarding energies. Each curve itself represents the depth distribution of protons reaching 992 KeV, the resonance energy. An initial beam spread Ω_0 = 2.8 KeV is assumed in the calculation.

The true Al profile $\rho(x)$ is related to the measured yield $Y(E_0)$ by the expression:

$$Y(E_0) = A\int_0^{\infty}\rho(x)f(x,E_0)dx \tag{106}$$

where A is the normalization depending on the detection geometry, reaction cross section etc.

4.4.1 Evaluation of the straggling parameter.

Since samples MBE 31-3 and MBE 32-x are fabricated to have step function profiles. The functional form of $\rho(x)$ in Eqn. 106 is known i.e.,

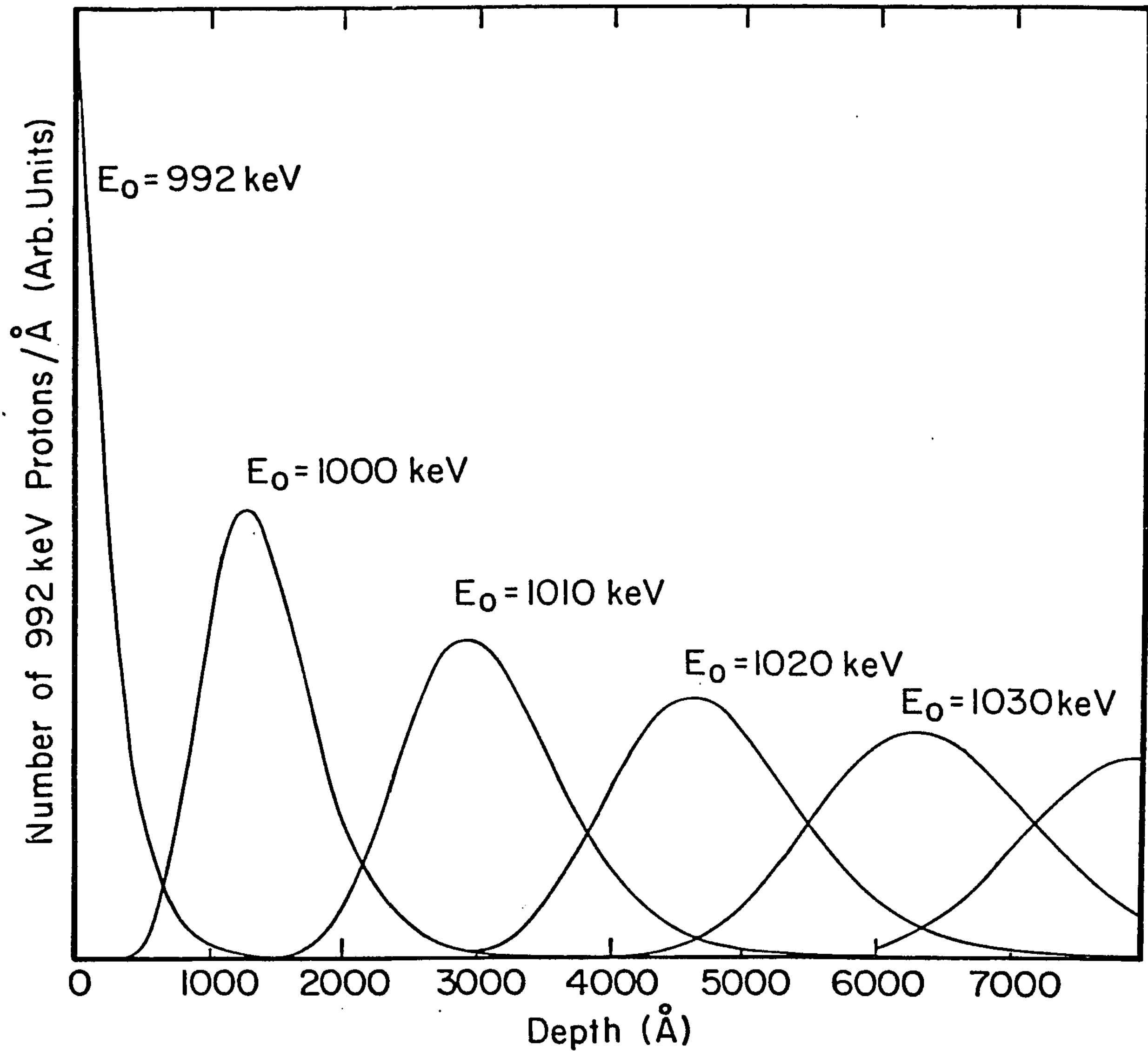

FIG. 41. Beam profile due to straggling at various depths, according to Bohr theory. The energies labeling the curves are proton bombarding energies. Each curve represents the depth distribution of protons reaching 992 KeV, assuming an initial beam energy spread of 2.8 KeV (FWHM) about the bombarding energy.

$$\rho(x) = C \text{ for } x \leq t \quad (107)$$
$$= 0 \text{ for } x \geq t$$

where t is the thickness of the epilayer and C is the absolute Al concentration of the film. The incident beam width Ω_0 is known from the thick Al target yield and the straggling width is given by $\Omega_s = Kx^{\frac{1}{2}}$.

A least square fitting of the data was done on the γ ray yield for samples MBE 31-3 and MBE 32-x using Eqns. 105, 106 and 107 with A, the normalization, K, the straggling parameter and t, the thickness as adjustable parameters. All the integrations were done using Simpson's rule. The parameters were varied to get the best fit with the experimental yield curve. Thus both epilayer thickness and the straggling parameter K could be obtained from the experimental data. The dashed lines Figs. 40a and 40b represents the calculated yield $Y(E_0)$ using these best fit values. The solid line represents the resultant step function profiles used in generating these best fit curves. The agreement between the experimental points and the calculated yield is quite good.

Table VII tabulates the results, presented as the best fit values of the straggling parameter K and the epilayer thickness t for samples MBE31-3 and MBE 32-x. In third column, the measured coefficient K_M from Eqn. 101 is presented, and in the fourth column K_M is compared with K_B, the coefficient calculated form the Bohr theory Eqn. 96. The

consistency of K_M for both samples confirms the $x^{\frac{1}{2}}$ dependence of the straggling width Ω_s and the fact that K_M is somewhat smaller than K_B is consistant with that of the more recent calculations. The experimentally determined thickness for both samples is in good agreement with that predicted from the growth conditions.

4.4.2 Effect of substrate preparation.

Having thus evaluated K it is now possible to examine GaAlAs/GaAs structures grown under different conditions. Figure 42 shows the γ ray yield results for the sample MBE 49-4, the sample where the epilayer was grown directly on the GaAs substrate. For this sample the transition region could not be fit assuming a step function distribution for $\rho(z)$ and using the same deconvolution procedure and the straggling parameters as for the previous two samples. The data indicate a nonabrupt transition at the interface of this sample. For simplicity we have chosen to represent this transition by a straight line, the slope of which was varied in the fitting procedure similar to that used for the other two samples. The straight line giving the best fit to the data, after convolution with the straggling function obtained as described above and with the initial beam broadening, is represented by the solid line in Fig. 42. Although this line is a simplified representation of the nonabruptness of the transition, it does indicate an interfacial region of approximately 2000 Å in width for this sample.

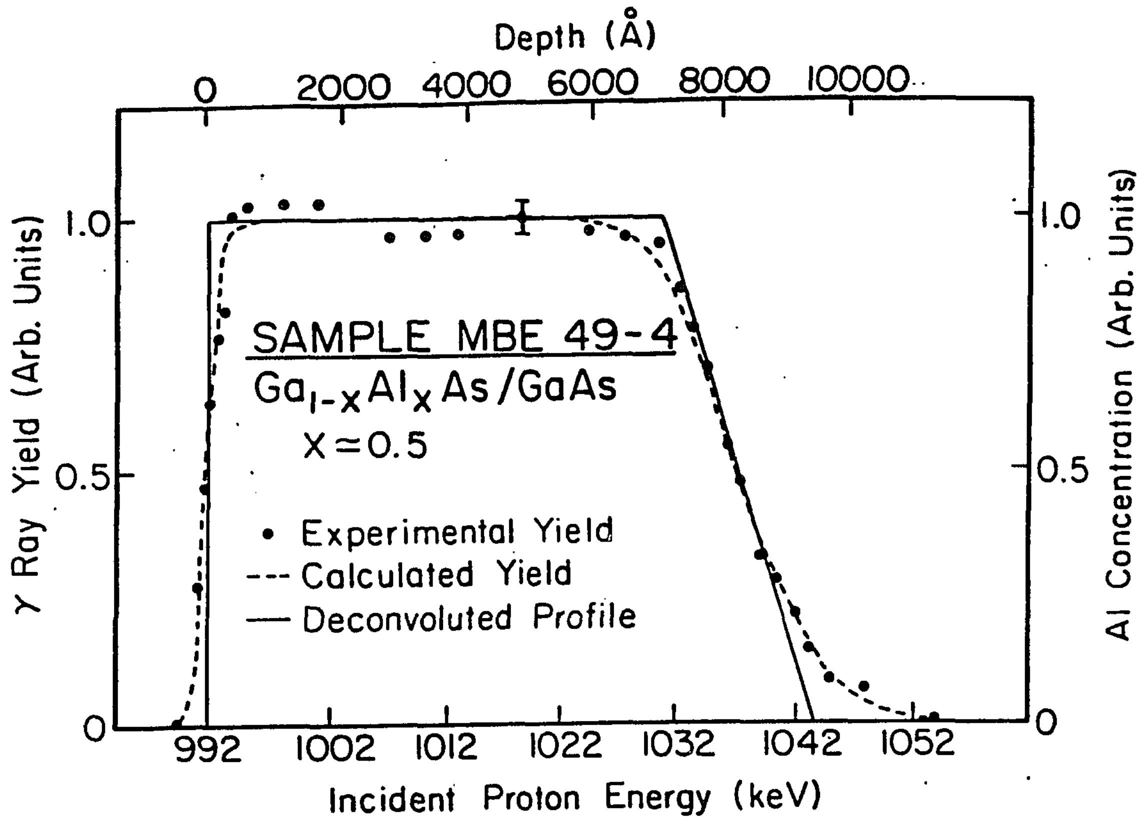

FIG. 42. Gamma ray yield (in arbitrary units) as a function of incident proton energy for MBE-grown sample MBE 49-4. The data are shown by dots. A representative error bar is shown. The dashed line shows the best fit curve to the data calculated from eqn.106 using the profile distribution represented by the solid line. The scale at the top of the figure represents the depth corresponding to a given proton energy.

The nonabruptness of the interface in this sample is probably due to differences in stoichiometry between the substrate surface, which is thermally cleaned without excess As, and the MBE grown GaAs surfaces (sample MBE 31-3 and MBE 32-x) which were grown under excess As, and also had a shorter exposer time prior to growth of the GaAlAs layer. This nonabrupt interface is similar to that seen in a previous profiling study done on GaAlAs layers grown by LPE. This similarity raises the possibility that the Al concentration gradient at the interface may be related to substrate preparation rather than to epilayer growth techniques, and opens up the speculation that abrupt interface concentration gradients might be produced in samples in which GaAlAs layers were LPE grown on top of buffer layers of GaAs.

Chapter V

Summary and Conclusions

This thesis is an investigation of the compound semiconductor alloy systems $Ga_{1-x}Al_xAs/GaAs$ and $(Ga_{1-x}Al_x)_{0.47}In_{0.53}As/inP$ using three spectroscopic techniques, i.e., Raman scattering, electrolyte electroreflectance, as well as nuclear profiling. Samples used in this study were prepared by a variety of growth techniques including MBE, LPE, MOCVD and VPE, and range in composition $0 \le x \le 0.9$ for $Ga_{1-x}Al_xAs$ and $0 \le x \le 1$ for $(Ga_{1-x}Al_x)_{0.47}In_{0.53}As$.

The effect of microscopic alloy disorder on the vibrational properties as well as in the electronic properties were investigated from the results of Raman scattering and EER measurements. The first order LO phonon Raman spectra in the representative ternary alloy systems $Ga_{1-x}Al_xAs/GaAs$ (two mode behavior), and $Ga_{0.47}In_{0.53}As/inP$ (apparent one mode behavior), shows an asymmetrically broadened lineshape. We find for small values of x, the "AlAs like" mode in $Ga_{1-x}Al_xAs$ is very broad and asymmetric, whereas the "GaAs like" mode is more symmetric and sharper. As the Al composition increases, the "GaAs like" mode becomes broader and less symmetric whereas the

reverse happens to the "AlAs like" mode i.e., this mode becomes sharper and more symmetric.

We have for the first time quantitatively explained this asymmetric broadening of the first order LO phonon Raman lineshapes in these alloy systems using a "spatial correlation" model related to q vector relaxation induced by the microscopic alloy disorder. Due to the alloy potential fluctuations the correlation length of the phonon becomes finite which leads to a relaxation of the $q \approx 0$ selection rule of the first order Raman scattering.

A quantitative analysis of these lineshapes have provided important information regarding the nature of the disorder. A Gaussian correlation function seem to best describe the effect of these microscopic alloy disorder. From this analysis we find:

1. The "GaAs like" mode and "AlAs like" mode in $Ga_{1-x}Al_xAs$ have different correlation lengths, depending on the composition, which suggests that, there is different degree of disorder in the two sublattices. At low Al composition the Al sublattice have a high degree of disorder as seen by the relatively small correlation length, whereas the GaAs sublattice is fairly ordered. As the Al composition x increases the situation reverses. i.e., the Al sublattice becomes more and more ordered at the expense of the Ga sublattice.

2. The correlation length and hence the alloy disorder depends on the growth techniques as well as the growth parameters.

Our results furthur indicate that the Ga sublattice in $Ga_{0.47}In_{0.53}As$ is more ordered than $Ga_{0.5}Al_{0.5}As$.

We have performed the first EER study on the quaternary alloy system $(Ga_{1-x}Al_x)_{0.47}In_{0.53}As$. grown lattice matched to InP. The various interband transition energies E_0 (fundamental gap), $E_0+\Delta_0$ (spin orbit split component), E_1, $E_1+\Delta_1$, E_0' and $E_0'+\Delta_0'$ as well as the spin orbit splittings of the valence bands Δ_0 and Δ_1 were accurately determined. The energies of the various interband transitions as well as the spin orbit splittings are found to follow a quadratic relationship. Previous to this study, only the variation of E_0 with composition was known for this material (from room temperature photoluminescence measurements). The variation of the fundamental gap E_0 is in good agreement with the available bandstructure calculation as well as the photoluminescence measurements.

The spin orbit splittings Δ_0 and Δ_1 exhibit a negative bowing similar to that found in the other quaternary alloy system GaInAsP. In lattice matched alloys the bowing of the spin orbit splittings is a result of the APF and the structural distortion due to the bondlength alternations. VV-B-W proposed a model based on the disorder induced mixing of the valence band wave function into the conduction band wave functions.

Their model predict an upward bowing for Δ_1 whereas a downward bowing for Δ_0. We have generalized the VV-B-W model including both intra and interband mixing, disorder induced or that due to the structural distortion, to account for the composition dependence of the valence band spin orbit splittings Δ_0 and Δ_1 in the quaternary alloys InGaAsP and GaAlInAs grown lattice matched to InP. The generalized model successfully accounts for the upward bowing found only in the lattice matched quaternary alloy systems as well as the behavior of Δ_1. The model has an adjustable parameter K, which is a measure of the strength of the proposed selection rule for the fluctuating potential. We obtain a value of K=0.15 for the GaInAsP system, and K=1.4 for the GaAlInAs system. The difference in the value of K may indicate the varying degree of alloy disorder as well as structural distortion in the two systems.

Raman scattering study in GaAlAs/GaAs heterostructures prepared under different condtions has revealed several important aspects regarding the epilayer, interface as well as the substrate material. Information is obtained regarding (1) crystal quality (2) alloy composition of the epilayer (3) band bending and (4) carrier depletion. The epitaxial layer of GaAlAs in sample SCL-379 which was grown on a strained substrate had significantly poorer crystalline quality compared to those of SCL-392 and SCL-400. The substrates E-820 and E-1068

used in growing SCL-392 and SCL-400, respectively, were of much better quality exhibiting very little symmetry forbidden modes as well as disorder activated modes. The presence of LO phonon-plasmon coupled modes as well as the unscreened LO phonon clearly showed that there is a charge depleted region near the GaAs surface resulting from a surface bandbending. The frequency position of the coupled modes provided a direct way of determining the bulk carrier concentration in these substrates. Since the penetration depth of light was large enough, signals were seen from both epilayer as well as GaAs near the interface. In the heterostructure the frequency position of the coupled mode arising from the GaAs region showed that the GaAs near the interface region had a lower carrier concentration than that was present initially before the epilayer was grown. These results are explained as due to carrier depletion from the substrate to the epilayer. The absence of the unscreened LO phonon modes from the substrates region of the heterostructure showed that there is no bandbending at the GaAs near the interface. A possible mechanism for the activation of the symmetry forbidden modes as seen in sample SCL-379 is given in terms of internal strain.

The electroreflectance measurements on these samples again confirmed the conclusions regarding the quality of the various epilayers. The composition of the three samples as determined from

Raman spectra and the EER measurements agree within experimental error.

Nuclear profiling technique has been developed as a powerful tool to obtain accurate depth profiles in GaAlAs/GaAs structures. The major limitation to the depth resolution is the energy straggling of the projectiles resulting from the statistical nature of the energy loss mechanism. We have done the first energy straggling measurements in GaAlAs using nuclear reaction technique. The samples were prepared by MBE. We obtain in GaAlAs the straggling parameter to be lower than that predicted by the Bohr theory. Our results agree with the more recent calculations. These results furthur confirm that the straggling width is proportional to the squareroot of the thickness.

We have obtained the epilayer thickness accurately in the various samples. We have also noticed the importance of growing buffer layers of GaAs for obtaining sharp interface regions. The sample MBE 49-4 which was grown without the buffer layer exhibits an interface region which is approximately 2000 Å wide.

The conclusions of this study can be summarized as follows:

1. Raman spectroscopy, Modulated optical spectroscopy and Nuclear profiling technique are powerful tools to, investigate the vibrational, electronic, and physical properties of compound semiconductors such as GaAlAs and GaAlInAs.

2. The asymmetric broadening of first order LO phonon Raman lineshapes in alloy semiconductors such as GaAlAs and GaInAs is a manifestation of q-vector relaxation induced by the microscopic alloy disorder. Quantitative information regarding the disorder can be obtained by a detailed analysis of these lineshapes.

3. The microscopic alloy disorder as seen by the phonons, is different for the Ga sublattice and Al sublattice in GaAlAs, and depends in general, on the composition, growth conditions as well as the growth technique.

4. The Ga sublattice in $Ga_{0.47}In_{0.53}As/InP$ seems to be more ordered than that in comparable GaAlAs.

5. The compositional variation of the various interband transitions E_0 (fundamental gap), $E_0+\Delta_0$ (spin orbit split component), E_1, $E_1+\Delta_1$, E_0' and $E_0'+\Delta_0'$ as well as the spin orbit splittings of the valence bands Δ_0 and Δ_1, for the quaternary $(Ga_{1-x}Al_x)_{0.47}In_{0.53}As$, were accurately determined. The energies of the various interband transitions as well as the spin orbit splittings is found to follow a quadratic relationship.

6. In contrast to ternary alloy semiconductors, the spin orbit splitting Δ_0 is found to have an upward bowing in lattice matched quaternary alloys GaAlInAs and GaInAsP.

7. The generalized VV-B-W model including the intra and interband effects due to alloy disorder and that due to structural distortion, successfully accounts the upward bowing of Δ_0 and Δ_1 in GaAlInAs as well as GaInAsP grown lattice matched to InP.

8. Raman scattering is demonstrated to be a powerful technique to characterize the epilayer, interface and substrate in GaAlAs/GaAs heterojunction.

9. We have obtained the straggling parameter in GaAlAs using the the nuclear profiling technique. The straggling width varies as the squareroot of thickness.

10. We have observed the importance of growing buffer layers to obtain sharp interfaces in GaAlAs/GaAs heterostructures.

Bibliography

1. M. Cardona, Light scattering in Solids Topics in applied physics, Vol. 8 ed. by M. Cardona (Springer-Verlag, Berlin, Heidelberg, New York 1975).
2. W.Hayes and R.Louden, Scattering of light by crystals. (John wiley, New york, 1978).
3. M. Cardona, Modulation spectroscopy (Academic, New York, 1969)
4. D.E. Aspnes, Handbook of Semiconductors edited by Balkanski Vol 2, (North Holland, 1980) chap. 4.
5. J.C. Mikkelson, Jr. and J.B. Boyce Phy. Rev. B 28 7130 (1983)
6. J.A. Van Vechten, O. Berolo and J.C. Wooley, Phys. Rev. Lett. 20, 1400 (1972).
7. O. Berolo, J.C. Wooley and J.A. Van Vechten, Phys. Rev. B 8, 3794 (1973).
8. D.J. Chadi, Phys. Rev. B, 16, 790 (1977).
9. A.S. Barker and A.J. Sievers, Rev. Mod. Phys., 47 , S2 (1975) and references therein.
10. R.Bonneville, Phys.Rev.,B 24, 1987 (1981)

11. D. Olego ,T.Y. Chang, E. Silberg, E.A. Caridi and A. Pinczuk Appl. Phys. Lett. 41, 476 (1982).

12. F. Aymerich, Phys. Rev. B 26, 1968 (1982).

13. F. Aymerich, Phys. Rev. B 28, 6071 (1983).

14. See, for example, A.G. Milnes and D.L. Feucht, Heterojunctions and Metal-Semiconductor Junctions (Academic, New York, 1972), and references therein.

15. See, for example, H. Hovel, Solar Cells, Semiconductor and Semimetals (Academic, New York, 1975), Vol. II, and references therein.

16. J.M. Woodall and H.J. Hovel, Appl. Phys. Lett. 21 379 (1972).

17. S.C. Lee and G.L. Pearson, Solid state electronics 24, 563 (1981).

18. H.C. Casey,Jr.,A.Y.Cho, D.V. Lang, E.H. Nicollian and P.W. Foy, J. Appl. Phys. 50, 3484 (1979).

19. P. Bayerl, W. Pabst and P. Eichinger, Ion beam surface layer analysis Vol 1, edited by O. Meyer, G. Linker, and F. Kappeler (Plenum press, New york, (1975)

20. J.S. Rosner, P.M.S. Lesser, F.H. Pollak, and J.M. Woodall, J. Vac. Sci. Technol. 19, 584 (1981).

21. W. Richter, Springer Tracts in Modern Physics, Solid State Physics, Vol 78, (Springer, Verlag, Berlin, 1976).

22. R. Louden, Adv. in Physics 13, 423 (1964).

23. E. Burstein and A. Pinczuk, "Light Scattering by collective excitations in dielectrics and Semiconductors", The Physics of Optoelectronic materials. pp 33-79; ed. by W.A. Albers (Plenum press, New York, 1971).

24. G. Abstreiter, M. Cardona, and A. Pinczuk, Light Sacttering by free carrier excitations in Semiconductors in Light scattering in Solids Vol IV, (Springer-Verlag, Berlin, Heidelberg, New york 1975).

25. A. Pinczuk and E. Burstein In /1/ Chap. 2.

26. E. Anastasakis, Dynamical properties of Solids edited by G.K. Hoton and A.A. Maradudin (north Holland Publishing Co., 1980), chap. 3.

27. G. Abstreiter, A. Pinczuk, R. Trommer and M. Cardona, Solid State Commun. 21, 959 (1977).

28. Y.N. Shen, W. Shockley, and G.L. Pearson, Phy. Rev. 151, 648 (1966).

29. I.F. Chang and S.S. Mitra, Phy. Rev. B. 172 924 (1968).

30. I.F. Chang and S.S. Mitra, Phy. Rev. B. 2 1215 (1970).

31. H.C. Gupta, G. Ahuja, S. Prakash, L.M. Tiwari and B.B. Tripati, Phy. Rev. B 28 7191 (1983)

32. R. Tsu, H. Kawamura and L. Esaki, in Proceedings of the Eleventh International Conference on the Physics of

Semiconductors , Warsaw, 1972, edited by M. Miasek (P.W.N. Polish Scientific, Warsaw,1972) p.1135.

33. T.P. Pearsall, R. Carles and J.C. Portal, Appl.Phys.Lett. 42,436 (1983)

34. P.Parayanthal, F. H. Pollak and J. M. Woodall, Appl.Phys.Lett. 40 ,961(1982).

35. R. Trommer, E. Anastassakis and M. Cardona, in Light Scattering in solids, edited by M. Balkanski, R.C.C. Leite and S.P.S. Porto (Flammarion, Paris, 1976) p. 396.

36. See, for example, R.Tsu, Proc. Photo Optical Instrumentations Engineers 276, 78 (1981) and references therein.

37. G. Abstreiter, E. Bauser, A. Fisher and K. Ploog, J. Appl. Phys. 16, 345 (1979), and references therein.

38. D.J. Evans and S. Ushioda, Phys. Rev. 9, 1638 (1974).

39. B. Jusserand and J. Saprial, Phys. Rev. B 24 7194 (1981).

40. N. Saint-Ericq, R. Carles, J.B. Renucci, A.Zwick and M.A. Rennuci, Solid State Commun. 39, 1137 (1981).

41. F.H. Pollak in Proceedings of the Society of Photo Optical Instrumentation Engineers edited by F.H. Pollak and R.S. Bauser (SPIE, Bellingham, Washington, 452 26, (1984).

42. H. Mausi, P.B. Klein, R.K. Chang, R.H. Callender, and R.J. Chicotta in Proceedings of the Twelfth International Conference

on the phÿsics of Semiconductors edited by M.H. Pilkuhn (B.G. Teubner Stuttgart), p. 509.

43. G.L. Pearson and D. Cheung, Quaterly Progress report for period 1 Oct. through 31 Dec. 1973, Solid State Electronics Laboratory, Stanford University, California.

44. D. Olego and M. Cardona, Phys. Rev. B, 24, 7217 (1981).

45. K.K. Tiong, P.M. Amirtharaj, P. Parayanthal and F.H. Pollak Solid State Commun., 50, 891 (1984).

46. ·Katayama, K. Murase and H. Kawamura, Phys. Rev. Lett. 33, 1481 (1974).

47. R.. Dornhaus, R. Farrow and R. Chang, Solid State Commun. 32, 375 (1979).

48. T.N. Krabach, N. Wada, M. V. Klein, K. C. Cadien and J. E. Green, Solid State Commun., 45 , 895 (1983)

49. B.A. Weinstein, Solid State Commun., 20 , 999 (1976).

50. A.S. Barker,Jr., J. L. Merz, and A. C. Gossard, Phys.Rev.,B 17 , 3181 (1978)

51. K. Katimoto and T. Katoda, Appl.Phys.Lett. 40 826 (1982).

52. R. Shuker and R.W. Gamon, Phys. Rev. Lett., 25 , 222 (1970); ibid Proc. Second Int. Conf. Light Scattering in Solids , Paris, 1971, ed. by M. Balkanski (Flammarion Sciences, Paris, 1971)) p. 334

53. H. Richter, Z.P. Wang and L. Ley, Solid State Commun., 39 , 625 (1981).

54. R.J. Nemanich, S.A. Solin and R.M. Martin, Phys. Rev. B 23 6348 (1981).

55. K.K. Tiong, P.M. Amirtharaj, F.H. Pollak, and D.E. Aspnes, Appl. Phys. Lett., 44 122 (1984).

56. M. Teicher, R. Beserman, M.V. Klein, and H. Morkoc, submitted to Phys. Rev. B.

57. C. Kittel, Introduction to Solid State Physics , 3rd ed. (Wiley, New York, 1967), chap.5.

58. J.T. Waugh and G. Dolling, Phys. Rev., 132 , 2410 (1963)

59. B.O. Seraphin Semiconductors and Semimetals Vol 9, Edited by R.K. Willardson and A.C. Beer (Academic press, New York, 1972).

60. D.E. Aspnes and Bottka, Semiconductors and Semimetals Vol 9, Edited by R.K. Willardson and A.C. Beer (Academic press, New York, 1972).

61. Y. Hamakawa and T. Nishino in Optical properties of SolidsNew developments edited by B.O. Seraphin (North Holland, Amsterdam, 1976) chap. 6.

62. M. Cardona, K.L. Shaklee, and F.H. Pollak, Phy.Rev. 154, 696 (1967).

63. F.H. Pollak in Proceedings of the Society of Photo Optical Instrumentation Engineers edited by D.E. Aspnes, S. So and R.F. Potter (SPIE, Bellingham, Washington, 276, 142 (1981).

64. M. Cardona Advances in Solid State Physics Vol 10, Festkorperprobleme, (pergaman, Vieweg, p 125).

65. L. Van Hove, Phy. Rev. 89 1189 (1953).

66. B.O. Seraphin and N. Bottka, Phy. Rev. 145, 628 (1966).

67. D.E. Aspnes and J.E. Rowe, Phy. Rev. B, 5, 4022 (9172).

68. D.E. Aspnes and J.E. Rowe, Solid St. Commun. 8, 1145 (1970).

69. Enderlein, Phy. Stat. Solidi, 26 509 (1968).

70. Porsh, Phys. Stat. Solidi 27, 359 (1968).

71. D.E. Aspnes, Surf. Sci. 37, 418 (1973).

72. D.E. Aspnes and A. Frova, Solid St. Commun., 7, 155 (1969).

73. J.E. Rowe and D.E. Aspnes, Phy. Rev. Lett. 25 162 (1970).

74. H. Hasegawa and H.L. Hartnagel, J. Electrochem. Soc. 123 713 (1976).

75. C.R. Stanley, D. Welch, G.W. Wicks, C.E.C. Wood, C. Palmstrom, F.H. Pollak, and P. Parayanthal, Proceedings of the International Symposium on GaAs and related Compounds, Albuquerque, 1982.

76. S.M. Kelso, D.E. Aspnes, M.A. Pollack, and R.E. Nahory, Phys. Rev. B 26, 6669 (9182).

77. T.P. Pearsall, Gallium-Indium-Arsinide-Phosphide alloy semiconductors (New York, John Wiley, 1982) chap 2.

78. P.M. Laufer, F.H. Pollak, R.E. Nahory, and M.A. Pollack, Solid State Commun. 36, 419 (1980).

79. E.H. Perea, E.E. Mendez, and C.C. Fonstad, Appl. Phys. Lett. 36, 978 (1980).

80. Y. Yamozoe, Ph.D thesis (Osaka University, 1981) (unpublished).

81. M.R. Lorenz and A. Onton, Proc. of the 10th International Conference of the Physics of Semiconductors, ed. by S.P. Kelly, J.C. Hensel and H. Stern (Oak Ridge: United States Atomic Energy Commission) pp. 444.

82. O. Berolo and J.C. Wooley, Can. J. Phys. 49, (1971).

83. J.A. Van Vechten and T.K. Bergstresser, Phy. Rev. B 1, 3351 (1970).

84. G.B. Stringfellow, J. Electron. Mater. 10 919 (1981).

85. See for example, W.K. Chu, M.A. Nicolet, J.W. Mayer, and C.A. Evans, J. Anal. Chem. 46 2136 (1974).

86. See for example, C.M. Garner, C.Y. Su, and W.E. Spicer, J. Vac. Sci. Technol. 16, 1521 (1971) P.S. Ho, Surf. Sci. 85, 19 (1979)

87. See for example, R. Sahia, J.S. Harris, D.D. Edwell, and F.H. Eisen, J. Electron. Mater. 6, 645 (1977) and references therein.

88. N. Bohr, Mat. Fys. Medd. Dan. Vid. Selsk. 18, (8) (1948).

89. J. Lindhard and M. Scharff, Mat. Fys. Medd. Dan. Vid. Selsk. 38, (4) (1971).

90. E. Bondurup and P. Hvelplund, Phy. Rev. A 4, 562 (1971).

91. W.K. Chu, Phy. Rev. A, 13, 2057 (1976).

92. See for example, M. Luomajarvi, A. Fontell, and M. Bister, in : Ion Beam Surface Layer analysis edited by O. Mayer, G. Linkes, and F. Kappler (Plenum Press, New York, 1976).

93. See for example, J.M. Harris and M.A. Nicolet Phys. Rev B 11 1013 (1975).

94. H.H. Anderson and J.E. Ziegler, Hydrogen Stopping Powers and Ranges In All Elements (Pergamon, Oxford, 1977).

95. See for Example, W.K. Chu, in Ion Beam Handbook for Materials analysis (Academic Press, New York, 1977).